

HELIOSEISMIC DETECTIONS OF SUNSPOT REGIONS

A DISSERTATION
SUBMITTED TO THE DEPARTMENT OF PHYSICS
AND THE COMMITTEE ON GRADUATE STUDIES
OF STANFORD UNIVERSITY
IN PARTIAL FULFILLMENT OF THE REQUIREMENTS
FOR THE DEGREE OF
DOCTOR OF PHILOSOPHY

Stathis Ikonidis

August 2012

© 2012 by Efstathios Ilonidis. All Rights Reserved.
Re-distributed by Stanford University under license with the author.



This work is licensed under a Creative Commons Attribution-Noncommercial 3.0 United States License.
<http://creativecommons.org/licenses/by-nc/3.0/us/>

This dissertation is online at: <http://purl.stanford.edu/my892yp9456>

I certify that I have read this dissertation and that, in my opinion, it is fully adequate in scope and quality as a dissertation for the degree of Doctor of Philosophy.

Philip Scherrer, Primary Adviser

I certify that I have read this dissertation and that, in my opinion, it is fully adequate in scope and quality as a dissertation for the degree of Doctor of Philosophy.

Vahe Petrosian

I certify that I have read this dissertation and that, in my opinion, it is fully adequate in scope and quality as a dissertation for the degree of Doctor of Philosophy.

Junwei Zhao

Approved for the Stanford University Committee on Graduate Studies.

Patricia J. Gumpert, Vice Provost Graduate Education

This signature page was generated electronically upon submission of this dissertation in electronic format. An original signed hard copy of the signature page is on file in University Archives.

Abstract

Sunspots are regions where strong magnetic fields emerge from the solar interior and where major eruptive events occur. Sunspot studies are needed to understand the generation and emergence of magnetic fields in the photosphere and monitor the solar magnetic activity. In this thesis, local helioseismology methods are used to detect and study sunspot regions on the far-side of the Sun, the photosphere, and the deep convection zone, before these magnetic regions become visible on the solar disc.

One of the successes of helioseismology is the imaging of solar far-side magnetic regions. Helioseismic holography and time-distance technique are capable of detecting sunspot regions on the far side of the sun and provide useful warnings for space weather forecasts. These techniques employ acoustic waves that travel to the far side and return to the front side after multiple bounces in the photosphere. We explore the possibility of far-side imaging by the time-distance technique using three-skip acoustic signals. This method is first validated with use of numerical simulation data and then it is used to detect sunspot regions on the solar far side using SOHO/MDI observations. It is shown that if these maps are combined with maps of existing methods, the appearance of spurious signals is reduced.

Sunspot observations in the photosphere show that the acoustic power inside a sunspot region is significantly reduced compared to the quiet Sun. The power deficit is due to three main groups of physical mechanisms: absorption, emissivity reduction, and local suppression. These effects are separated with a measurement scheme that utilizes one- and double-skip waves in sunspots and quiet-sun regions. Using a large sample of sunspots observed with SOHO/MDI, the coefficients of each mechanism are measured as functions of travel distance and their relative contribution to the total

power reduction is determined as well. The methods and the results of this study will be utilized for the detection of emerging sunspot regions in the convection zone.

Helioseismic methods can be used to detect and study the properties of sunspot regions not only on the solar far side and the photosphere but also in the deep solar interior. We develop a measurement procedure which is capable of detecting emerging sunspot regions at depths around 60,000 km and 1 – 2 days before the detected magnetic structures emerge to the surface. The detection is based on measurements of the acoustic phase travel-time perturbations with the time-distance helioseismology technique using SOHO/MDI, SDO/HMI, and GONG datasets. The travel-time anomalies are related with cross-covariance frequency perturbations that depend strongly on the acoustic frequency. The implications of these measurements to studies of magnetic flux emergence in the solar convection zone and the potential applications to space weather forecasts are discussed.

Acknowledgements

I would like to thank my principal advisor Phil Scherrer for letting me join his research group and explore the fascinating world of solar physics. His leadership skills as principal investigator of SOHO/MDI and SDO/HMI instruments together with his insightful thinking have been a continuing source of inspiration for me.

I am deeply grateful to my co-advisor Junwei Zhao for introducing and teaching me the art of helioseismology. I truly appreciate his valuable advice, constant support, and endless patience without which the completion of this thesis would not be possible.

Many good friends and colleagues have helped me during these years and I would like to thank all of them. It was a huge privilege to be member of the Stanford solar group and work with great people who were always willing to advise and help me. My CMITP colleagues and fellow students made many otherwise dull moments unforgettable. A special thanks should go to my roommate George for his precious help, the intriguing discussions, the incredible laughs, and the epic adventures we had together.

Last, I would like to wholeheartedly dedicate this thesis to my parents, Fotios and Chrysanthi, my family in Greece, and my beloved wife Zeng. Their unconditional love is the most wonderful gift I could ever ask for.

Contents

| | |
|--|------------|
| Abstract | v |
| Acknowledgements | vii |
| 1 Introduction | 1 |
| 1.1 The Sun | 1 |
| 1.1.1 Early observations | 1 |
| 1.1.2 Solar Activity and the Sunspot Cycle | 4 |
| 1.1.3 Solar Storms and Space Weather Effects | 7 |
| 1.2 Helioseismology | 8 |
| 1.2.1 Solar Oscillations | 9 |
| 1.2.2 Global Helioseismology | 10 |
| 1.2.3 Local Helioseismology | 12 |
| 1.2.4 Time-Distance Helioseismology | 14 |
| 1.3 Data | 19 |
| 1.3.1 SOHO/MDI | 20 |
| 1.3.2 SDO/HMI | 22 |
| 1.4 Motivation | 24 |
| 2 Solar Far-Side Imaging | 27 |
| 2.1 Introduction | 27 |
| 2.2 Data and Technique | 28 |
| 2.3 Results | 31 |
| 2.3.1 Results from Numerical Simulation Data | 31 |

| | | |
|----------|---|------------|
| 2.3.2 | Results from MDI observations | 33 |
| 2.4 | Discussion | 38 |
| 3 | Measurements of Absorption | 41 |
| 3.1 | Introduction | 42 |
| 3.2 | Method | 43 |
| 3.3 | Data Analysis and Results | 48 |
| 3.4 | Summary | 57 |
| 4 | Emerging Magnetic Flux I: Method | 59 |
| 4.1 | Introduction | 59 |
| 4.2 | Data and Filtering | 64 |
| 4.3 | Method | 64 |
| 4.3.1 | Phase-speed filtering | 65 |
| 4.3.2 | Averaging of the Oscillation Signal | 68 |
| 4.3.3 | Multiple Arc Configurations | 68 |
| 4.3.4 | Depth Averaging | 72 |
| 4.3.5 | Discussion | 74 |
| 5 | Emerging Magnetic Flux II: Results | 79 |
| 5.1 | Detection of Emerging Magnetic Flux | 79 |
| 5.2 | Temporal Evolution and Depth Dependence | 89 |
| 5.3 | Frequency Perturbations | 94 |
| 5.4 | Results from SDO/HMI and GONG | 98 |
| 5.5 | Discussion | 102 |
| 6 | Summary and Perspective | 109 |
| 6.1 | Summary | 109 |
| 6.2 | Perspective | 111 |
| | Bibliography | 114 |

List of Tables

| | | |
|-----|--|----|
| 4.1 | Phase-speed filtering parameters | 78 |
|-----|--|----|

List of Figures

| | | |
|-----|--|----|
| 1.1 | Earliest and recent sunspot images | 3 |
| 1.2 | International sunspot numbers | 5 |
| 1.3 | “Butterfly diagram” | 6 |
| 1.4 | Two-dimensional power spectrum of solar oscillations | 11 |
| 1.5 | Ring diagrams with SOHO/MDI and TON | 13 |
| 1.6 | Carrington maps of magnetic flux (Earthside) and inferred flux (farside). | 15 |
| 1.7 | Optical layout of Michelson Doppler Imager | 21 |
| 1.8 | Example of HMI tuning-position profiles | 23 |
| 2.1 | Power spectrum and time-distance diagram for the three-skip far-side imaging | 30 |
| 2.2 | Three-skip measurement scheme | 31 |
| 2.3 | Far-side images for simulations | 33 |
| 2.4 | Results of far-side imaging for 8 November 2003 | 34 |
| 2.5 | Results of far-side imaging for 9 November 2003 | 35 |
| 3.1 | Energy budget of acoustic waves propagating through the quiet sun and a sunspot | 44 |
| 3.2 | Dissipation coefficient | 49 |
| 3.3 | Time-distance diagrams of ingoing and outgoing waves and amplitude fittings | 51 |
| 3.4 | Time-distance diagrams of one- and two-skip waves and amplitude fittings | 52 |

| | | |
|------|--|----|
| 3.5 | Coefficients of absorption, emissivity reduction, and local suppression for umbral measurements | 54 |
| 3.6 | Coefficients of absorption, emissivity reduction, and local suppression for sunspot measurements | 55 |
| 3.7 | Normalized coefficients | 57 |
| 4.1 | Cartoon representation of an emerging active region | 60 |
| 4.2 | Previous helioseismic measurements in an emerging-flux region | 63 |
| 4.3 | Power spectrum of solar oscillations used for the detection of emerging magnetic flux | 65 |
| 4.4 | Acoustic ray paths | 66 |
| 4.5 | Step-by-step improvement of the S/N ratio | 67 |
| 4.6 | Comparison of two phase-speed filters | 69 |
| 4.7 | Optimization of the phase-speed filter | 70 |
| 4.8 | Comparison of point-to-point with arc-to-arc computation of cross- covariances | 71 |
| 4.9 | Schematic representation of the 20 arc configurations used for the com- putation of cross-covariances | 72 |
| 4.10 | Phase travel-time perturbation maps of AR 10488 made using 20 arc configurations | 73 |
| 4.11 | Phase travel-time perturbation maps of AR 10488 for various arc sizes and depths | 75 |
| 4.12 | Effects of geometry and filtering on helioseismic measurements | 77 |
| 5.1 | Intensity observations of AR 10488 | 80 |
| 5.2 | Magnetograms before and after the emergence of AR 10488 | 81 |
| 5.3 | Detection of emerging magnetic flux in AR 10488 | 83 |
| 5.4 | Detection of emerging magnetic flux in AR 8164 | 84 |
| 5.5 | Detection of emerging magnetic flux in AR 8171 | 85 |
| 5.6 | Detection of emerging magnetic flux in AR 7978 | 86 |
| 5.7 | Distribution of travel-time perturbations measured in quiet regions . | 88 |
| 5.8 | Temporal evolution of travel-time perturbations in AR 10488 | 90 |

| | | |
|------|--|-----|
| 5.9 | Temporal evolution of travel-time perturbations in AR 8164 | 91 |
| 5.10 | Temporal evolution of travel-time perturbations in AR 8171 | 92 |
| 5.11 | Temporal evolution of travel-time perturbations in AR 7978 | 93 |
| 5.12 | Temporal evolution of mean travel-time perturbation maps of AR 10488 at 3 different depths, part I | 95 |
| 5.13 | Temporal evolution of mean travel-time perturbation maps of AR 10488 at 3 different depths, part II | 96 |
| 5.14 | Normalized perturbation at 3 different depths | 97 |
| 5.15 | Travel-time and frequency perturbations around 3.3 mHz | 99 |
| 5.16 | Travel-time and frequency perturbations around 3.7 mHz | 100 |
| 5.17 | Travel-time and frequency perturbations around 4.0 mHz | 101 |
| 5.18 | Detection of emerging flux in AR 11158 observed with SDO/HMI . . | 103 |
| 5.19 | Temporal evolution of travel-time perturbations in AR 11158 | 104 |
| 5.20 | Comparison of MDI and GONG travel-time maps of AR 10488 | 105 |

Chapter 1

Introduction

1.1 The Sun

1.1.1 Early observations

The Sun is perhaps the most fascinating object in the sky and the nearest star to the Earth. Sun worship can be found in most ancient civilizations. Some of the first significant attempts to understand the Sun and the solar system were made by the ancient Greeks more than 2500 years ago. The Athenian Anaxagoras (c. 500 BCE – 428 BCE) described the Sun and the stars as fiery rocks larger than the size of Peloponnessus, roughly 160 km (A Refutation of All Heresies, 1, epitome, 3). He also explained that we do not feel the heat of other stars due to their vastly large distances from the Earth. Aristarchus of Samos (310 BCE – c. 230 BCE) was the first to suggest the heliocentric model in which the Sun is at the center of the solar system and the Earth and the other planets revolve around the Sun. This model received little support for nearly 1800 years until it was revived by Polish astronomer Nicolaus Copernicus (1473 CE – 1543 CE).

Aristarchus also tried to measure the distance between the Earth and the Sun as well as the solar diameter. His method was based on estimating the angle between the moon, the Earth, and the Sun at half moon, the time that the moon appears half-illuminated to an observer at the Earth. Although this method is perfectly valid,

an uncertainty of less than 3 degrees in the estimate of this angle led to a large underestimate of the Sun's distance to only 18 – 20 times the moon's distance while the actual value is about 400. An independent way of measuring the distance to the Sun was proposed in the Chinese mathematical treatise *Zhou Bi Suan Jing* (c. 1st century BCE) assuming a flat Earth. According to this method, the solar distance can be determined geometrically by placing rods of known length at a fixed distance and measuring the length of shadows at noon. The distance of 80,000 li (roughly 40,000 km) that was deduced from these measurements was again too short. Eusebius of Caesarea mentions in *Preparatio Evangelica* that Eratosthenes of Cyrene (c. 276 BCE – c. 194 BCE) found the distance to the Sun to be “stadia myriads 400 and 80,000” which can be interpreted as 400 myriad plus 80,000 or “400 and 80,000” myriad. If the latter interpretation is correct and with a stadium of 185 m, a value of 804,000,000 stadia is obtained which is equal to about 149,000,000 km.

Aristotle (384 BCE – 322 BCE) believed that the Sun was perfect and constant and this belief was maintained for centuries. However, people noticed transient changes on the Sun with naked-eye observations long before the invention of telescope around 1608. There are tens or hundreds of records from China, Korea, Vietnam, Japan, and other countries of features on the solar disc that seemed to be naked-eye sunspots. The earliest definite observation of a sunspot was recorded in China in 165 BCE (Wittmann & Xu, 1987). The first clear reference to a sunspot in western literature is probably by Aristotle's pupil, Theophrastus of Athens (c. 371 BCE – c. 287 BCE), around 300 BCE. The earliest known drawing of sunspots is from a sighting on 8 December 1128 and appears in *The Chronicle of John of Worcester* (Figure 1.1). The sunspot was depicted as a large round feature on the solar surface with a dark spot at the center, known now as umbra, surrounded by a lighter region, the penumbra. With the invention of telescope, sunspots have been systematically observed and a large volume of scientific data has been collected since the beginning of the 17th century. These observations are currently used to understand the physical mechanisms that drive the solar activity, an investigation that started more than 2500 years ago and continues up to date.

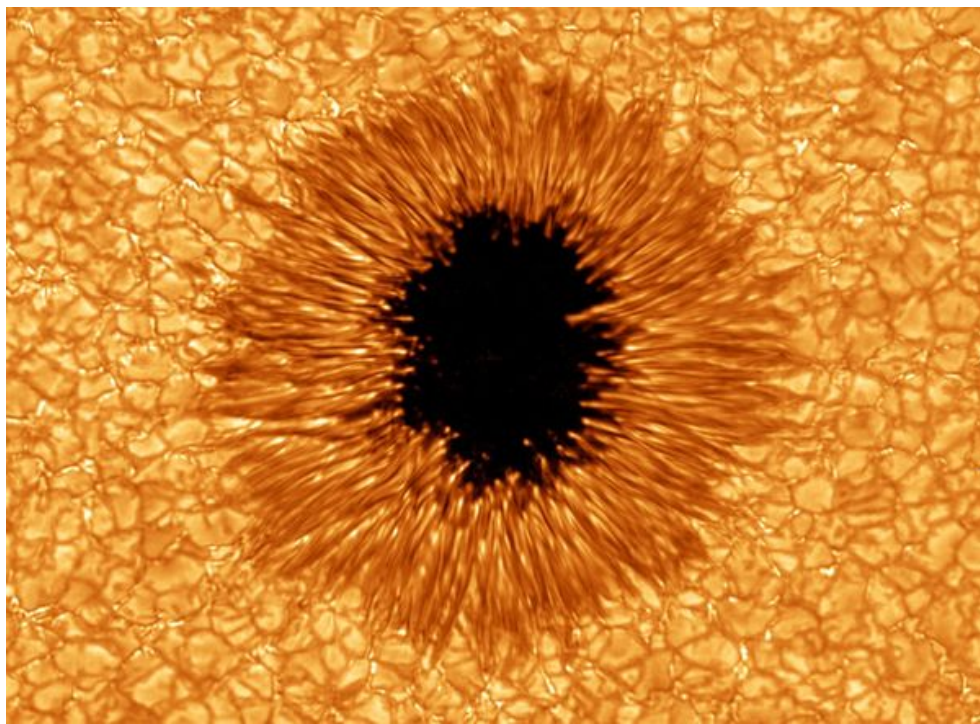
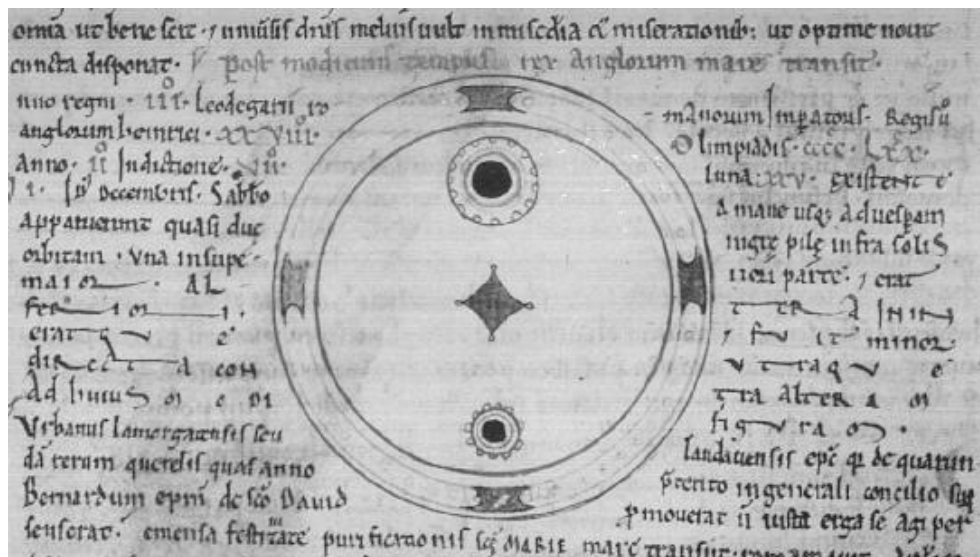


Figure 1.1: Earliest known sunspot drawing, from the Chronicle of John of Worcester, 12th century (upper) and one of the most detailed sunspot images that have ever been observed (lower). The upper image is reproduced from R.W. Southern, *Medieval Humanism*, Harper & Row 1970, [Plate VII] and the lower image is courtesy of Big Bear Solar Observatory.

1.1.2 Solar Activity and the Sunspot Cycle

Solar activity has a vast variety of manifestations ranging from photospheric and chromospheric features, such as sunspots, faculae, and plages, to eruptive processes, such as flares and coronal mass ejections (CMEs), and numerous other phenomena in the atmosphere and the solar wind. Many of these phenomena are directly related with the highly complex and dynamic nature of solar magnetism. Several indices have been used over the years to quantify the solar activity and study its temporal variability. Among the most commonly used indices is the sunspot number (Figure 1.2) which is defined as a weighted number of individual sunspots and sunspot groups counted according to a prescribed manner (for more details see Usoskin, 2008). Since the detection and study of sunspot regions is the main topic of this dissertation, below we discuss the basic properties of sunspot cycle.

Solar activity exhibits an 11-year magnetic cycle which is probably produced by dynamo processes in the solar interior. The sunspot cycle was discovered in 1844 when Heinrich Schwabe reported that sunspot observations appeared to have a 10-year periodicity (Schwabe, 1844). During the minimum of the activity, the Sun is either spotless or if it is not, only few sunspots are observed on the solar disc at any given day. As the cycle evolves more and more sunspots emerge in the photosphere and during the peak of the activity dozens of sunspots are visible in the solar surface. The distribution of sunspots in heliographic latitude is not uniform; sunspots emerge mostly at mid-latitudes in the beginning of the cycle with the emergence locations migrating towards the equator as the cycle progresses (Maunder, 1904). This pattern is often depicted in a diagram of latitudinal sunspot locations as a function of time, the so-called “butterfly diagram” (Figure 1.3).

The magnetic field in bipolar magnetic regions is such that the leading sunspots in one hemisphere have the same magnetic polarity, which is opposite to the magnetic polarity of the leading sunspots in the opposite hemisphere (Hale et al., 1919). This property is known as Hale’s law. The polarity of leading and following sunspots in each hemisphere reverses at the end of sunspot cycle and so the period of sunspot cycle is only half of the actual period of solar cycle. Hale et al. (1919) also showed that bipolar magnetic regions tend to be “tilted” relative to the equator, with the

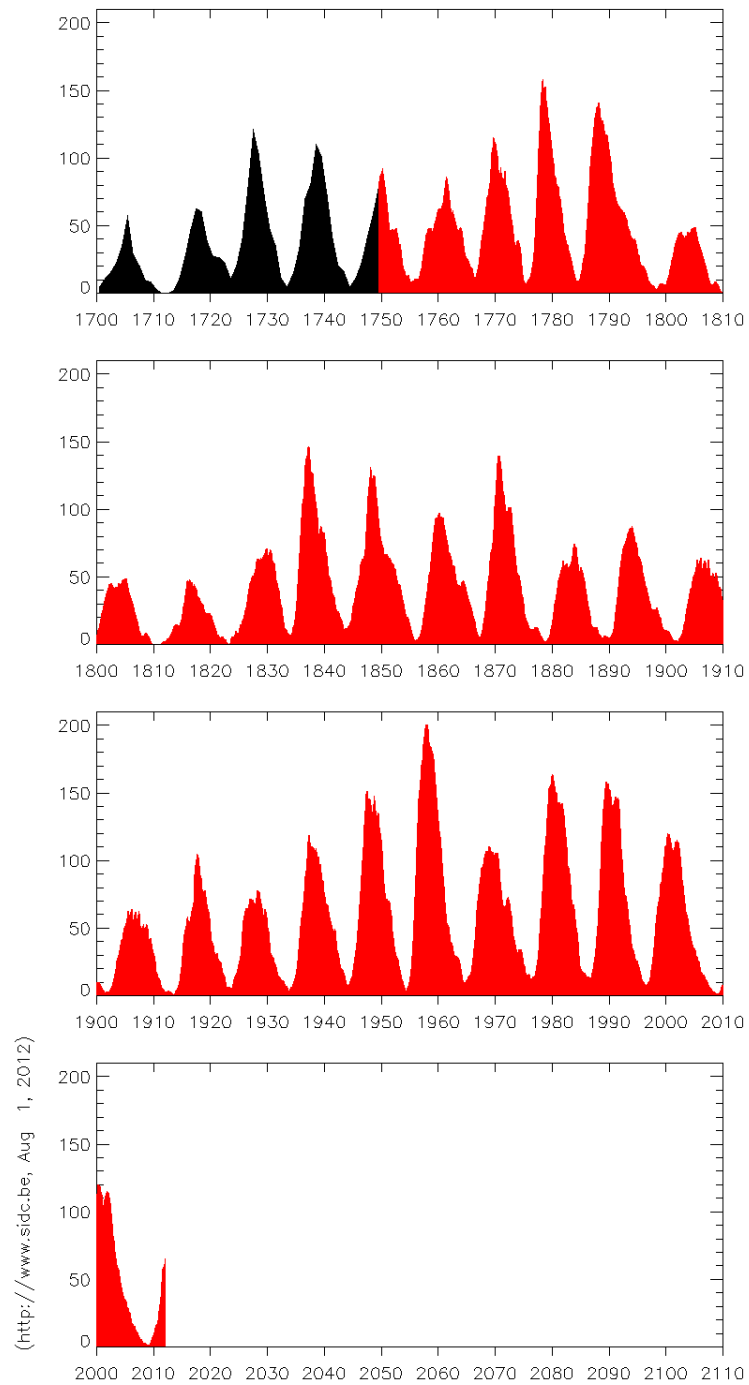


Figure 1.2: International sunspot numbers from 1700 up to now provided by the Solar Influences Data Analysis Center (SIDC) in Belgium. Yearly averages are shown in black and monthly averages are shown in red. Figure courtesy of SIDC-team, World Data Center for the Sunspot Index, Royal Observatory of Belgium.

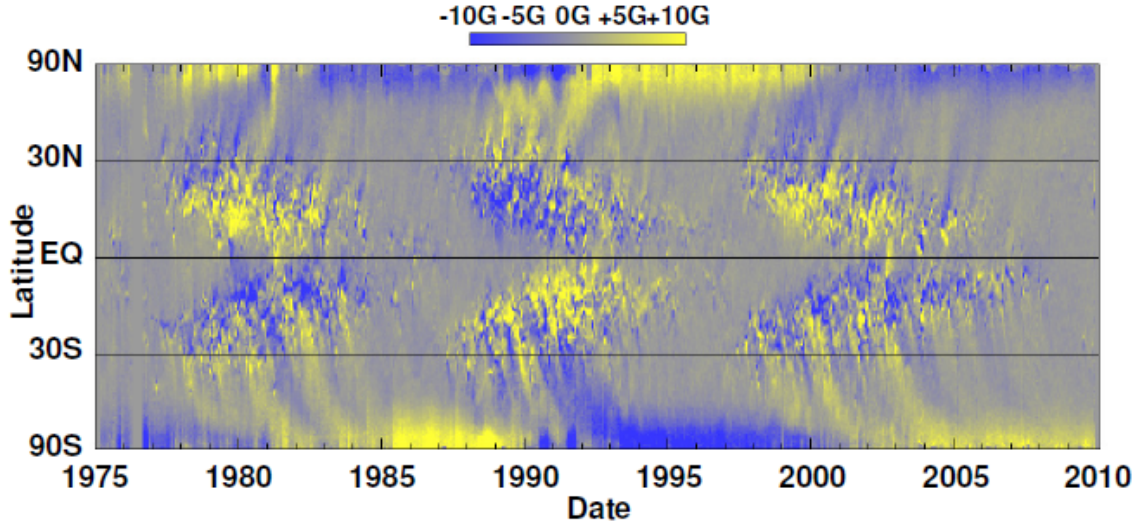


Figure 1.3: Magnetic “Butterfly diagram” showing Hale’s and Joy’s laws and the migration of sunspots from mid-latitudes towards the equator during the course of a sunspot cycle. The Figure is adopted from Hathaway (2010).

leading sunspot being closer to the equator. This property, which is known as “Joy’s law”, appears only statistically and the orientation of individual bipolar regions may vary significantly.

The origin of solar activity is believed to be a dynamo mechanism that operates in tachocline, a thin shear layer at the base of the convection zone. In most dynamo models, magnetic fields, generated in tachocline, emerge through the convection to the photosphere and form active regions. However, the detailed mechanism of the solar dynamo is not known and there is no model that can reproduce all the observed properties of solar activity. Understanding the physical mechanisms that generate and transport magnetic fields from the deep interior of the Sun to the surface is perhaps one of the most important questions in solar physics. For a detailed review of solar dynamo models see Charbonneau (2010).

1.1.3 Solar Storms and Space Weather Effects¹

Solar activity has strong influence on the Earth and the interplanetary space. One example is flares and CMEs that may arrive on the Earth and cause space weather storms. There are 3 types of space weather storms: geomagnetic storms, radiation storms, and radio blackouts. Geomagnetic storms are temporary disturbances of the geomagnetic field caused by solar wind gusts. Radiation storms are caused by high levels of solar radiation that occur when the numbers of energetic particles increase. Radio blackouts are disturbances in the ionosphere caused by x-ray emission from the sun.

When a CME arrives at Earth, it does not always have the same effect. If the north-south (or z) component of the CME field is positive (northward field), the CME will have little or no effect on the Earth. However, if the north-south component of the field is negative, it opposes the direction of the Earth's magnetic field. In this case the two fields interact, allowing energy from the solar wind to enter the Earth's magnetosphere. Such events can cause magnetic storms, periods when the Earth's magnetic field is highly disturbed.

Geomagnetic storms can induce strong currents that flow through the Earth and have the ability to damage extra high-voltage transformers. A severe geomagnetic storm that occurred in Quebec on March 13, 1989 caused a transformer failure on one of the main power transmission lines in the Hydro Quebec system which led, in less than 90 seconds, to the collapse of the entire power grid. The geomagnetic storm was the result of a CME that occurred on March 9, 1989. Such strong storms have significant impact on satellites as well. Some of the problems include increased drag, surface charging, solar panel degradation, single event upsets, contamination of the image systems, and orientation problems.

The effects of space weather are not restricted to electrical power grids and satellites. Geomagnetically induced currents may contribute to the corrosion of gas and oil pipelines. Solar storms cause degradation or blackouts of high-frequency radio communications affecting maritime and aviation systems. Navigation aided by the global

¹The description here follows my report on solar storm vulnerability published online in the following webpage: <http://large.stanford.edu/courses/2010/ph240/ilonidis1/>

positioning system (GPS) is also affected by space weather. During severe events, polar flights need to be diverted to lower latitudes with additional stop-offs. Radiation storm levels are often high enough and create concerns for passengers and crew of airlines as well as for astronauts. These concerns are much greater for manned missions to the Moon and Mars. Last, the robotic arm and workstation on the International Space Station are also very sensitive to radiation events.

One of the most important functions of a space weather forecast agency is to provide reliable and long-term forecasts, with minimal false alarms, in order to minimize the economic impact of a space storm. Currently, the Space Weather Prediction Center (SWPC) can predict the occurrence of a geomagnetic storm or a strong (X-class) flare 1 to 3 days in advance with moderate confidence. However, the forecast of ionospheric disturbances, which is important for GPS users, is less reliable. Forecasts, for example, posted by SWPC five days before the strongest flare of the previous solar cycle were 50%, 40%, 35%, 75%, 75%. On the day of the flare, November 4, 2003, the probability remained at 75% and the following days dropped to 10%, 1%, 1%.

1.2 Helioseismology

The deep interior of the Sun and other stars was one of the least accessible regions to scientific investigation up to about 50 years ago. The discovery of periodic oscillations on the solar surface in the early '60s set the foundations for the development of a new research field, that of helioseismology. Helioseismology is the study of solar oscillations in order to investigate the subsurface structure of the Sun. The first helioseismic methods examined the global structure of the Sun with limited ability to study the properties of local regions. In the last 20 years, new techniques were developed which are now widely used for the study of small-scale features, such as sunspots and supergranules. A brief introduction to the properties of solar oscillations and the most common helioseismic methods is given below, although only one of these methods, the time-distance technique, was used in this dissertation.

1.2.1 Solar Oscillations

Solar oscillations with a period of about 5 minutes were first observed in 1960 (Leighton et al., 1962) by a spectroheliographic technique at mount Wilson Observatory. This groundbreaking observation was later confirmed by Evans & Michard (1962). Several theoretical models were suggested to interpret the observation but it took almost a decade until Ulrich (1970) and Leibacher & Stein (1971) explained the observed oscillatory motions by standing acoustic waves in the solar interior. Several other studies (Deubner, 1975; Rhodes et al., 1977; Claverie et al., 1979; Duvall & Harvey, 1983) confirmed this interpretation and found a ridge structure in power spectra which is consistent with the model of standing waves. It is believed that solar oscillations are excited by turbulent convective motions near the surface of the Sun (Goldreich & Keeley, 1977).

The acoustic waves, which are excited near the surface, propagate in the solar interior but since the sound speed increases with depth, the waves are constantly refracted and return to the surface. At the surface, they are reflected back to the interior due to the sudden decrease in density. Eventually the acoustic waves remain trapped in the solar interior and the Sun acts as a resonant cavity. The oscillation signal $v(r, \theta, \phi, t)$ can be described as a sum of normal modes.

$$v(r, \theta, \phi, t) = \sum_{n,l} \sum_{m=-l}^{m=l} A_{nlm} \xi_{nl}(r) Y_{lm}(\theta, \phi) e^{i[\omega_{nlm}t + \alpha_{nlm}]} \quad (1.1)$$

where the three integers n , l , m are the radial order, angular degree, and azimuthal order respectively, A_{nlm} is the mode amplitude, ξ_{nl} is the radial eigenfunction, Y_{lm} is the spherical harmonic, ω_{nlm} is the eigenfrequency, and α_{nlm} is the phase of the mode. The spherical harmonics have the form

$$Y_l^m(\theta, \phi) = a_{lm} P_l^m(\cos\theta) e^{im\phi} \quad (1.2)$$

where P_l^m is the associated Legendre polynomial and a_{lm} is a normalization factor. The radial order n corresponds to the number of nodes of the radial eigenfunction, the angular degree l gives the total number of node circles on the sphere, and the

azimuthal order m indicates how many of these node circles cross the equator. In a spherical system with no preferred axis of symmetry, the eigenfrequencies do not depend on m . However, the solar rotation defines a particular axis of symmetry and the oscillation frequencies show a weak dependence on m . The eigenfrequencies ω_{nlm} of the solar oscillations are measured from the resonant peaks in the power spectrum (Figure 1.4) and they are used as a diagnostic of the solar interior. The amplitude of a single mode is about 30 cm/s and the interference of 10 million or more oscillation modes with randomly distributed phases results in oscillation amplitudes of 0.5 to 1 km/s or larger in more extreme cases.

1.2.2 Global Helioseismology

The goal of global helioseismology is to determine the internal structure of the Sun from the observed eigenfrequencies of solar oscillations. Precise measurements of the eigenmode frequencies require long uninterrupted observations. The Taiwan Oscillation Network (Chou et al., 1995) and the Global Oscillation Network Group (Harvey et al., 1996) are among the ground-based networks of observatories that provided such observations. In addition, space instruments such as the Michelson Doppler Imager onboard the Solar and Heliospheric Observatory (Scherrer et al., 1995) provided high quality data without the problems of atmospheric seeing.

If the sound-speed and density in the solar interior are denoted by c and ρ respectively, the shift in the eigenmode frequency $\delta\omega$ for the (n, l) mode can be written as

$$\frac{\delta\omega_{nl}}{\omega_{nl}} = \int_0^{R_\odot} \left[K_{c^2, \rho}^{nl}(r) \frac{\delta_r c^2(r)}{c^2(r)} + K_{\rho, c^2}^{nl}(r) \frac{\delta_r \rho(r)}{\rho(r)} \right] dr \quad (1.3)$$

where $K_{c^2, \rho}^{nl}(r)$ and $K_{\rho, c^2}^{nl}(r)$ are the inversion kernels, functions which describe the sensitivity of the (nl) eigenfrequency to changes in the model. It has been shown (Basu et al., 1997, Kosovichev et al., 1997) that the sound-speed and density distributions inferred by global helioseismology agree with the standard solar model (Christensen-Dalsgaard et al., 1996) within 1% or less.

The splitting of the eigenfrequencies $\delta\omega_{nlm}$ for modes with the same radial order n and angular degree l but different azimuthal order m can be used to infer the internal

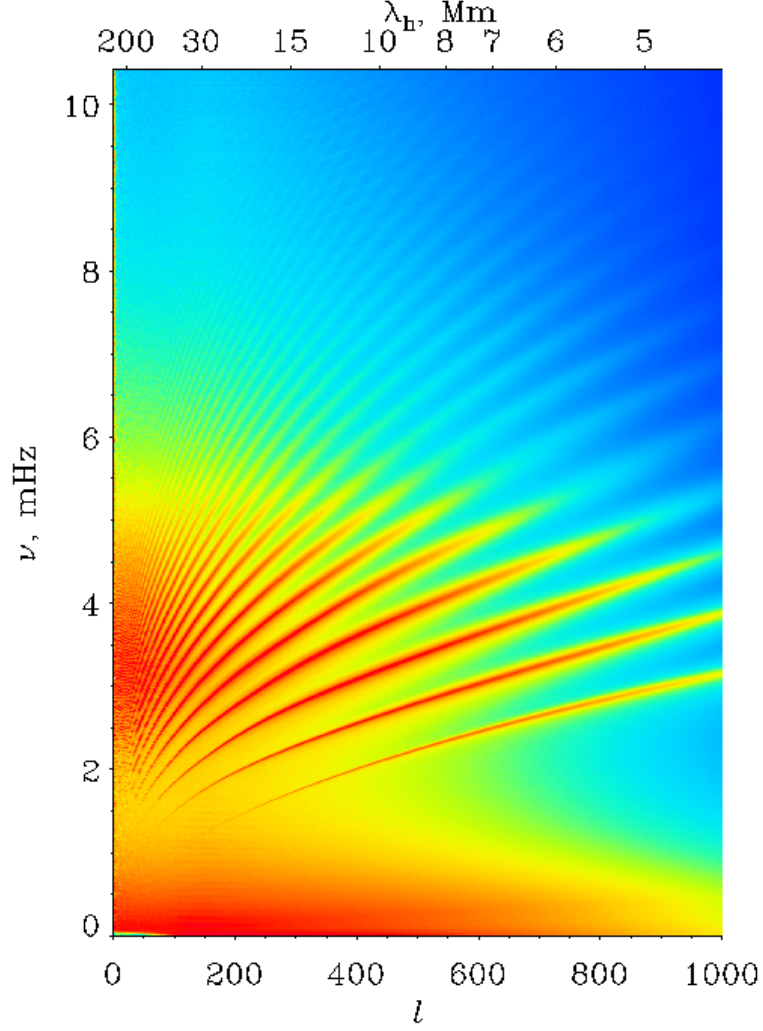


Figure 1.4: Two-dimensional power spectrum of solar oscillations. The eigenfrequencies of these oscillations can be identified from the locations of ridge structures. Figure courtesy of SOI/MDI Team.

rotation rate Ω as a function of solar radius and latitude. The frequency splitting derived from linear perturbation theory is given by

$$\delta\omega_{nlm} = \omega_{nlm} - \omega_{nl0} = \int_0^R \int_0^\pi K_{nlm}(r, \theta) \Omega(r, \theta) r dr d\theta \quad (1.4)$$

where K_{nlm} is the sensitivity kernel. This method was used to infer the differential

rotation throughout most of the convection zone (Schou et al., 1998).

1.2.3 Local Helioseismology

Local helioseismology techniques were developed to probe structures and flows at smaller spatial scales than those explored by global helioseismology. Among the local helioseismology techniques that have been widely developed and used in the last 20 years are the ring diagram analysis (Hill, 1988), the time-distance technique (Duvall et al., 1993), and the helioseismic holography (Lindsey & Braun, 1997).

Ring Diagram Analysis was first introduced by Gough & Toomre (1983) and Hill (1988). This technique is based on the computation of power spectra from the oscillation signals of small patches of the solar surface. A cut at constant frequency of three dimensional power spectra shows ring structures (Figure 1.5) that correspond to the ridges of the normal modes. Flows and sound-speed perturbations in the region of wave propagation distort or alter the location of the rings. Therefore, fittings of the position and the shape of the rings can be used to infer flows and sound-speed perturbations in a local region of the sun. Important results have been obtained by this method including inferences of the rotational speed and meridional flow (Schou & Bogart, 1998; Basu et al., 1999; Haber et al., 2000, 2002)

Time-distance helioseismology was first applied by Duvall et al. (1993, 1996) and since then became one of the major techniques of local helioseismology. The time-distance technique is applied by selecting pairs of points on the solar surface and cross-correlating the observed oscillation signals at these points. It is possible, from the cross-correlation function, to obtain estimates of the acoustic travel times for the selected pairs of points (Kosovichev & Duvall, 1997; Gizon & Birch, 2004). These travel times are then inverted to infer local sound-speed perturbations and flows in the solar interior.

Time-distance helioseismology has been widely used to infer the interior sound-speed perturbations and flows of sunspot regions (Kosovichev et al., 2000; Zhao et

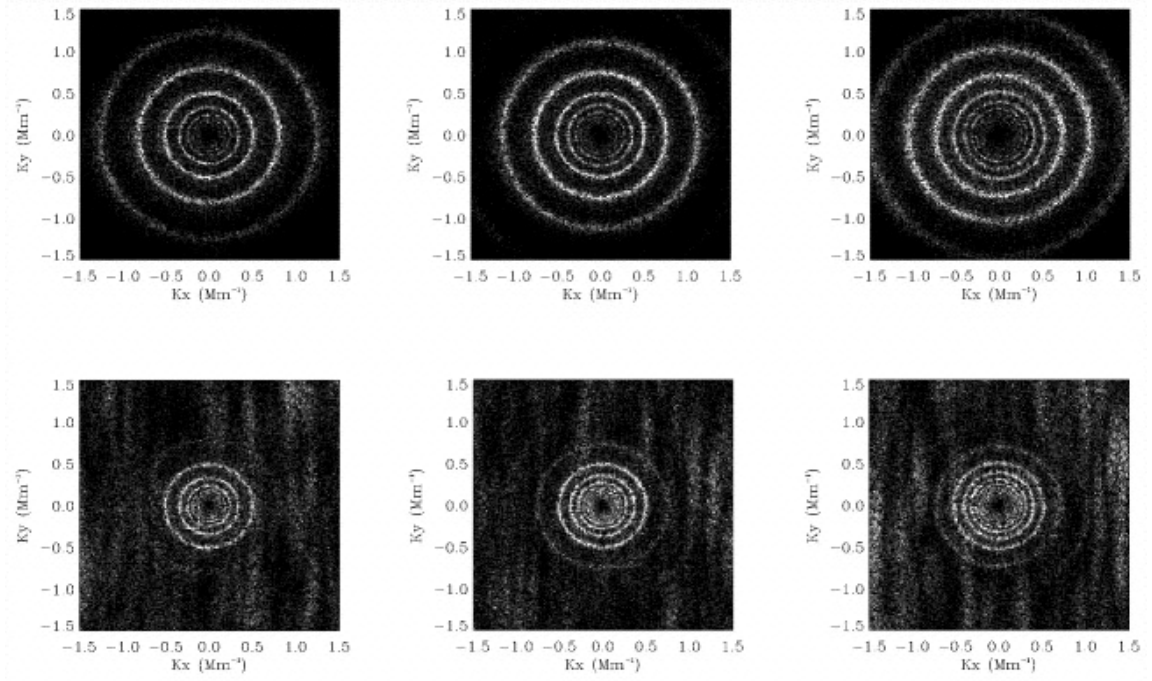


Figure 1.5: Cuts at constant frequencies of three-dimensional power spectra obtained with SOHO/MDI (upper) and TON (lower) instruments. The frequencies are 3.0 mHz (left), 3.5 mHz (middle), and 4.0 mHz (right). The plot is adopted from González Hernández et al., (1998).

al., 2001, Zhao & Kosovichev 2003) and measure meridional flows (Giles et al., 1997; Zhao & Kosovichev, 2004) and the rotational velocity (Giles, 1999).

The time-distance technique is used throughout this dissertation and more detailed descriptions of the technique are given in the next section.

Helioseismic Holography was proposed by Roddier (1975) and developed by Lindsey & Braun (1990, 1997). The main idea of helioseismic holography is that the oscillation signal at any location and time in the solar interior can be estimated from the oscillations observed at the surface of the sun. Helioseismic holography was also developed in parallel by Chang et al. (1997), who used the term “acoustic imaging” to describe the new technique.

The formalism of acoustic egression and ingression is used in helioseismic holography. If $\Psi(\mathbf{r}', t')$ is the acoustic wavefield at time t' and horizontal location \mathbf{r}' , then the acoustic ingression (H_-) and egression (H_+) are given by

$$H_{\pm}(\mathbf{r}, z, t) = \int dt' \int_P G_{\pm}(|\mathbf{r} - \mathbf{r}'|, z, t - t') \Psi(\mathbf{r}', t') d^2\mathbf{r}' \quad (1.5)$$

where the second integral is computed over a pupil P on the surface, z is the depth below the surface, and G_{\pm} are Green's functions that show how a disturbance observed at location $(\mathbf{r}', z = 0)$ and time t' propagates forward and backward in time to location (\mathbf{r}, z) and time t . Computations of ingression and egression power maps revealed the existence of “acoustic moats” (Lindsey & Braun, 1998) and “acoustic glories” (Braun & Lindsey, 1999) in the vicinity of sunspot regions.

Phase-sensitive helioseismic holography, which is based on the correlation of ingression and egression signals, was later developed by Braun & Lindsey (2000). The temporal correlation

$$C(\mathbf{r}, z, \tau) = \int H_-(z, \mathbf{r}, t') H_+(z, \mathbf{r}, t' + \tau) dt' \quad (1.6)$$

is used as a diagnostic of perturbations in the solar interior. One of the major successes of phase-sensitive holography was the imaging of magnetic regions on the solar far side (Lindsey & Braun, 2000a). Active regions on the far side of the sun can be detected by the helioseismic holography technique before they become visible on the solar disc (Figure 1.6).

1.2.4 Time-Distance Helioseismology

Tracking and Remapping

The procedure of making time-distance measurements starts with the tracking and remapping of three-dimensional datacubes, with the first two dimensions being the heliographic longitude and latitude and the third dimension being the time. The oscillation signal is usually intensity fluctuations or Doppler velocity. In this thesis, we only use Doppler velocity signals.

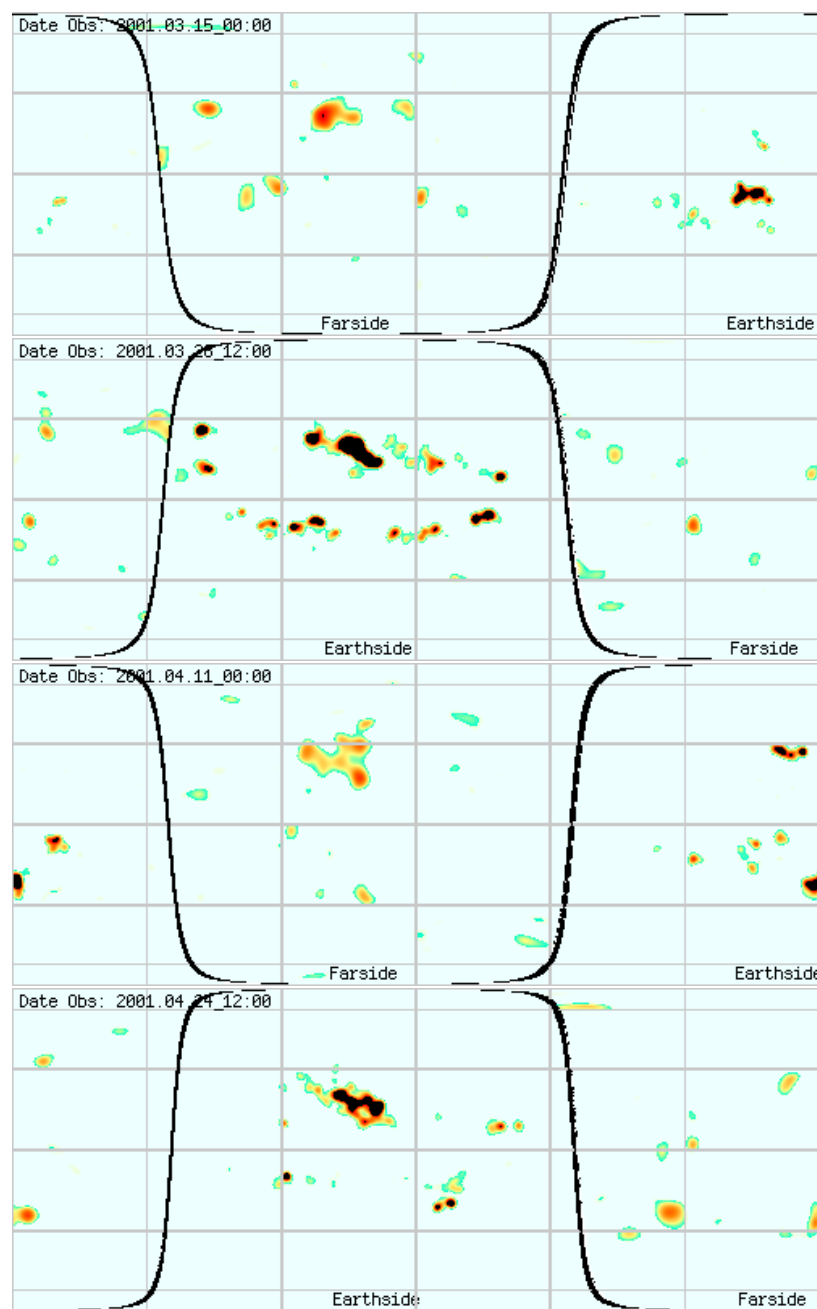


Figure 1.6: Carrington maps of magnetic flux (Earthside) and inferred flux (farside). The far-side images were made with the helioseismic holography technique using MDI data. Region 9393 is seen at longitude 154° and latitude 17° . This region was first detected on the far side and it can be successively seen on the far-side and front-side maps for at least two Carrington rotations. Images were taken from top to bottom on 15 March 2001, 28 March 2001, 11 April 2001, and 24 April 2001. Figure courtesy of SOI/MDI Team.

Since the rotation in the solar photosphere is not uniform but it depends on the heliographic latitude, a latitude dependent tracking rate (Snodgrass, 1984) is often used in helioseismic studies. However, if the tracked region is not very large and the temporal duration of the dataset is not too long to cause distortion of high latitude regions, a uniform tracking rate may be used. One such option is the Carrington rotation rate with frequency of 456 nHz and sidereal rotation period of 25.38 days. Most datasets in this thesis have a spatial size of $30^\circ \times 30^\circ$ and a temporal duration of 8 hours. These datasets are tracked with the Carrington rotation rate.

The mapping of the spherical solar surface to a Cartesian plane can be done using various projections. The azimuthal equidistant projection (or Postel projection) was mostly used in this dissertation. In this type of projection, distances and directions are correct only between points along straight lines through the center of the projection. It has been shown that Postel projection is good in minimizing distortions and giving "sharp" power spectra (Bogart et al., 1995).

Filtering

Filtering of the oscillation signal in the Fourier domain is the next step of the measurement procedure. The observed Doppler velocity signal has contributions not only from p-mode waves but also from f-mode waves, convective motions, and high-frequency waves that are not trapped in the solar interior. It is often necessary, in order to enhance the S/N ratio, to keep only the oscillation signals that are relevant for our analysis and remove or reduce the contribution of other oscillation signals. This is done with frequency, f-mode, phase-speed, direction, and ridge filters.

Frequency filters are often applied in order to remove oscillation signals below or above a specific frequency threshold. At low frequencies, typically below 1.6 mHz, the oscillation power is dominated by strong convective motions. At high frequencies, above the acoustic cut-off frequency around 5.3 mHz, the waves escape into the atmosphere and have different physical properties. Thus, it is common in time-distance measurements to filter out waves below 1.6 mHz and above 5.3 mHz.

Surface gravity waves have very different nature than pressure waves. They are horizontally propagating disturbances which stay mostly near the surface and do not

follow ray paths. Time-distance measurements with f-modes is a very useful tool to explore near-surface structures and flows (Gizon et al., 2000) but f-mode signals are often filtered out when p-mode signals are used. The f-mode filter used throughout this dissertation is the same with that used by Giles (1999).

Phase-speed filters have been widely used in local helioseismology to enhance the S/N ratio. A phase-speed filter selects waves with a small range of horizontal phase speeds ω/k , which travel similar horizontal distances, and excludes waves with much higher or lower phase speeds. If we determine the horizontal distance of the oscillation signals used for the cross-correlation computations and choose the appropriate phase-speed filter, it is possible to obtain a much higher S/N ratio. The selection of appropriate phase-speed filters is an important ingredient of this dissertation and it will be further discussed in chapter 4. A list of phase-speed filters that are commonly used in time-distance measurements is given in Zhao et al. (2012).

Direction filters select waves that propagate in a small range of directions. This may be useful for time-distance measurements along specific directions, such as estimates of flows in the North-South and East-West directions, or measurements around sunspots (see Giles, 1999; Chou et al., 2009a). We do not use direction filters in this thesis and therefore we will not elaborate on this topic.

Ridge filters are used to isolate oscillation modes with fixed radial order n . These oscillation modes are all within the same ridge of the power spectrum. The advantages and disadvantages of using ridge filters compared to phase-speed filters are discussed in Zhao, Chou, & Yang (2011).

Cross-correlation computations

As soon as the procedures of tracking, remapping, and filtering are done, the computation of temporal cross-covariance functions is performed. A spatial averaging is often required since point-to-point cross-covariances are too noisy due to stochastic nature of solar oscillations. In most cases, an annulus with radius Δ is selected over a central location \mathbf{r} and the oscillation signal is averaged either over the whole annulus or over part of the annulus, typically a quadrant oriented in the East-West or North-South direction. The temporal cross-covariance $C_{ann}(\mathbf{r}, \Delta, t)$ is then computed

between the oscillation signal at the central point $\Psi(\mathbf{r}, t)$ and the averaged signal on the annulus $\Psi_{ann}(\Delta, t)$

$$C_{ann}(\mathbf{r}, \Delta, \tau) = \frac{h_t}{T - |\tau|} \sum_t \Psi(\mathbf{r}, t) \Psi_{ann}(\Delta, t + \tau) \quad (1.7)$$

where h_t is the temporal sampling, T is the length of temporal duration of the observation, and τ is the time lag.

Estimate of the travel time

It is possible, from the observed cross-covariance function, to make estimates of the acoustic travel time between pairs of locations on the solar surface. There are currently two major methods to estimate travel times, the fitting with a Gabor wavelet (Kosovichev & Duvall, 1997) and the one-parameter fit (Gizon & Birch, 2004). The two methods use different definitions of travel-time and they should not always be expected to provide similar travel-time estimates.

The Gabor wavelet function, for travel distance Δ and time lag τ , has the form:

$$G(\Delta, \tau) = A \cos(\omega_0(\tau - \tau_{ph})) \exp\left[-\left(\frac{\delta\omega}{2}(\tau - \tau_{gr})\right)^2\right] \quad (1.8)$$

where A is the amplitude, ω_0 is the central frequency, $\delta\omega$ is the frequency bandwidth, and τ_{gr} and τ_p are the group and phase travel times respectively. The phase travel times are significantly less noisy than the group travel times and therefore it is customary to use only phase travel time measurements.

The one-parameter fit is based on comparison of the measured cross-covariance function with a reference cross-covariance function. The travel time τ between points \mathbf{x}_1 and \mathbf{x}_2 is defined as

$$\tau(\mathbf{x}_1, \mathbf{x}_2) = h_t \sum_t W(\Delta, t) [C(\mathbf{x}_1, \mathbf{x}_2, t) - C^0(\Delta, t)] \quad (1.9)$$

where C^0 is a reference cross-covariance function, $\Delta = \mathbf{x}_2 - \mathbf{x}_1$, and $W(\Delta, t)$ is a weight function.

The one-parameter fit is more robust with respect to noise but if the outliers are removed the noise in the travel times is similar for both methods (Roth et al., 2007). On the other hand, the Gabor wavelet fitting provides information not only about the travel time but also about the amplitude, the frequency, and the frequency bandwidth which may be important when acoustic waves interact with magnetic fields.

Travel-time perturbations

In the ray approximation, the acoustic travel times are sensitive only to perturbations along the ray paths. This is generally a good approximation in the limit of short wavelengths and high frequencies. It can be shown (Kosovichev & Duvall, 1997) that to the first-order approximation the difference and the mean of acoustic travel time perturbations due to structural inhomogeneities and flows of reciprocal paths along a ray are given by

$$\delta\tau_{\text{diff}} = -2 \int_{\Gamma} \frac{\mathbf{n}\mathbf{V}}{c^2} ds \quad (1.10)$$

$$\delta\tau_{\text{mean}} = - \int_{\Gamma} \left[\frac{\delta c}{c} \frac{k}{\omega} + \frac{\delta\omega_{ac}}{\omega_{ac}} \frac{\omega_{ac}^2}{c^2\omega^2} \frac{\omega}{k} + \frac{1}{2} \frac{k}{\omega} \left(\frac{c_A^2}{c^2} - \frac{(\mathbf{k}\mathbf{c}_A)^2}{k^2 c^2} \right) \right] ds \quad (1.11)$$

where \mathbf{n} is a unit vector tangent to the ray, \mathbf{V} is the flow velocity, $\mathbf{c}_A = \mathbf{B}/\sqrt{4\pi\rho}$ is the Alfvén velocity, and \mathbf{B} is the magnetic field. The last equation indicates that the mean travel time perturbation depends on the angle between the wave vector \mathbf{k} and the magnetic field \mathbf{B} . Anisotropy in the mean travel-time perturbations could indicate the direction of the magnetic field, although such an anisotropy has not been detected yet.

1.3 Data

Data from Michelson Doppler Imager (MDI) onboard the Solar and Heliospheric Observatory (SOHO) and Heliospheric and Magnetic Imager (HMI) onboard the Solar Dynamics Observatory (SDO) were mainly used in this dissertation. We describe in this section the MDI and HMI instruments, the observables, and the measurement techniques. More information about the MDI and HMI instruments can be found in

Scherrer et al. (1995), Scherrer et al. (2012), and Schou et al. (2012).

1.3.1 SOHO/MDI

The Solar and Heliospheric Observatory is a project of international cooperation between the European Space Agency (ESA) and the National Aeronautics and Space Administration (NASA). It was launched in December 1995 and placed in orbit around the Sun-Earth L1 point. The spacecraft was originally designed as a two-year mission, but it continues to operate until now, almost 17 years after launch.

The Michelson Doppler Imager is one of the instruments onboard SOHO collecting data for helioseismic and magnetic-field studies. MDI consists of the optics package and the electronics package. Here, we will only describe the optics package (Figure 1.7). A refracting telescope feeds sunlight through a series of filters onto a CCD camera. The telescope, with a 12.5 cm primary lens and a secondary (enlarging) lens, has an effective focal length of 1867 mm. The optical elements in the filter system include the front window, the blocking filter, the Lyot filter, and two Michelson interferometers. All of the filters, except for the front window, are located inside a very precisely temperature-controlled oven. The full width at half maximum (FWHM) of the filters is: 50 Å for the front window, 8 Å for the blocking filter, 465 mÅ for the Lyot filter, and 188 mÅ and 94 mÅ for the Michelson interferometers. The 94 mÅ bandpass of Michelsons can be tuned with rotating waveplates across the Ni I 6768 Å mid-photospheric absorption line, which is used for the measurements. The CCD is a front-side illuminated, 3-phase 1024×1024 array with 21 micron square pixels, which is read out at 0.5 Mpixels per second.

MDI records filtergrams, images of the solar photosphere in well-defined wavelength bands and polarization states, and produces measurements of line-of-sight velocity, line and continuum intensity, and magnetic field. The observables are computed from five filtergrams, labeled F_0 through F_4 , equally spaced by 75 mÅ. F_0 is nearly continuum, F_1 and F_4 are centered on the wings, and F_2 and F_3 are centered

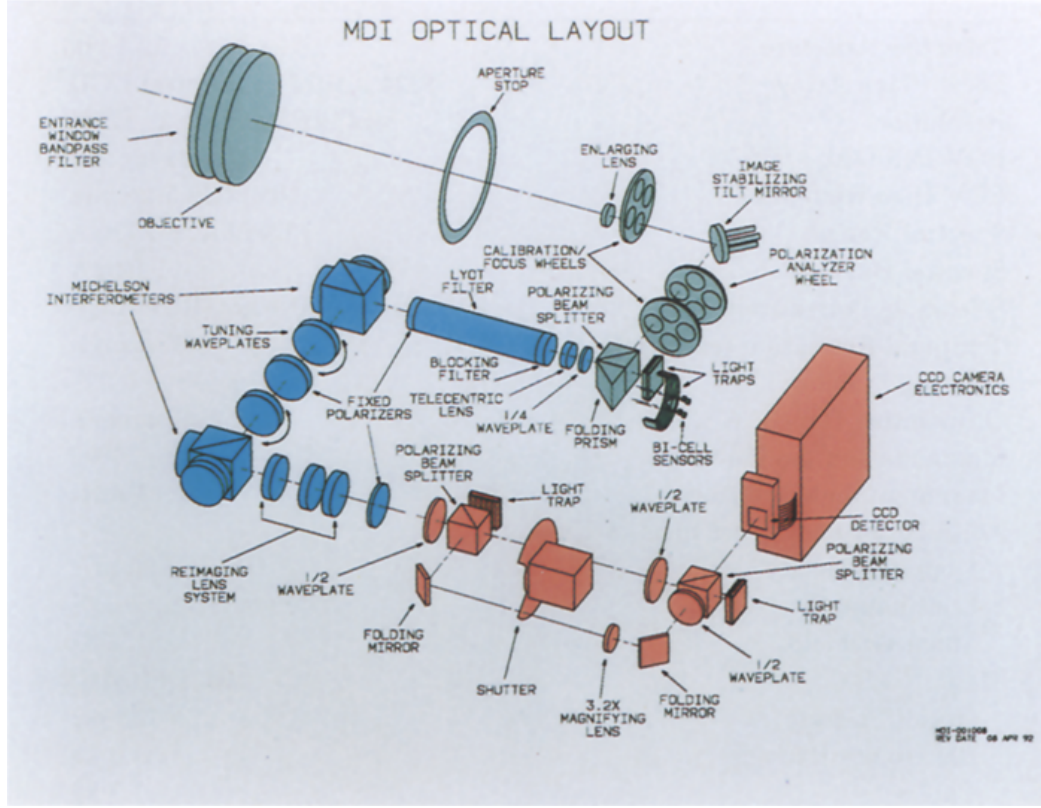


Figure 1.7: Optical layout of Michelson Doppler Imager. Figure adopted from Scherrer et al. (1995).

about the core of the center-of-disc Ni line. The Doppler velocity is estimated from α

$$\alpha = \begin{cases} (F_1 + F_2 - F_3 - F_4)/(F_1 - F_3), & \text{if numerator} > 0 \\ (F_1 + F_2 - F_3 - F_4)/(F_4 - F_2), & \text{if numerator} \leq 0 \end{cases} \quad (1.12)$$

using a lookup table constructed from simulations using parameterized solar line profiles and the measured filter transmission profiles. Doppler shift measurements of right and left circularly polarized light are used to estimate the longitudinal magnetic field. The Doppler shift difference of these two polarization states is a measure of the Zeeman splitting and is roughly proportional to the magnetic flux density. The 1σ noise levels of MDI measurements are 20 m/s for the Doppler velocity and 20 G for the longitudinal magnetic field.

MDI has 3 observing programs: the Structure Program, the Dynamics Program, and Campaigns. In this dissertation, we have used data only from the Structure and the Dynamics Program. The Structure Program is the basic observing mode, which runs continuously and produces low resolution Dopplergrams with a size of 192×192 pixels and a temporal cadence of 1 minute. The Dynamics Program runs for 2-3 months each year producing higher resolution Dopplergrams with a size of 1024×1024 pixels and a temporal resolution of 1 minute. More details about the data used in our studies are given in the following chapters.

1.3.2 SDO/HMI

The Solar Dynamics Observatory is the first mission of NASA's Living With a Star (LWS) program. It was launched in February 2010 and placed in geosynchronous orbit at an altitude of 36,000 km. The spacecraft was designed as a five-year mission and until now it continues to operate normally.

The Helioseismic and Magnetic Imager, which extends the capabilities of MDI, is one of the three instruments onboard SDO. MDI and HMI instruments have similar structure and the description here is mainly a comparison of the two instruments and not a detailed description of HMI instrument. HMI consists of the optics package, an electronics box, and a harness to connect the two. The main telescope is a two-element refracting telescope with a 14.0 cm clear aperture. The front window has a FWHM of 50 Å and its main purpose is to limit the heat input to the instrument. A particular concern for the front window is the focus change due to a very large temperature perturbation when going in and out of eclipses. The rest of the filter system includes a blocking filter, a Lyot filter, and two Michelson interferometers and enables narrow-band filtergrams to be made across the Fe I 6173 Å line. HMI's blocking filter has the same FWHM with that of MDI, 8 Å. The Lyot filter has the same basic design as the MDI filter with the addition of a tuned element in order to accommodate the wide range in radial velocity due to the geosynchronous orbit of SDO. The FWHM of the untuned part is 612 mÅ and that of the tunable element is 344 mÅ. The Michelsons with FWHM of 172 mÅ and 86 mÅ are tuned by rotating a

combination of two half-wave plates and a polarizer. This design has the advantage that any one of the three mechanisms can fail without impacting the ability to tune either Michelson. HMI has also two identical front-side illuminated CCD detectors with a 4096^2 pixel format and $12\ \mu\text{m}$ pixels. The CCDs have a readout rate of 2 Mpixels per second.

HMI observables are calculated from 12 filtergrams taken at 6 wavelengths equally spaced by $69\ \text{m}\text{\AA}$ (Figure 1.8) and 2 polarizations (left-circular and right-circular polarizations). The calculations of observables, which is based on the MDI-like algorithm (Couvidat et al., 2012), is performed on the ground and not onboard the satellite. The line-of-sight observables include Doppler velocity, magnetic field strength, and Fe I line width, line depth, and continuum intensity. The expected 1σ noise level of HMI Doppler velocity is less than 20 m/s for velocities up to about 6 km/s and for distances up to about $0.3\ R_\odot$ away from disc center (Schou et al., 2012).

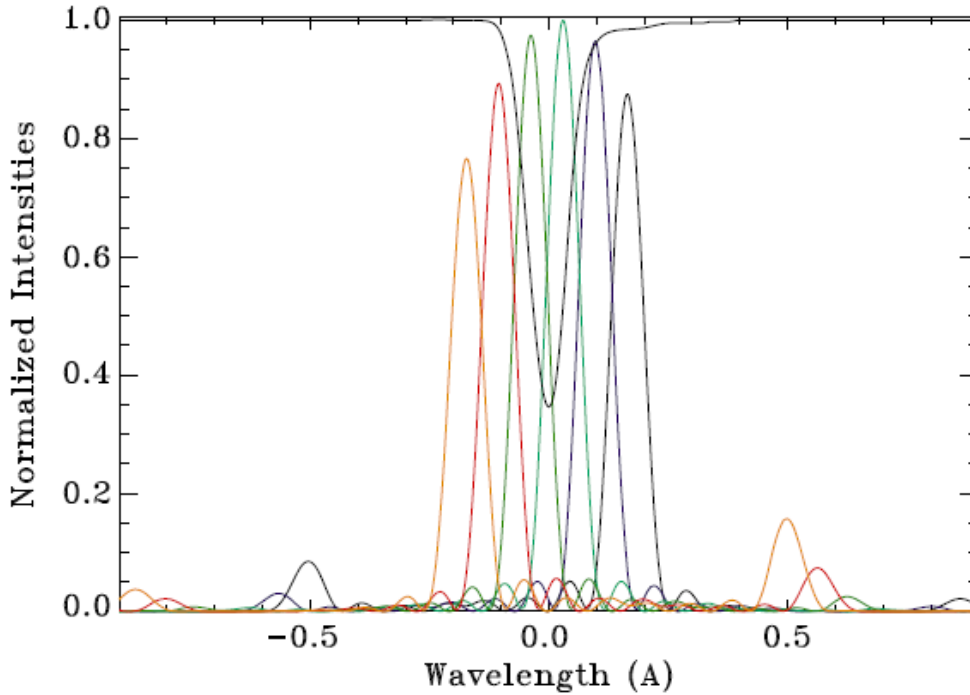


Figure 1.8: Example of HMI tuning-position profiles with respect to the Fe I solar line at disk center and at rest. Figure adopted from Schou et al. (2012).

HMI provides data with higher temporal and spatial resolution than MDI. The full-disc Doppler velocity and line-of-sight magnetic flux images used in this dissertation are available every 45 seconds with a spatial resolution of 0.03 heliographic degrees at disc center. These continuous high-resolution observations are particularly useful for local helioseismology studies. Although the majority of results in this dissertation were obtained with MDI data, the analysis methods are applicable to HMI data as well.

1.4 Motivation

Sunspots are perhaps the most interesting features on the solar surface. These magnetic regions are manifestations of the dynamo mechanism that generates the solar magnetic field and their appearance on the solar surface is linked with the solar activity and the phases of the solar cycle. Sunspots naturally attracted the interest of solar physicists and became object of intense scientific exploration. There are systematic observations of sunspots for about 400 years whereas sporadic observations extend for thousands of years. Despite the long efforts to understand how sunspot regions are generated in the solar interior and emerge in the photosphere, there is still no definitive answer on the depth of magnetic-field generation and the process of magnetic field emergence is not yet well understood. From an observational point of view, little progress has been made in the investigation of magnetic flux emergence in the solar convection zone. Helioseismology, which is primarily responsible to explore the interior of the sun, encountered difficulties in detecting pre-emergence signatures of sunspot regions and thus sunspots cannot be expected before they become visible in the photosphere.

Not only the origin and emergence of sunspot regions is not well understood but also many physical effects that take place in sunspot regions have not been quantitatively determined yet. There are several ways that the strong magnetic field of sunspot regions can affect the acoustic waves that propagate close to these magnetic regions. Acoustic waves are absorbed and the acoustic emissivity is reduced in

sunspots. In addition, the presence of strong magnetic fields affects the observed amplitude of solar oscillations even if the acoustic absorption and emissivity reduction are neglected. Since the basic tools of helioseismic studies are based on observations of solar oscillations and any inferences about the surface or subsurface properties of sunspots uses these observations, it is important to obtain quantitatively estimates of these effects.

Sunspot regions are also associated with very complex and energetic eruptive events. These events may have significant impact on the interplanetary space and change the space weather conditions in the near-Earth environment. It is a major task of space weather forecasting to monitor the solar magnetic activity and forecast the emergence of sunspot regions as well as the eruptive events that occur in these regions. In addition to sunspots which are already visible in the photosphere, sunspots emerging from the Sun's east solar limb and the subsurface layers may produce flares and CMEs and impact the Earth as well as space satellites. Thus, monitoring the subsurface and far-side magnetic activity is a useful tool for space weather forecasters.

Motivated by scientific curiosity about the nature of sunspots and space weather forecasting needs, we perform, in this dissertation, a helioseismic study on the detection of sunspots. The main goal is to detect sunspot regions before they become visible on the solar disc and make quantitatively estimates of the value of physical quantities, such as absorption and emissivity reduction, that affect the acoustic wave propagation in sunspot regions. The results of this study improve our understanding of surface and subsurface properties of sunspots and benefit space weather forecasts.

Chapter 2

Solar Far-Side Imaging¹

The mapping of far-side active regions was first made possible using the helioseismic holography technique by use of four-skip acoustic signals. The quality of far-side images was later improved with the combination of four- and five-skip signals using helioseismic holography and time-distance technique. In this work, we explore the possibility of making three-skip far-side images using the time-distance technique, and improving the quality of far-side maps obtained from the existing time-distance method.

2.1 Introduction

The detection of large solar active regions on the far side of the Sun can improve space-weather forecasting and facilitate the study of evolution of those active regions. Active regions that appear on the east solar limb can affect space weather, causing problems in spacecraft, electrical power grids, and telecommunications. Monitoring the solar far-side activity enables the anticipation of large active regions by more than a week before they rotate into our view from the Sun’s east limb.

The first attempt to map the central region of the solar far side was made by Lindsey and Braun (2000a) by use of the helioseismic-holography technique (Lindsey

¹Most part of this chapter was published in Solar Physics (Ilonidis, Zhao, & Hartlep, 2009)

and Braun, 2000b). Low- and medium- ℓ acoustic waves exhibit an apparent travel-time deficit in solar active regions, which is detectable by phase-sensitive holography (Braun and Lindsey, 2000). This technique initially included only double-skip acoustic signals but was later extended (Braun and Lindsey, 2001) to map the whole far side using single- and triple-skip signals.

The time-distance helioseismology technique also has the capability to map the central area of the solar far side (Duvall, Kosovichev, and Scherrer, 2000; Duvall and Kosovichev, 2001). The mapping area was later extended onto the whole far side using four- and five-skip acoustic signals (Zhao, 2007). The two schemes are used separately to make two whole far-side maps. The combination of the two maps gives far-side images with better signal-to-noise ratio. This is an independent solar far-side imaging tool in addition to the holography technique, which allows for the possibility to cross-check the active regions seen in both time-distance and helioseismic holography techniques and hence improves the accuracy of monitoring the solar far-side active regions.

However, no studies have been carried out yet to explore the possibility of making far-side images using acoustic signals with three skips. Here we apply the time-distance technique to show that it is possible to image the solar far side utilizing three-skip acoustic signals, and we discuss advantages and disadvantages of this method. We also suggest a method to improve the quality of existing far-side images that includes the results of our work.

2.2 Data and Technique

The medium- ℓ program of the *Solar and Heliospheric Observatory* / Michelson Doppler Imager (SOHO/MDI) (Scherrer *et al.*, 1995) is used in this work. The oscillation modes that are observed range from $\ell = 0$ to ≈ 300 , and the data are acquired with a one-minute cadence and a spatial sampling of $10''$ (0.6 heliographic degrees per pixel at disc center). The $\ell - \nu$ power spectrum diagram of this dataset is shown in Figure 2.1a. The continuity of the observations and the particular range of modes that we analyze make the SOHO/MDI medium- ℓ data ideal for solar far-side

imaging.

The time-distance technique is able to detect acoustic signals that travel to the far side and return to the front side after experiencing four and five skips (Zhao 2007). It is useful to examine whether acoustic signals after three skips are also detectable by this technique. In Figure 2.1b the time-distance diagram is computed using all oscillation modes from a 2048-minute MDI medium- ℓ dataset with a spatial size of $120^\circ \times 120^\circ$ after the region is tracked with the Carrington rotation rate and is remapped using Postel’s projection with the solar disk center as the remapping center. The diagram shows acoustic skips of up to seven times on the front side as well as signals traveling to the far side and returning to the front side after three and four skips. From all of these signals we keep only the ones that are needed in our analysis and filter out all other acoustic modes. The acoustic signals that are needed should have long single-skip travel distance corresponding to low- ℓ modes. Such a filtering improves the signal-to-noise ratio at the required travel distances of the three-skip method. Figure 2.1c shows the time-distance diagram computed using only the useful acoustic modes within a box of ℓ -range $6 - 15$ at 2.5 mHz and $12 - 30$ at 4.5 mHz. This filtering is applied to the data after Postel’s projection and thus it works best where the geometry is least distorted. Another issue is that the theoretical travel time is a few minutes off from the time-distance group travel time after three skips, because as pointed out by Kosovichev and Duvall (1996) and Duvall *et al.* (1997), the ray-approximated travel time is a few minutes off from the time-distance group travel time.

Not all acoustic signals that come back from the far side after three skips are used but only those with time-distance annulus radii $80^\circ - 113^\circ$ from the target point for the single-skip and $160^\circ - 226^\circ$ for the double-skip (see Figure 2.2). This scheme is able to cover the whole far side except for a circular region in the center of that side. Following Zhao (2007) to save computation time, only the areas lower than the latitude of 48° , where nearly all active regions are located, are included in the far-side imaging computations.

The first step of the computational procedure is to track a 2048-minute long MDI medium- ℓ dataset with the Carrington rotation rate. Then it is remapped to

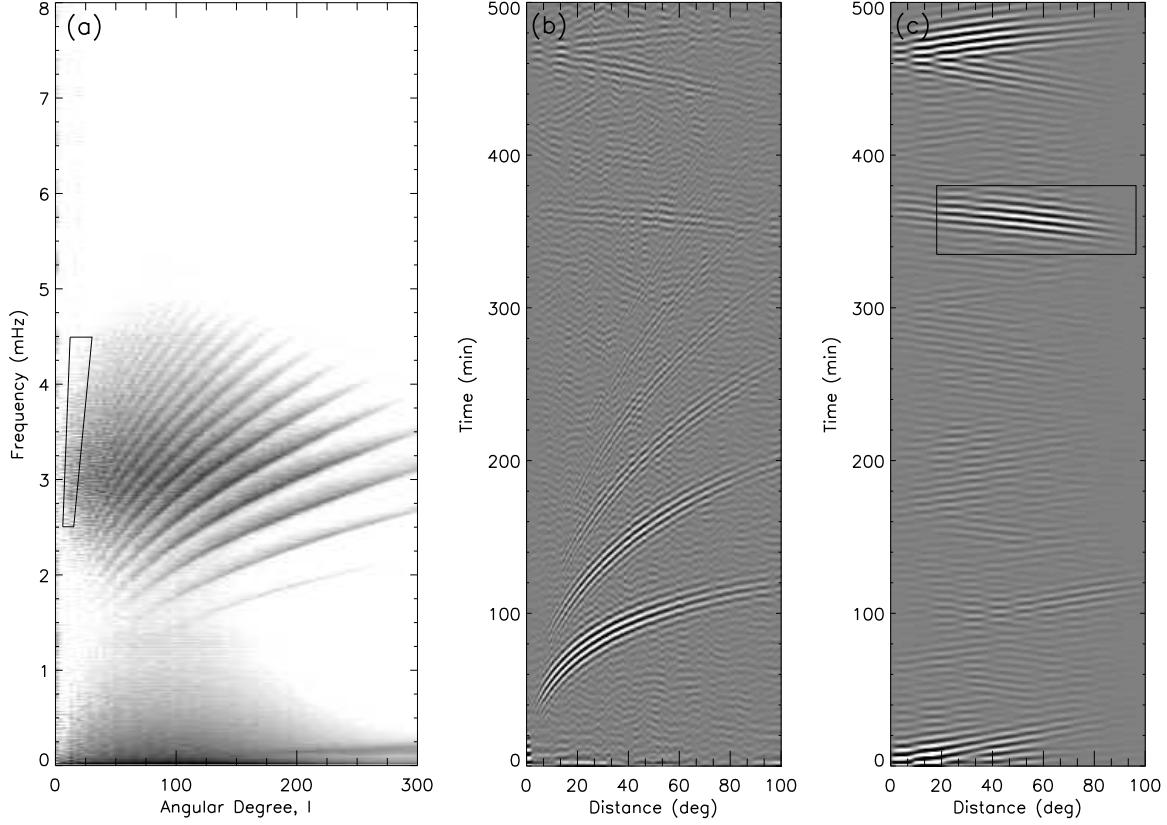


Figure 2.1: (a) Power spectrum computed from a 2048-minute MDI medium- ℓ dataset. The black box includes oscillation signals with ℓ -range 6 – 15 at 2.5 mHz and 12 – 30 at 4.5 mHz which are used in our computations. (b) time-distance diagram computed using the whole power spectrum of the same dataset, and (c) time-distance diagram computed using only the oscillations that have frequency and ℓ included in the black quadrangle as indicated in (a). The black box delimits the acoustic travel distances and times used for far-side imaging. Figure adopted from Ilonidis, Zhao, & Hartlep (2009).

Postel’s coordinates centered on the solar disk with a spatial sampling of 0.6° per pixel, covering a span of 120° along the Equator and the central meridian. This dataset is filtered in the Fourier domain and only the oscillation modes with travel distances in agreement with the distances listed above are kept (see Figure 2.1). Corresponding pixels in the annuli on both sides of the target point are selected and the cross-covariances with both positive and negative travel-time lags are computed. Then both time lags are combined and all cross-covariances obtained from different

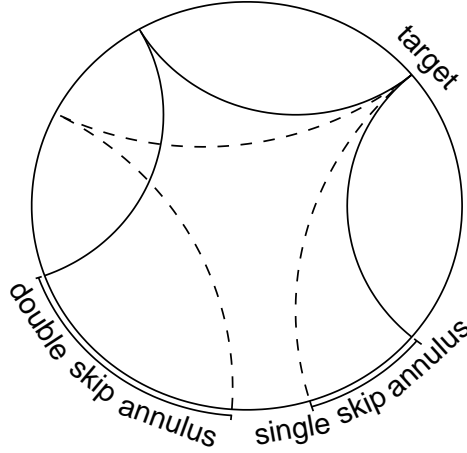


Figure 2.2: Three-skip measurement scheme where one set of single-skip and one set of double-skip rays are located on either side of the target point. The figure shows the equatorial plane with the upper half corresponding to the far side of the Sun and the lower part corresponding to the front side. Figure adopted from Ilonidis, Zhao, & Hartlep (2009).

distances after appropriate shifts in time are also combined. The final cross-covariance is fitted with a Gabor wavelet function (Kosovichev and Duvall, 1996) and an acoustic phase travel time is obtained. The far-side image is a display of the measured mean acoustic travel times after a Gaussian smoothing with a FWHM of 2.0° .

2.3 Results

2.3.1 Results from Numerical Simulation Data

Comparing the far-side images with the directly-observed near side after active regions have rotated into our view from the far side, or before they rotate out of view onto the far side, is the traditional way to evaluate the accuracy of far-side images. However, active regions sometimes develop rapidly, on time scales of days, thus the traditional way is not always sufficient. A different approach is based on comparisons of far-side maps with STEREO observations of far-side solar activity (Liewer et al., 2012). Numerical models of solar oscillations can provide artificial data with near-surface perturbations mimicking active regions on the far side of the Sun. Applying

helioseismic-imaging techniques on the simulated wavefield allows for a direct comparison of the far-side images with the prescribed sound-speed perturbations, and it thus provides an accurate test of the far-side imaging technique.

We present results on testing the new time-distance technique with three-skip acoustic signals. The sensitivity of the technique is tested by varying the size of the active region. The propagation of solar acoustic waves is simulated numerically in a spherical domain. The simulations take into account the effects of a spatially-varying sound speed but for now ignore flows and magnetic fields. The quiet solar medium is represented with a sound speed that is only a function of radius given by the standard solar model S of Christensen-Dalsgaard *et al.* (1996) matched to a chromospheric model from Vernazza, Avrett, and Loeser (1981). Active regions are modeled as local variations in the sound speed from the quiet Sun. The depth profile of these variations can be found in Hartlep *et al.* (2008). The data are prepared to be similar to MDI medium- ℓ data and have been used to test the existing four- and five-skip far-side imaging technique (Hartlep *et al.*, 2008). The radial velocity is computed at a location 300 km above the photosphere and is stored with one-minute cadence and a spatial resolution of $0.703^\circ \text{ pixel}^{-1}$. The data are remapped onto Postel’s coordinates with a spatial sampling of $0.6^\circ \text{ pixel}^{-1}$. A region of $120^\circ \times 120^\circ$ is used for analysis and the first 500 minutes are discarded because they represent transient behavior. The following 1024 minutes are used in the analysis, a short but sufficient period for far-side analysis. The rest of the procedure for the simulation data is the same as for the observations. For more details about the simulation and for discussion on how these simulations were used for testing far-side imaging, see Hartlep *et al.* (2008).

We have used simulated data for two active-region sizes, a large one with a radius of 180 Mm and a smaller one with a radius of 90 Mm. A circular area around the center of the far side with a radius of 24° as well as a band along the solar limb 15° in width have been excluded from the far-side map because the three-skip technique is not able to fully cover these areas. As seen in the left image of Figure 2.3, the three-skip scheme can clearly detect the large active region but with some level of uncertainty in the location as well as the shape of the region. The detection of the

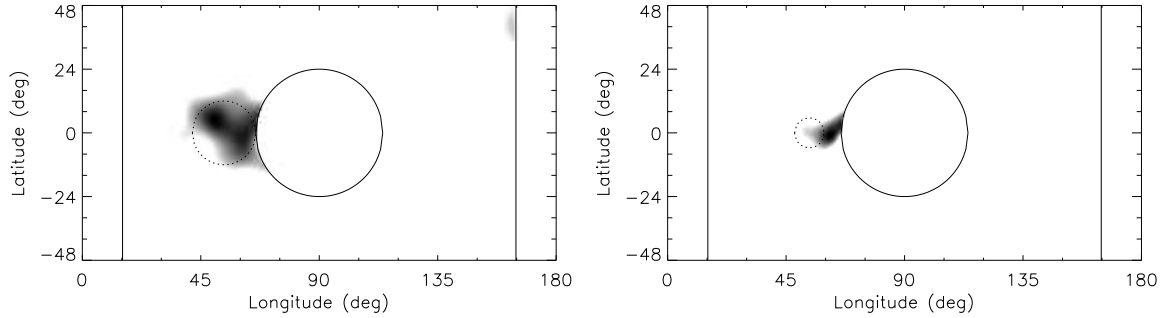


Figure 2.3: Far-side images for simulations with an active region with radius 180 Mm (left) and 90 Mm (right). The dotted circles indicate the sizes and locations of the active regions. Figure adopted from Ionidis, Zhao, & Hartlep (2009).

small active region by the three-skip scheme is shown in the right image of Figure 2.3. It is very encouraging that the far-side map is completely clear of spurious features. However, as in the previous case, the location and the shape are slightly different from the original region.

2.3.2 Results from MDI observations

We have applied our three-skip imaging technique to the numerical simulation data and found that this technique is able to recover active regions larger than at least 90 Mm in size, but unable to detect unambiguously features close to the far-side limbs and center due to the low, or no, acoustic wave coverage in these areas.

Next we make far-side images using MDI observational data. Two different datasets, each lasting 2048 minutes, with the middle time corresponding to 12:00 UT of 8 and 9 November 2003, are used for this purpose, and the corresponding maps are shown on the left side of Figures 2.4 and 2.5 respectively. In order to highlight the far-side active regions, the same maps are shown on the right side of Figures 2.4 and 2.5 after applying a travel-time threshold of -2.0σ . The threshold for the three-skip image is smaller (-1.5σ) because the standard deviation of this travel-time map is substantially larger than other maps averaged from two or three travel-time maps. In the first row of Figures 2.4 and 2.5, far-side images made with the new three-skip technique are displayed. In order to test the quality and accuracy

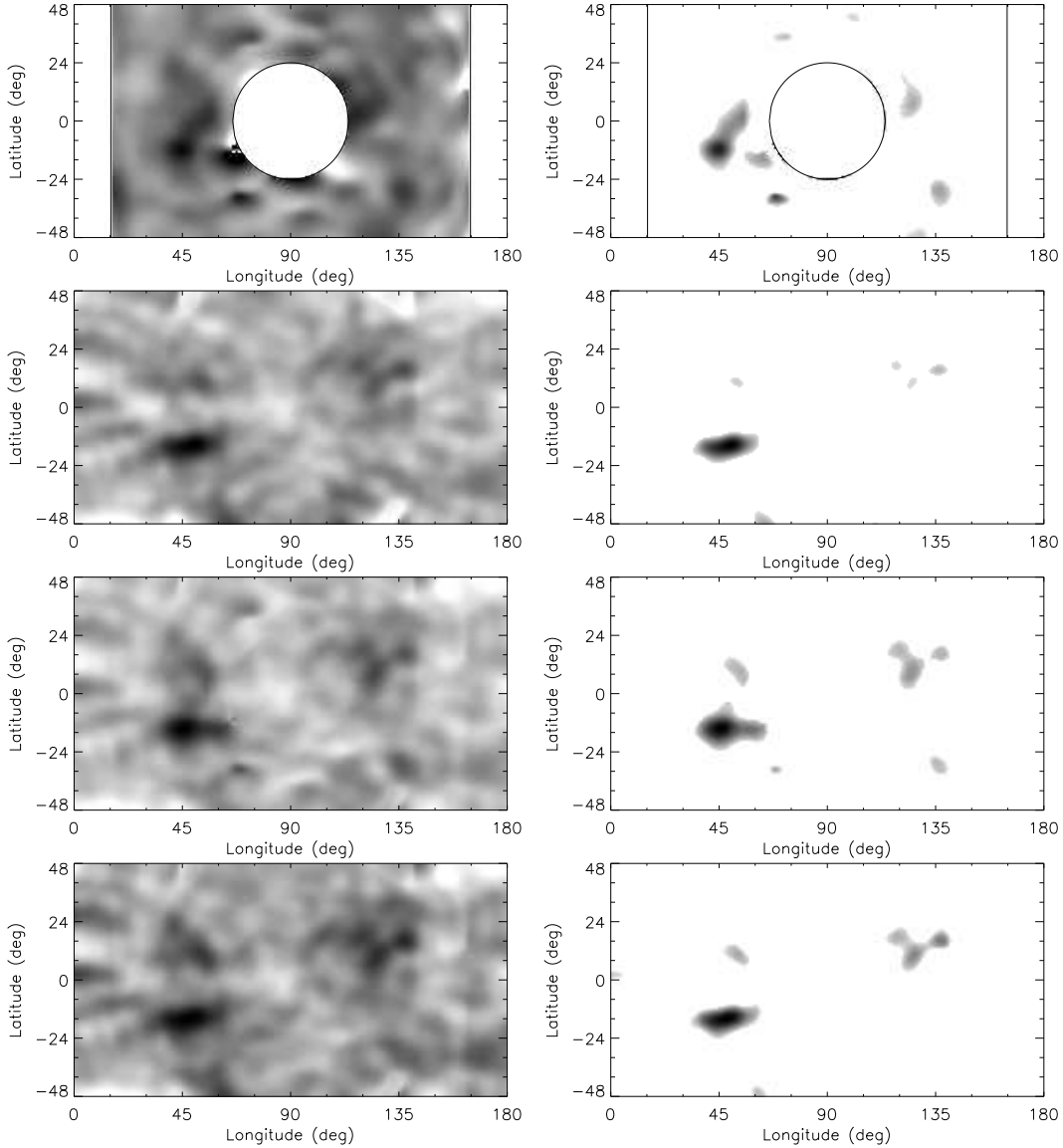


Figure 2.4: Results of time-distance far-side active region imaging, obtained from three-skip measurements (first row), combination of four- and five-skip measurements (second row), combination of three-, four-, and five-skip measurements by simple averaging (third row) and combination of three-, four-, and five-skip measurements by the new method of averaging (bottom row). On the right-side, images display the far-side map after applying a travel-time threshold of -2.0σ (-1.5σ for the three-skip map because the standard deviation is substantially larger) in order to highlight the far-side active regions that are of interest. Images are obtained for 8 November 2003. Figure adopted from Ilonidis, Zhao, & Hartlep (2009).

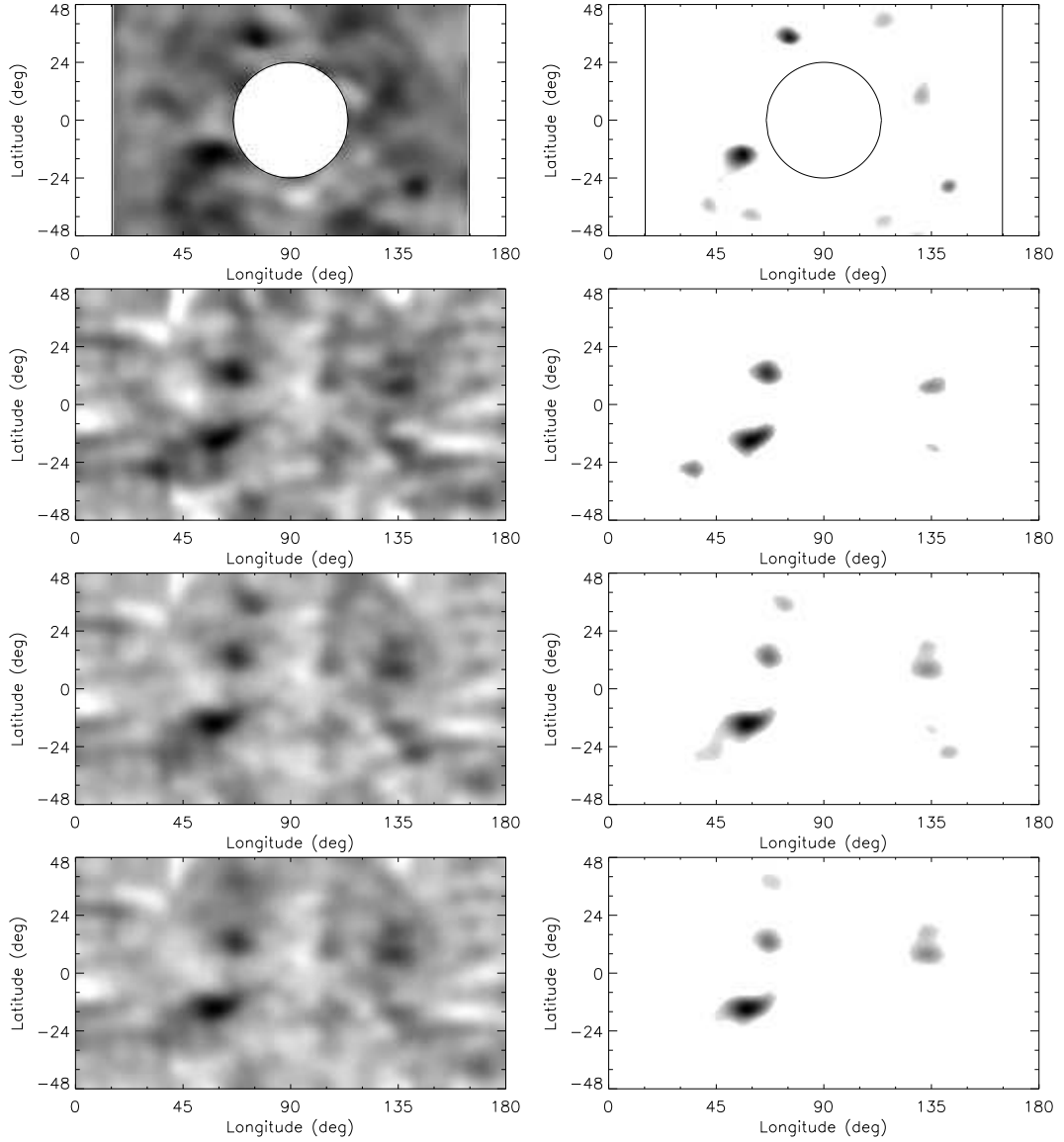


Figure 2.5: Results of time-distance far-side active region imaging, obtained from three-skip measurements (first row), combination of four- and five-skip measurements (second row), combination of three-, four-, and five-skip measurements by simple averaging (third row) and combination of three-, four-, and five-skip measurements by the new method of averaging (bottom row). On the right-side, images display the far-side map after applying a travel-time threshold of -2.0σ (-1.5σ for the three-skip map because the standard deviation is substantially larger) in order to highlight the far-side active regions that are of interest. Images are obtained for 9 November, 2003. Figure adopted from Ilonidis, Zhao, & Hartlep (2009).

of the new imaging technique, far-side images from the same dates made with the existing time-distance technique (Zhao, 2007) are shown in the second row. The third and fourth rows display far-side images made with a combination of three-, four-, and five-skip results, but the technique applied for the combination is different in each case, and it is further discussed in more details below.

The new far-side maps that utilize acoustic signals with three, four, and five skips consist of three distinct regions, two bands along the solar limbs 15° in width, a circular area around the center of the far side with a radius of 24° , and the rest of the far-side region. The imaging of the bands along the solar limbs is based only on acoustic signals with four skips. A combination of four- and five-skip acoustic signals is used for the central circular area, while for the rest of the far-side image the combination includes three-skip measurements in addition to the four- and five-skip measurements. The imaging of the existing far-side maps is based on a combination of four- and five-skip measurements except for two bands along the solar limbs where only four-skip measurements are used (see Zhao, 2007). The boundaries of all of those regions have been linearly smoothed over a distance of 12° . All of the far-side acoustic travel times are displayed after a mean travel-time background is removed.

As mentioned before, the two bottom rows of Figures 2.4 and 2.5 present far-side images made by combining three-, four- and five-skip measurement schemes. The method of combining images by simply taking the average is a rather simple but reasonable technique in the case of two images and is able to enhance the signal-to-noise ratio in the far-side images (Zhao, 2007). Therefore, the arithmetic average is used in the central circular area of the far side that involves only acoustic signals with four and five skips. However, more sophisticated techniques of combination can be applied if three or more far-side images are available. At each pixel location of the far-side map where there is overlap between the regions accessed by the different combinations of skip distances, the travel times obtained from the three-, four-, and five-skip images are considered and the absolute values of the three differences in the travel times are calculated. If the two largest differences are larger than a high threshold and the smallest difference is smaller than a low threshold then the travel time that is substantially smaller or larger is replaced by the average of the other

two. The travel time at those pixels that satisfy the above conditions is essentially the average of travel times of just two different measurement schemes. By setting the high threshold equal to 13 seconds and the low threshold equal to 9 seconds we have managed to remove spurious features from the far-side map and at the same time enhance the signal in the active regions. The two thresholds were selected after tests with MDI data of far-side active regions. The third and fourth rows of Figures 2.4 and 2.5 show respectively far-side maps made by simply averaging the three-, four-, and five-skip acoustic signals and by applying the new combination technique.

Both the new and the existing far-side imaging technique cannot give consistently a clear far-side map without any spurious features, but they can differ quantitatively as well as qualitatively. It is clear from Figure 2.4 and 2.5 that the level of noise in the three-skip image is quite high. If we simply average the three-, four-, and five-skip signals and compare the new far-side map with the existing map, the large active regions appear larger and more enhanced but spurious signals originating from the contribution of the noisy three-skip image also appear in the far-side map. However, the new combination technique is able either to completely remove some of those signals from the far-side map or at least to weaken their contribution. As a result the new far-side maps have a better signal-to-noise ratio with reduced and fewer artifacts.

Comparing corresponding maps we can conclude that the detection of large active regions is more successful with the new technique. The three-skip measurement scheme utilizes low- ℓ acoustic modes, lower than the ones used in the four- and five-skip schemes hence the wavelength of these modes is greater, and this results in a reduced sensitivity in the detection of small active regions. But even if the three-skip scheme completely failed to detect small active regions, the new combination technique ensures that in most cases these regions will be visible in the far-side map. On the other hand, increasing the total number of skips produces degradation in the signal correlations and, as we expect, the three-skip method has stronger correlations than the four- and the five-skip method. It is quite remarkable though that in some cases the three measurement schemes have spurious signals at the same locations, an indication that there might be some weak correlation in the noise of the far-side images, or alternatively, that “ghost-images” from near-side active regions appear on

the far side.

2.4 Discussion

The availability of both time-distance and helioseismic holography far-side maps makes the detection of active regions more robust and confident. Additionally, far-side imaging provides us with some experience in analyzing low- and medium- ℓ mode oscillations by the use of local-helioseismology techniques and this will help us in analyzing deeper solar interior and polar areas.

The time-distance technique with three-skip acoustic signals is another imaging tool in addition to the existing techniques. We have successfully made three-skip far-side images of the solar active regions using data from numerical simulations as well as from MDI observations. The three-skip measurement scheme cannot cover the whole far side, and moreover, the far-side images have many spurious features that do not appear in the four- and five-skip images. Consequently the three-skip images by themselves are not as good as the images obtained by other time-distance techniques. Our motivation for making three-skip far-side images derives from the fact that the availability of one more far-side imaging technique makes possible the application of more sophisticated methods of combining images than the simple arithmetic averaging. In addition, the correlations in the three-skip technique are rather strong and facilitate the detection of large active regions.

The combination of four- and five-skip measurement schemes was shown by Zhao (2007) to significantly enhance the signal-to-noise ratio of far-side acoustic travel-time measurements and make the resulting far-side map much cleaner. More specifically it helps to remove most, but not all, of the spurious features. On the other hand, it also removes some small active regions that can otherwise be seen in one map or the other. The three-skip scheme is an independent tool for imaging the far-side solar active regions, and thus it can be combined with the two existing time-distance techniques. The combination of the three measurements can give a cleaner far-side map, with fewer spurious features and enhanced active regions.

The method of combining images is very important in the problem of far-side

imaging. Here we present two different methods, the first one was also used by Zhao (2007) while the second one is a newly suggested method that improves the quality of the image. The new method utilizes, at each pixel location, the far-side maps derived from three-, four-, and five-skip travel times, subject to two arbitrary thresholds. Properly adjusting these thresholds, it is possible to enhance the active regions and reduce the level of noise. In addition, combination of the time-distance far-side images with the helioseismic holography images, which are available through the SOI/MDI webpage http://soi.stanford.edu/data/full_farside/, may further improve the quality of these images.

Chapter 3

Measurements of Absorption, Emissivity Reduction, and Local Suppression Coefficients in Sunspot Regions¹

The power of solar acoustic waves is reduced inside sunspots mainly due to absorption, emissivity reduction, and local suppression. By analyzing 47 active regions observed by SOHO/MDI without using signal filters, we have determined the coefficients of surface absorption, deep absorption, emissivity reduction, and local suppression. The dissipation in the quiet Sun is derived as well. We find that absorption is the dominant mechanism of the power deficit in sunspots for short travel distances, but gradually drops to zero at travel distances longer than about 6° . The absorption in sunspot interiors is also significant. The emissivity-reduction coefficient ranges from about 0.44 to 1.00 within the umbra and 0.29 to 0.72 in the sunspot, and accounts for only about 21.5% of the umbra's and 16.5% of the sunspot's total power reduction. Local suppression is nearly constant as a function of travel distance with values of 0.80 and 0.665 for umbrae and whole sunspots respectively, and is the major cause of the power deficit at large travel distances.

¹Most part of this chapter was published in Solar Physics (Ilonidis & Zhao, 2011)

3.1 Introduction

Solar oscillations have lower amplitude in sunspots than in the quiet Sun (Leighton, Noyes, and Simon, 1962; Lites, White, and Packman, 1982). The observed power reduction is caused by several mechanisms which here are grouped in three categories: absorption, emissivity reduction, and local suppression, as categorized by Chou *et al.* (2009c).

The first category, absorption, includes three different mechanisms: *i*) acoustic wave energy is converted into heat (Hollweg, 1988; Lou, 1990; Sakurai, Goossens, and Hollweg, 1991; Goossens and Poedts, 1992), *ii*) acoustic waves are converted into modes that cannot be detected in the photosphere (Spruit and Bogdan, 1992; Cally and Bogdan, 1993; Cally, Bogdan, and Zweibel, 1994; Crouch and Cally, 2005; Gordovskyy and Jain, 2008), *iii*) wave leakage to the outer atmosphere is enhanced due to the modification of the acoustic cut-off frequency. The second category is emissivity reduction. The reduction in convection in sunspots leads to reduced excitation of acoustic waves (Hurlburt and Toomre, 1988; Parchevsky and Kosovichev, 2007). The last category, local suppression, is a local change in observed wave amplitude, rather than a change in energy. Several mechanisms also fall into this category. The observed amplitude reduction may be caused by: *i*) Wilson depression (Hindman, Jain, and Zweibel, 1997), *ii*) altered eigenfunctions (Hindman, Jain, and Zweibel, 1997), *iii*) a greater wave speed, and *iv*) a change in the line profile (Wachter, Schou, and Sankarasubramanian, 2006; Rajaguru *et al.*, 2007). For more details on each mechanism see Hindman, Jain, and Zweibel (1997) and Chou *et al.* (2009a, 2009b).

Braun, Duvall, and LaBonte (1987, 1988), Bogdan *et al.* (1993), and Chen, Chou, and the TON team (1996) found, using Hankel analysis and spherical decomposition of the acoustic wavefield, that sunspots absorb as much as 50% of the incoming acoustic waves. This method includes decomposition of the *p*-mode oscillations into inward and outward propagating modes with respect to the sunspot. However, the effects of absorption and emissivity reduction cannot be distinguished, and, additionally, local suppression is not included in such measurements.

The first attempt to distinguish and determine the three coefficients of absorption,

emissivity reduction, and local suppression was made by Chou *et al.* (2009b, 2009c). For this purpose they used the property that the waves emitted along the wave path between two points have no correlation with the signal at the starting point. Their technique makes use of direction and phase-velocity filters, which successfully allow measurements of the three above coefficients for specific acoustic wave-travel distances.

In this work we use a similar yet new method, which does not make use of the direction and phase-velocity filters to determine the coefficients of absorption, emissivity reduction, and local suppression. Instead, we use many active regions to increase the signal-to-noise ratio. The measurement procedure, in the absence of those filters, is more general and does not depend on the particular characteristics of the filters. More specifically, the absence of the phase-velocity filter allows the determination of all three parameters as functions of travel distance from active regions, while the absence of direction filter does not raise any questions regarding the width of the filter. This issue is important in some steps of the measurement procedure such as the correction for the dispersion of acoustic waves. On the other hand, the use of many active regions limits our method to an averaged measurement of absorption, emissivity reduction, and local suppression inside active regions only as functions of travel distance from the center of the regions but not as functions of direction.

3.2 Method

The energy budget of acoustic waves propagating through the quiet Sun and a sunspot is illustrated in Figure 3.1. The energy of a wave packet associated with a particular travel distance and propagating in a particular direction in the quiet Sun is constant and is denoted here by I . As the waves propagate through the solar medium in the top diagram of Figure 3.1, the acoustic energy after one skip is reduced by a factor of $(1 - d(r))$ due to dissipation, where d is the dissipation coefficient in the quiet Sun and r is the one-skip travel distance. At the same time new waves with energy $e(r)I$ are generated by turbulent convection where $e(r)$ is the emissivity coefficient in the quiet Sun. Since the acoustic energy is constant in the quiet Sun, $e(r) = d(r)$.

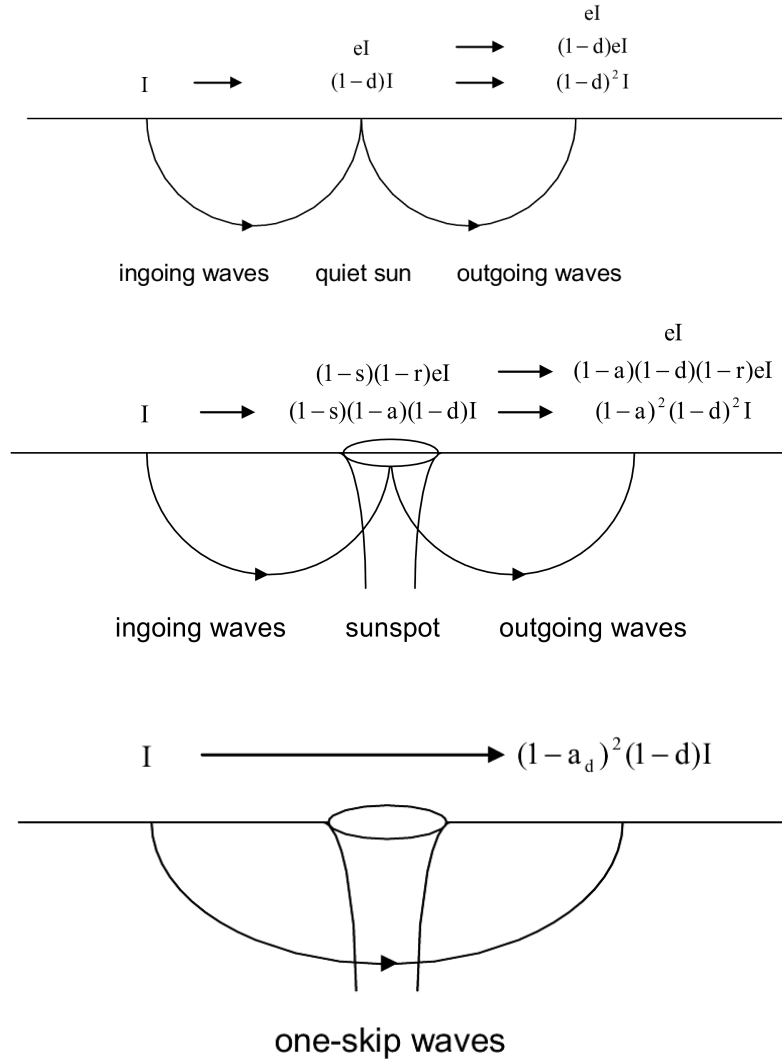


Figure 3.1: Energy budget of ingoing, outgoing, and double-skip waves propagating through the quiet Sun (top), ingoing, outgoing, and double-skip waves propagating through a sunspot (middle), and one-skip waves propagating through a sunspot (bottom). Only terms connected by arrows correlate. Figure adopted from Ilonidis & Zhao (2011).

For the two signals, $(1 - d(r))I$ and $e(r)I$, only the first one correlates with the signal I because $e(r)I$ is generated near the location of reflection by a different source. We use the above property to determine the dissipation of acoustic waves $d(r)$ in the quiet Sun. If the energy I of the acoustic waves is reduced by a factor of $(1 - d(r))$ after each skip, the energy of the same signal after n skips will be $(1 - d(r))^n I$. Using the definition of cross-covariance between two points as given in Equation (3.1), we compute the ratio of amplitude of the cross-covariance at the fifth skip, F_5 , to that at the first skip F_1 . Here the wave function Ψ is the square root of the energy. According to Equation (3.1), $F_5 = (1 - d)^{5/2} I$ and $F_1 = \sqrt{(1 - d)} I$. Equation (3.2) gives the dissipation in terms of F_5 and F_1 . The exact computational procedure used to determine $d(r)$ is described in the second paragraph of Section 3.3.

$$F_{12}(\tau) = \sum_t \Psi_1(t) \Psi_2(t + \tau) \quad (3.1)$$

$$d(r) = 1 - \left(\frac{F_5}{F_1} \right)^{1/2} \quad (3.2)$$

For the energy budget of the acoustic waves in the sunspot, we follow the model suggested by Chou *et al.* (2009c) but incorporate a minor modification. According to this model the terms $(1 - d(r))I$ and $e(r)I$ that were mentioned before in the quiet Sun are reduced by the factors $(1 - a(r))(1 - s(r))$ and $(1 - s(r))(1 - r(r))$ respectively inside the sunspot, where a is the absorption coefficient, r is the emissivity reduction coefficient, and s is the local suppression coefficient. After one more skip, the acoustic waves propagate outside the sunspot in the region of the quiet Sun. Both terms are further reduced by a factor of $(1 - a(r))(1 - d(r))$ and amplified by a factor of $(1 - s(r))$ because local suppression disappears outside the sunspot. At the location of the second skip, in addition to the terms described above, new waves with energy $e(r)I$ are generated by turbulent convection. For more details of this model see Chou *et al.* (2009c).

We consider now a reference point on the surface of the quiet Sun. Using the definition of cross-covariance as given in Equation (3.1), we compute the amplitude of cross-covariances of ingoing, outgoing, and two-skip waves with respect to the

reference point as functions of travel distance from that point. The two-skip waves have a reflection located in the reference point. The exactly same procedure is applied to the case of a sunspot where the reference point is always inside the sunspot. Considering the ratios of amplitude of the cross-covariance for the ingoing, outgoing and two-skip waves in the sunspot to that in the quiet Sun, we have a closed system of three equations with three variables: absorption, emissivity reduction, and local suppression. By computing ratios of measured values in the sunspots to that in the quiet Sun, we have avoided normalizing our computations (see Chou et al., 2009b for details of normalization). The cross-covariances of ingoing, outgoing, and two-skip waves for the quiet Sun and the sunspot are given in Equations (3.3)–(3.8). The solution of the system is given in equations (3.9)–(3.11). We should note here that although the waves in Figure 3.1 are associated with a particular travel distance, the coefficients of absorption, emissivity reduction, and local suppression, as defined in Equations (3.9)–(3.11) are functions of the travel distance r . We have

$$F_{\text{out}}^q = \sqrt{1 - d}I \quad (3.3)$$

$$F_{\text{in}}^q = \sqrt{1 - d}I \quad (3.4)$$

$$F_{2\text{skip}}^q = (1 - d)I \quad (3.5)$$

$$F_{\text{in}}^s = \sqrt{(1 - s)(1 - a)(1 - d)}I \quad (3.6)$$

$$F_{\text{out}}^s = \sqrt{(1 - d)(1 - a)(1 - s)}[(1 - a)(1 - d) + (1 - r)d]I \quad (3.7)$$

$$F_{2\text{skip}}^s = (1 - d)(1 - a)I \quad (3.8)$$

$$a = 1 - \frac{F_{2\text{skip}}^s}{F_{2\text{skip}}^q} \quad (3.9)$$

$$r = 1 - \frac{1}{d} \cdot \left[\frac{F_{\text{out}}^s F_{\text{in}}^q}{F_{\text{out}}^q F_{\text{in}}^s} - \frac{F_{2\text{skip}}^s}{F_{2\text{skip}}^q} (1 - d) \right] \quad (3.10)$$

$$s = 1 - \left(\frac{F_{\text{in}}^s}{F_{\text{in}}^q} \right)^2 \frac{F_{2\text{skip}}^q}{F_{2\text{skip}}^s} \quad (3.11)$$

A similar procedure is followed for one-skip waves. The ray path of these waves is illustrated in the bottom panel of Figure 3.1. The main difference of the one-skip waves from the two-skip waves is that the one-skip waves encounter the sunspot in deeper layers and do not have upper turning points located inside the magnetized photosphere, thus they can probe the absorption efficiency of the sunspot at these depths. It is natural to define a new absorption coefficient for the one-skip waves as $a_d = 1 - (F_{1\text{skip}}^s / F_{1\text{skip}}^q)^2$. However, using the same definition for the absorption coefficient as the one used for the two-skip waves allows for a direct comparison of the results obtained with these two methods. The absorption as measured by the one-skip waves is called hereafter “deep absorption” to be distinguished from the “surface absorption” measured by the two-skip waves and defined in Equation (3.9). The “deep absorption” is defined similarly as

$$a_d = 1 - \frac{F_{1\text{skip}}^s}{F_{1\text{skip}}^q} \quad (3.12)$$

The propagation of acoustic waves in the Sun is affected by dispersion. Dispersion increases the width and hence decreases the amplitude of the cross-covariance. However, if dissipation and absorption are ignored, the product of the square of the amplitude and the width of the cross-covariance is constant (Chou and Ladenkov, 2007; Burtseva *et al.*, 2007). In order to correct the effect of dispersion, the width-corrected cross-covariance \tilde{F}_{ab} is defined as

$$\tilde{F}_{ab} = F_{ab}(w_{ab})^{1/2} \quad (3.13)$$

where w_{ab} is the ratio of the width of the cross-covariance at point b to that at point a . All of the cross-covariances presented here are width corrected.

3.3 Data Analysis and Results

Doppler observations from MDI onboard the *Solar and Heliospheric Observatory* (Scherrer *et al.*, 1995) are used in this work. The study of ingoing, outgoing, one- and two-skip waves both for the active regions and the quiet Sun utilizes 31 active region datasets, selected randomly from 1996 to 2001. Each dataset is 512 minutes long, tracked with a Carrington rotation rate and remapped to Postel's coordinates centered at the main active region, with a spatial sampling of $0.12^\circ \text{ pixel}^{-1}$ and a size of 256×256 pixels. Each dataset is then filtered in the Fourier domain to remove solar convection and f modes. We do not filter out signals above the cut-off frequency since most of acoustic power is concentrated below the cut-off limit and our experiments also show that with and without filtering those signals, our results do not change.

The computational procedure starts with the determination of dissipation in the quiet Sun that appears in Equation (3.10). We select 900 pixels from each dataset to compute center-to-annulus cross-covariances with the time-distance helioseismology technique (Duvall *et al.*, 1993; Kosovichev, Duvall, and Scherrer, 2000). Two concentric quadrants are selected around a central pixel so that the radius of the larger quadrant is five times larger than that of the smaller one. The signal inside the quadrants is averaged, and the cross-covariance between the signal of the central pixel and the averaged signal of each quadrant is computed for both positive and negative travel-time lags. Each cross-covariance is then multiplied by the length of the corresponding quadrant because, in the absence of a direction filter, the acoustic energy, propagating from the central pixel to the quadrant, is uniformly distributed over it. The same procedure is repeated for a range of radii of $11 - 45$ pixels and all of the cross-covariances for the same distances and for both time lags, obtained from different central pixels and different datasets, are combined to increase the signal-to-noise ratio. For larger travel distances of $46 - 54$ pixels, the use of five skips is not possible due to the limited size of the dataset and thus only four skips were used. Equation (3.2) is modified for this case to $d(r) = 1 - (F_4/F_1)^{2/3}$. The one- and the five-skip (or four-skip) signals are fitted with a Gabor wavelet function (Kosovichev and Duvall, 1996) and the amplitudes and widths of the two cross-covariances are obtained. The

dissipation is calculated using Equations (3.2) and (3.13) and the result is presented in Figure 3.2.

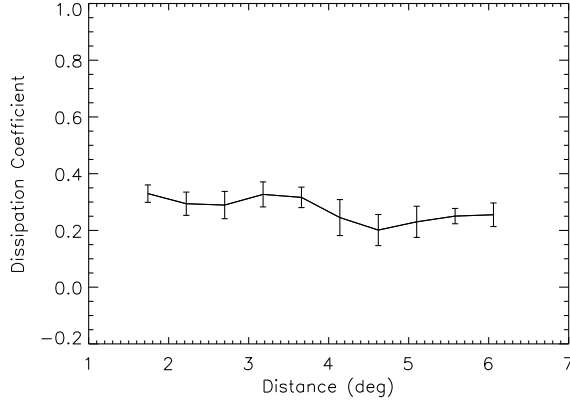


Figure 3.2: Dissipation coefficient in the quiet Sun as a function of acoustic wave-travel distance. Figure adopted from Ilonidis & Zhao (2011).

We should point out that an accurate measurement of dissipation is crucial for the work that follows since the dissipation coefficient appears in Equation (3.10) that is used to determine the emissivity reduction. The approach followed here is based on measurements of an amplitude ratio of five-skip (or four-skip) signals to one-skip signals. In fact any number of skips can be used to determine the dissipation coefficient. Therefore, the ratio of five-skip signal-to-one-skip signal in Equation (3.2) can be a ratio of two skips to one skip or three skips to two skips *etc.* Since after each skip the acoustic energy is reduced by a factor of $(1 - d(r))$, the larger the difference of skips in the ratio of Equation (3.2), the larger the dissipated energy. So using more skips makes our measurements more accurate. The use of more than five-skip signals is not possible due to the limited size of the dataset, so for the dissipation coefficient presented in Figure 3.2, five skips are used for distances up to 5.4° and four skips for larger distances. The two methods, as well as others with different combinations of skips, are consistent with the only difference being that the signal-to-noise ratio is higher for those methods where the dissipated energy is larger.

Next we determine the absorption, emissivity reduction, and local suppression coefficients inside active regions. This study includes 47 active regions distributed in 31 datasets. The strength of the magnetic field in the magnetograms, which were

obtained at the same time with same resolution as the Dopplergrams, is used as the criterion to select the pixels inside the active region in the corresponding Dopplergrams. Setting the threshold at 1100 G and 500 G, we select approximately the pixels inside the umbra and both the umbra and penumbra (sunspot) respectively. Each one of these pixels is used to compute center-to-annulus cross-covariances. An annulus around the central pixel is selected and the signal inside this annulus is averaged. The cross-covariance between the central pixel and the averaged signal inside the annulus is computed for both positive and negative travel-time lags. The positive travel-time lag corresponds to outgoing waves and the negative travel-time lag corresponds to ingoing waves. The same procedure is repeated for a range of radii of 11 – 54 pixels and all of the cross-covariances for the same distances, obtained from different central pixels and different datasets, are combined to increase the signal-to-noise ratio. The signals corresponding to outgoing and ingoing waves are fitted with a Gabor wavelet function and the amplitudes and widths of the two signals are obtained.

For the one- and two-skip waves (see Figure 3.1 for definition of one- and two-skip waves), the annulus around the central pixel is divided into four quadrants and the signal inside each one of them is averaged. The cross-covariance is computed between the two pairs of diametrically opposite quadrants for both positive and negative travel-time lags. The process is repeated again for the same range of radii and all the cross-covariances for the same distances and for both time lags, obtained from different central pixels and different datasets, are combined. The two-skip signal is again fitted with a Gabor wavelet function and the amplitude and width of the signal are obtained. The exactly same procedures are carried out for the quiet Sun to obtain cross-covariances as references. The time–distance diagrams for the sunspot and the quiet Sun as well as the amplitude fittings of the ingoing and outgoing waves are shown in Figure 3.3. The corresponding time–distance diagrams and amplitude fittings for the one- and two-skip waves are shown in Figure 3.4. The three coefficients of absorption, emissivity reduction, and local suppression are computed using Equations (3.9)–(3.11) and the results are presented in Figures 3.5 and 3.6. The error bar corresponds to the standard deviation of those measurements from which mean values are obtained.

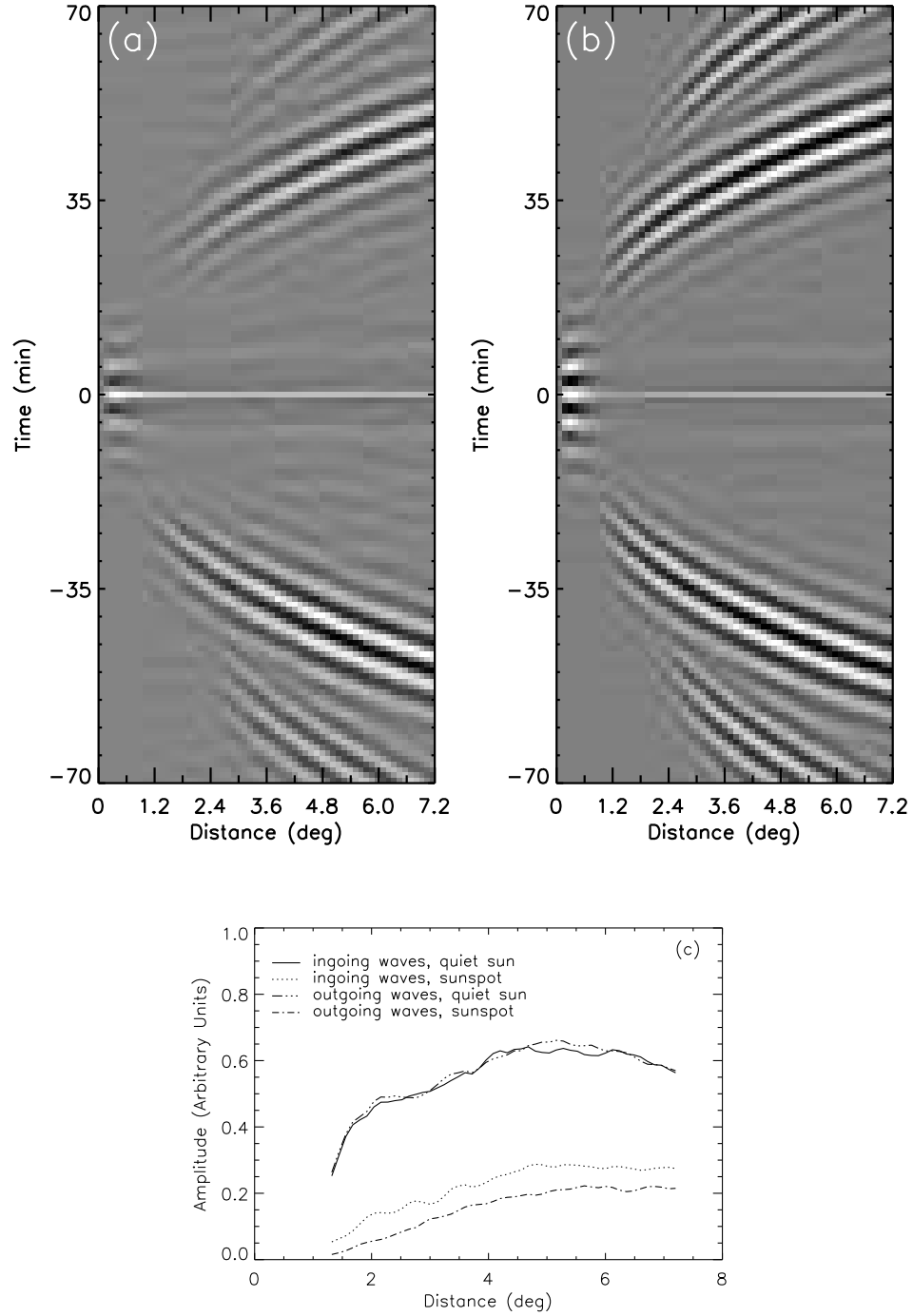


Figure 3.3: Time–distance diagrams of ingoing and outgoing waves for (a) sunspots and (b) quiet Sun. The positive travel–time lag corresponds to outgoing waves and the negative to ingoing waves. The amplitude fittings of the cross-covariance function are shown in panel (c). Figure adopted from Ilonidis & Zhao (2011).

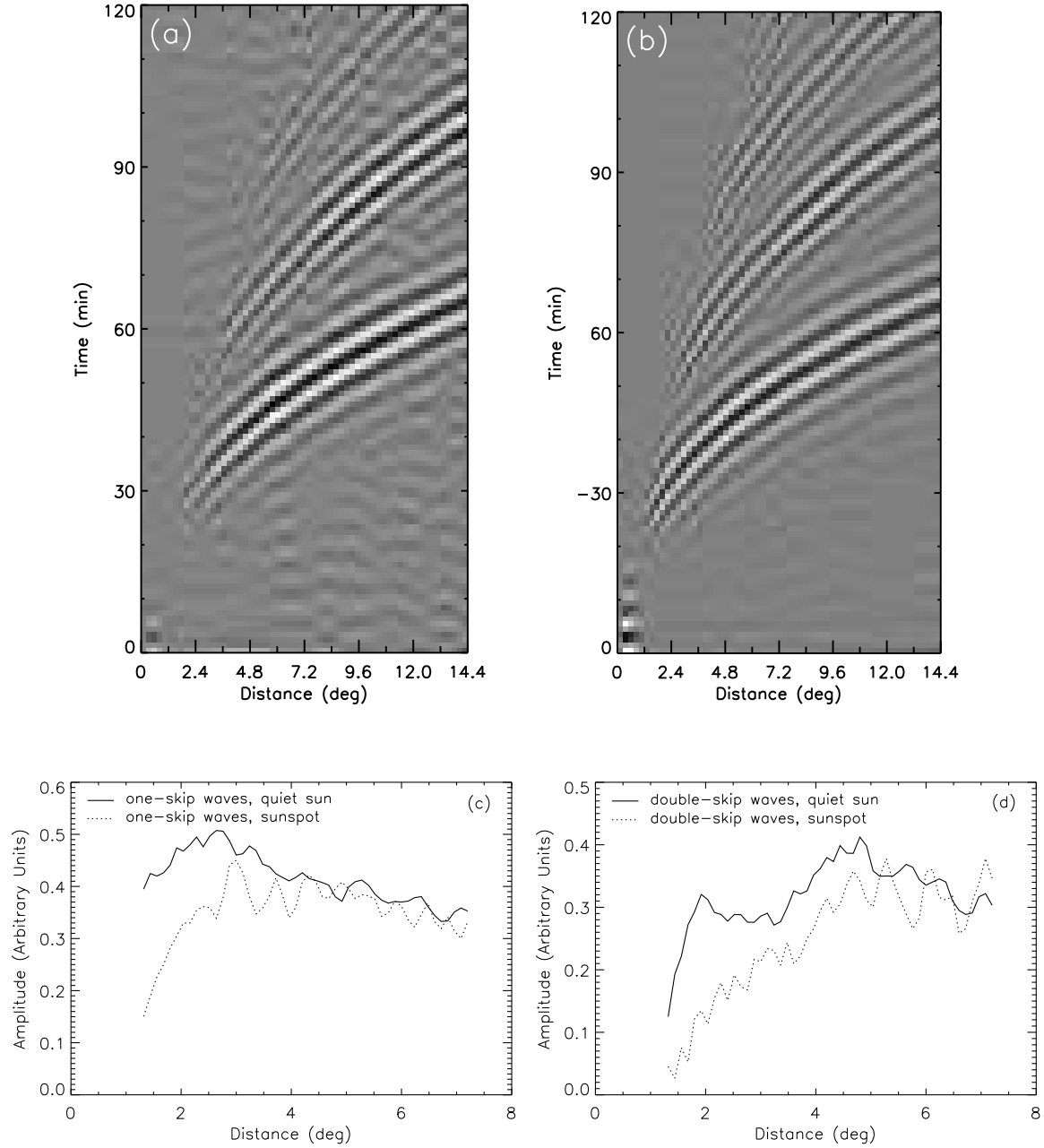


Figure 3.4: Time-distance diagrams of one- and two-skip measurements for (a) sunspots and (b) quiet Sun. Amplitude fitting of the cross-covariance function for (c) one-skip waves and (d) two-skip waves. Figure adopted from Ilonidis & Zhao (2011).

In the model of Figure 3.1, the beginning point is assumed to have the power of the quiet Sun. If that is not the case, an error will arise in the computation of the cross-covariances and the coefficients of absorption, emissivity reduction, and local suppression (Chou *et al.*, 2009d). In order to make our measurements as accurate as possible, the computation of cross-covariances includes only those pixels for which the magnetic field at the beginning point of Figure 3.1 is lower than an arbitrary threshold, which is set to 40 G. For the selection of pixels in the quiet Sun, the closest magnetic region to the quiet pixel is at least nine pixels away from it. The magnetic region is defined as a region where the magnetic field is higher than 500 G. For some large active regions, the annuli of short distances are located completely inside the sunspot and thus no pixel from those annuli can be used for the computation of center-to-annulus cross-covariances. In this case we use the average cross-covariance with same annulus distance from the central pixel, as calculated from all other central pixels of the same dataset. The algorithm described above makes sure that the computation of cross-covariances for the sunspot and the quiet Sun uses the exactly same number of annuli. However, it is possible that at short distances a significant number of pixels in the annuli are excluded from the computation of cross-covariances and therefore the accuracy of the measurements can be affected.

The measurements of ingoing and outgoing waves are less noisy than those of one- and two-skip waves (see Figure 3.1 for definition of one-skip waves). This can be seen either from the time–distance diagrams in Figures 3.3 and 3.4 or from the amplitude fittings of those diagrams. However, in both cases the amplitude and width of the cross-covariance function can easily be obtained by our method. For the quiet Sun, ingoing and outgoing waves have approximately equal amplitudes. On the contrary, for sunspot measurements the amplitude of outgoing waves is reduced compared to that of ingoing waves. The one- and two-skip wave amplitudes show a different trend. At short travel distances, the wave amplitude in the quiet Sun is much greater than that in sunspot but at large travel distances the two amplitudes are comparable within the noise level of the measurements.

The surface absorption coefficient, presented in Figures 3.5a and 3.6a, is a maximum at the shortest travel distances and smoothly drops to zero at distance of about

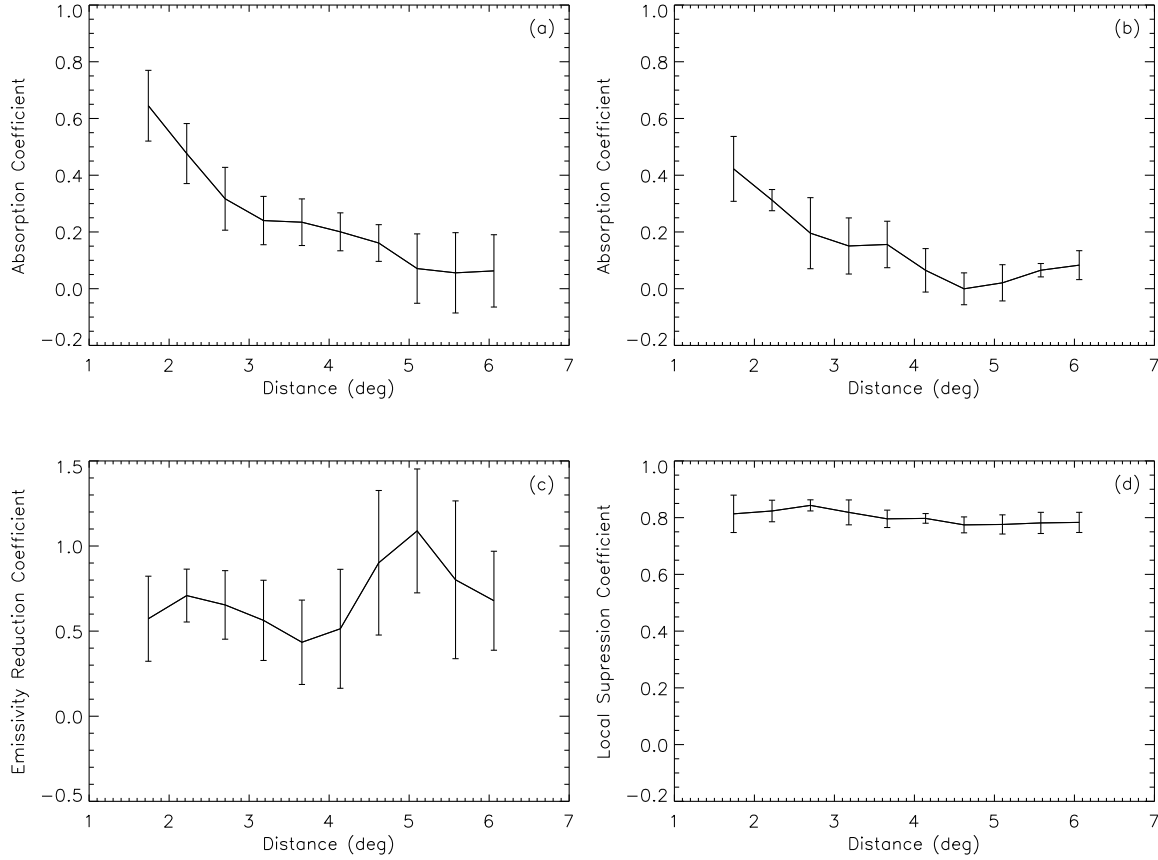


Figure 3.5: Coefficients of (a) surface absorption, (b) deep absorption, (c) emissivity reduction, and (d) local suppression obtained from umbral measurements (threshold of 1100 G). Figure adopted from Ilonidis & Zhao (2011).

6°. This picture is consistent with previous work (for example Braun, Duvall, and LaBonte, 1987, 1988; Bogdan *et al.*, 1993; Chen *et al.*, 1996). However, a quantitative comparison is not possible, first due to the different definitions of absorption and second because our definition separates the effects of absorption and emissivity reduction. The deep absorption follows the same trend but compared to the surface absorption is about 40% smaller at small travel distances where both of them are greater than zero. At large travel distances they both drop to zero and become comparable. The emissivity reduction coefficient is most noisy due to the several terms involved in Equation (3.10). Inside umbrae emissivity reduction is rather high ranging from 0.44 to 1.00 with a mean value of 0.70, while in the whole sunspot the

corresponding range is 0.29 to 0.72 averaging 0.47. The local suppression coefficient is very constant within the range of travel distances used in this work. Its mean values for umbral and penumbral measurements are 0.80 and 0.665 respectively.

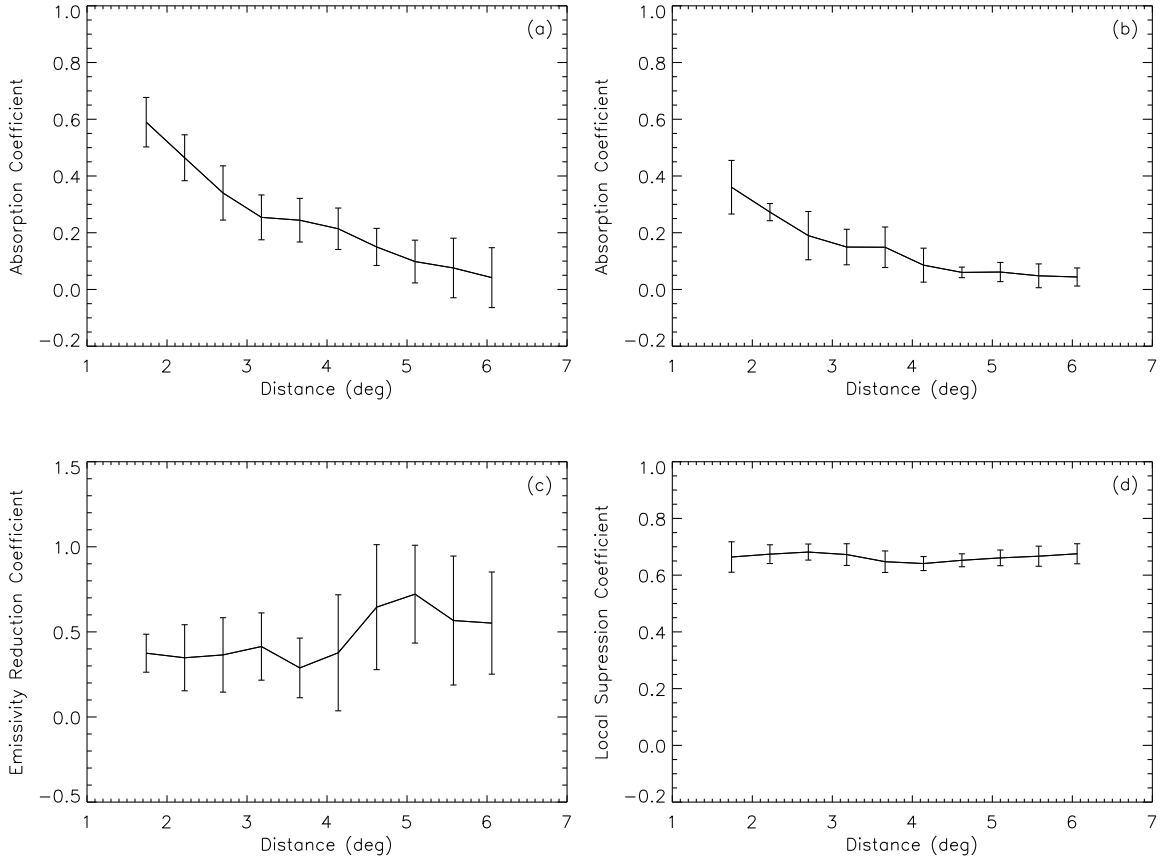


Figure 3.6: Coefficients of (a) surface absorption, (b) deep absorption, (c) emissivity reduction, and (d) local suppression obtained from sunspot measurements (threshold of 500 G). Figure adopted from Ilonidis & Zhao (2011).

All three coefficients of absorption, emissivity reduction, and local suppression, as defined in this work, contribute to the power deficit inside sunspots. However, it is not clear, from this definition, what is the exact contribution of each coefficient to the total power deficit in sunspots. It is more appropriate to define three normalized coefficients so that each is equal to the fraction of the contribution of the corresponding mechanism to the total power deficit inside the sunspot. Following Chou et al.

(2009c), the normalized coefficients are

$$a_* = \frac{a(1-d)}{1-P} \quad (3.14)$$

$$r_* = \frac{rd}{1-P} \quad (3.15)$$

$$s_* = \frac{s[(1-a)(1-d) + (1-r)d]}{1-P} \quad (3.16)$$

where $P = (1-s)(1-a)(1-d) + (1-s)(1-r)d$ is the total acoustic power inside the sunspot. It is easily shown that $a_* + r_* + s_* = 1$. The normalized coefficients are plotted as functions of travel distance in Figure 3.7.

The definition of normalized coefficients allows a direct comparison of the results obtained in this work with results from previous works. Chou *et al.* (2009c), using the same definition, found that the fractional contribution of each mechanism to the acoustic power deficit in the umbra of the sunspot for a specific wave packet that corresponds to travel distance of 3.5° is $a = 0.233$, $s = 0.685$ and $r = 0.082$. For the same travel distance, we found $a = 0.187$, $s = 0.652$ and $r = 0.161$. The two methods are consistent in local suppression but not in absorption and emissivity reduction. The absorption in Chou *et al.* is larger compared to our work while the emissivity reduction is smaller. However, the results obtained in this work are based on averaged measurements over 46 sunspots while the results presented by Chou *et al.* are based on a single sunspot. Not only are the two samples different but it is also possible that there are significant variations among the 47 sunspots analyzed in this study. Especially the coefficients of absorption and emissivity reduction may have strong dependence on the size of the sunspot and the strength of the magnetic field. It would be interesting to use the sample of 47 sunspots to study this dependence. Our method does not make use of phase-speed and direction filters though, and consequently, time-distance measurements with individual sunspots are very hard, if not impossible. In practice, the low number of total pixels increases the noise level in the cross-covariance function for the one- and especially for the two-skip waves, making the measurement of the amplitude very hard.

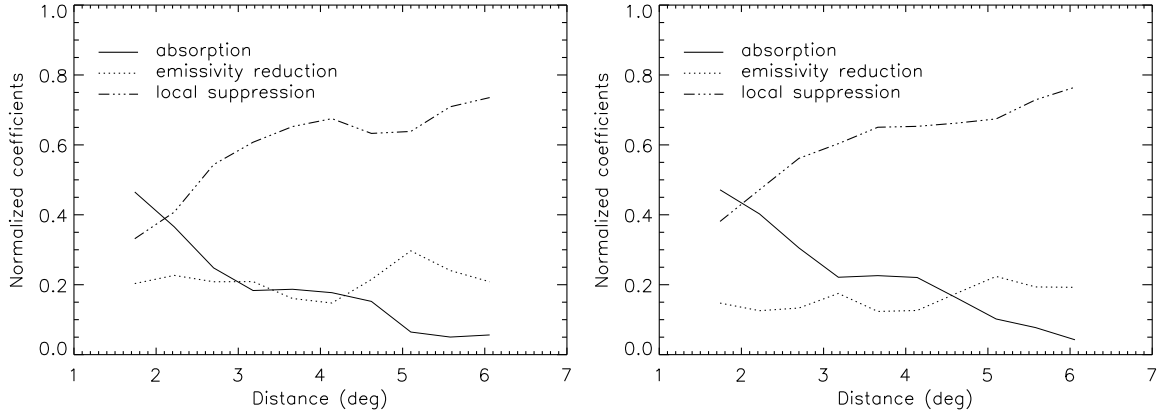


Figure 3.7: Normalized coefficients as functions of the travel distance for the umbral measurements (left) and the sunspot measurements (right). Figure adopted from Ilonidis & Zhao (2011).

3.4 Summary

We apply a new method to measure the coefficients of absorption, emissivity reduction, and local suppression inside solar active regions as well as the coefficient of dissipation in the quiet Sun. This method utilizes measurements from many active regions to increase the signal-to-noise ratio, and does not use signal filters except filtering out solar convection and f -modes. All four coefficients are determined as functions of the travel distance. Comparison with previous work for a specific travel distance shows good agreement in the coefficient of local suppression but discrepancies in coefficients of absorption and emissivity reduction. It is not clear though if these discrepancies are caused by the different method used in each case or by the different samples of sunspots. In summary, our results show the following:

- i The absorption coefficient is the dominant mechanism for the power deficit in sunspots at short distances but it gradually drops to zero at travel distance of about 6° .
- ii The measured deep absorption is about 60% as high as the measured surface absorption indicating that sunspots can actually absorb a large amount of acoustic

energy not only close to the surface but also deep below the photosphere.

- iii The emissivity reduction coefficient ranges between 0.44 and 1.00 within the umbra with a mean value of 0.70, and between 0.29 and 0.72 within the sunspot with a mean value of 0.47. The fractional contribution to the acoustic power deficit in sunspots is 21.5% for the umbra and 16.5% for the sunspot.
- iv The local suppression coefficient is remarkably constant as a function of the travel distance with a value of 0.80 for the umbral measurements and 0.665 for the sunspot measurements. Its fractional contribution to the acoustic power deficit increases smoothly as a function of the travel distance from 33% to 75% in the umbra and from 38% to 79% in the sunspot.

Chapter 4

Emerging Magnetic Flux I: Method¹

4.1 Introduction

Understanding solar magnetism is among the most important problems of solar physics. The emergence of magnetic flux from the deep solar interior to the atmosphere is related to the depth of a dynamo (Brandenburg, 2005), the formation and evolution of sunspots (Solanki, 2003; Rempel & Schlichenmaier, 2011), the initiation of flares and coronal mass ejections (Chen & Shibata, 2000), and the 11-year activity cycle (Hathaway, 2010). The detection of emerging magnetic flux in the deep convection zone may improve our understanding of solar magnetism.

It is widely believed that magnetic fields are generated and stored in the tachocline, a thin shear layer at the bottom of the convection zone. These fields are amplified by a dynamo action and rise in the form of Ω -shaped flux tubes through the convection zone to the surface where they are observed as active regions (Figure 4.1). However, there is no convincing observational evidence to support this idea, and dynamo mechanisms operating in the bulk of the convection zone or even in the near-surface

¹Part of this chapter was published in Science (Ilonidis, Zhao, & Kosovichev, 2011, 2012b) and the proceedings of the 61st Fujihara seminar: progress in solar/stellar physics with helio- and asteroseismology (Ilonidis, Zhao, & Kosovichev, 2012a)

shear layer have been proposed as well (Brandenburg, 2005). Investigation of emerging magnetic flux could possibly determine the depth of this process and set the foundations for a better understanding of sunspots and active regions.

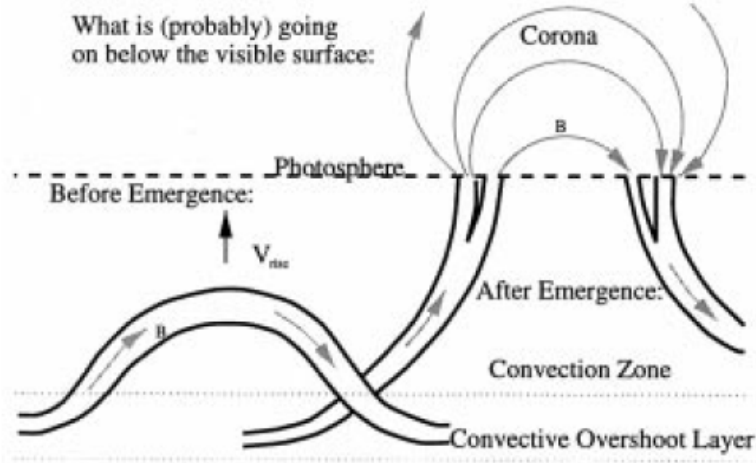


Figure 4.1: Cartoon representation of the most likely sub-photospheric magnetic structure of an emerging active region. Figure adopted from Fisher et al. (2000).

Early detection of emerging magnetic flux would also improve space weather forecasts. Active regions on the Sun produce flares and mass eruptions that may arrive on the Earth and cause power outages, satellite failures, and interruptions of telecommunication and navigation services. These eruptive events also pose a threat to astronauts and spacecraft. It is important for space weather forecasts to monitor solar subsurface processes and predict the emergence of active regions as well as the eruptive events associated with them. Emerging-flux events last typically from a few hours up to several days and, therefore, the goal is not only to make predictions about the emergence of new active regions, but also to predict the temporal evolution of those regions.

Numerical simulations have provided important physical insight into the process of magnetic flux emergence even though it is not possible yet to perform 3D MHD simulations of emerging flux tubes from the bottom of the convection zone to the solar atmosphere. Three-dimensional spherical shell anelastic MHD simulations of

rising magnetic flux tubes from the base of the convection zone up to a depth of 16 Mm have been carried out by Fan (2008). It was found in these simulations that in order for the emerging flux tube to show a tilt consistent with Joy's law, the flux tube should undergo severe flux loss during its rise. Birch, Braun, & Fan (2010) used this simulation model to estimate the detectability of rising flux tubes by helioseismology. It was suggested that the dominant effect of the rising flux tubes on the wave propagation is expected to be from a 100 m/s retrograde flow associated with the rising flux. MHD simulations in the top few Mm of the strongly stratified convection zone and the overlying convectively stable photospheric layer have recently revealed a number of important features: the lateral expansion of the flux tube into a magnetic sheet (Cheung, 2008), the dynamic coupling of convective flows and magnetic field (Fang et al., 2010, 2012), the role of convection and initial field strength to the dynamic evolution of the flux tube (Weber, Fan, & Miesch, 2011), and the flux deceleration, horizontal expansion, and two-step emergence into the atmosphere (Toriumi & Yokoyama 2010, 2011). For a review of numerical flux emergence models see Fan (2009).

Observations show that new emerging flux is characterized by significant fragmentation with strong flux concentrations distributed at small unresolved spatial scales. The formation of an active region in the photosphere is first observed with the appearance of small magnetic dipoles with opposite polarity that move apart at large speeds. New flux emerges between the two polarities with the newly emerged magnetic structures separating and reaching the main polarities. During this phase which lasts typically 3-5 days, the formation of pores and larger spots is observed by the coalescence of smaller magnetic elements.

Several studies have been performed on the helioseismic detection of emerging flux and these studies search mainly for wave-speed perturbations and plasma flows. Chang, Chou, & Sun (1999) constructed phase-shift maps of AR 7978 using the method of acoustic imaging (Chang et al., 1997). They reported the detection of upward-moving magnetic flux during the development of the active region. However, the contribution of the surface magnetism effects to the measured phase shifts was quite large. Kosovichev, Duvall, & Scherrer (2000) studied, using the time-distance technique (Duvall et al., 1993), the emergence of an active region which appeared on

the solar disc in January 1998. The authors found that the emerging flux propagates very quickly in the uppermost 18 Mm of the convection zone with the emerging speed estimated at about 1.3 km/s. Their results also suggest that sunspots are formed as a result of the concentration of magnetic flux close to the surface. Jensen et al. (2001) analyzed the same active region and found that wave-speed perturbations extend at least 20 Mm below the surface. They also report deeper anomalies that appeared 16–20 hours after the emergence and disappeared within 8 hours suggesting a change in the subsurface structure of the active region.

More recently, Kosovichev & Duvall (2008) investigated the emergence of AR 10488 which was observed with SOHO/MDI in October 2003 (Figure 4.2). The authors suggest that the active region is formed as a result of multiple flux emergence events. They also found that the emergence is accompanied by strong shearing outflows. However, no significant pre-emergence signatures were detected. Zharkov & Thompson (2008) investigated the emergence of AR 10790 using the same time-distance approach as Kosovichev et al. (2000). They observed regions with sound speed perturbations, presumably related to subsurface emerging flux, and estimated the speed of emerging flux at about 1 km/s. In all these studies, the low S/N ratio of the helioseismic measurements in the deeper layers and possibly the fast emergence speed posed constraints on a definitive subsurface detection before the flux appeared in the photosphere. For a recent review on the photospheric and subphotospheric studies of emerging magnetic flux see Kosovichev (2009).

A statistical study of a large number of active and quiet regions (Komm, Howe, & Hill, 2009), with ring-diagram analysis (Hill, 1988), showed that average vertical flows are shifted toward upflows in emerging-flux regions and downflows in decaying-flux regions. For flux emergence, upflows become stronger at depths greater than about 10 Mm whereas for decaying flux the flows change from upflows to downflows at depths greater than 10 Mm. Except for local helioseismic techniques, other methods have been employed as well for the detection of pre-emergence signatures of magnetic flux. Hartlep et al. (2011) found, using numerical simulations and observations, that under certain conditions subsurface emerging magnetic structures could cause detectable acoustic power variation in the overlying photospheric layer. The power variation

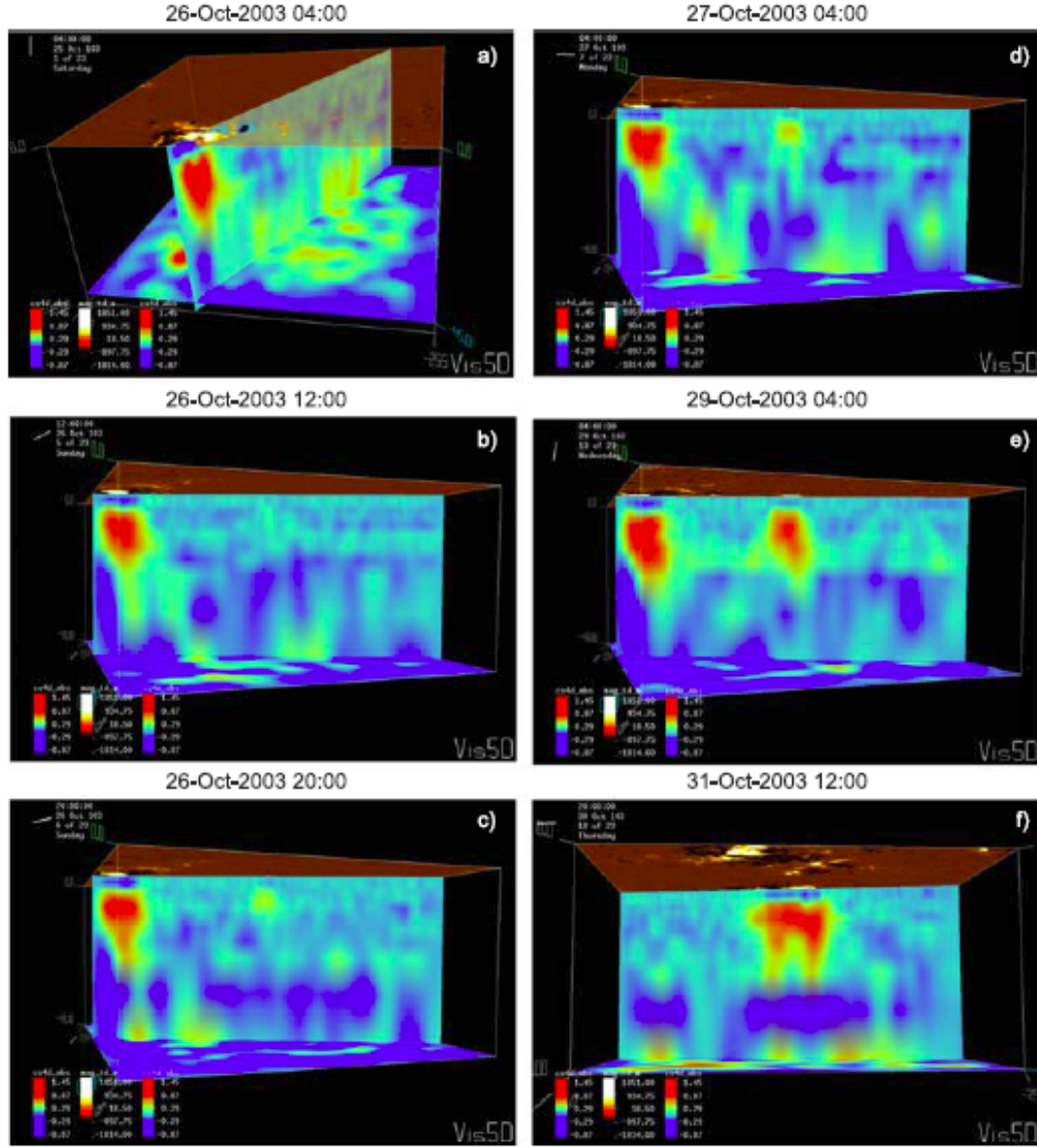


Figure 4.2: Subsurface wave-speed perturbations of AR 10486 (on the left-hand side of the images), and emerging-flux region 10488 (in the middle). Red color shows positive wave-speed variations relative to the quiet Sun; the blue color shows the negative variations, which are concentrated near the surface. The upper semi-transparent panels show the corresponding MDI magnetograms; the lower panel is a horizontal cut 48 Mm deep. The vertical cut goes through both active regions, approximately in the North–South direction crossing the equator, except the image in the right bottom panel, (f), where it goes only through AR 10488 in the EastWest direction. Figure adopted from Kosovichev (2009).

was found to be strongest for frequencies between 2 – 4 mHz for simulation data and 3 – 4 mHz for AR 10488 observed with SOHO/MDI. In another study, Toriumi, Hayashi, & Yokoyama (2012) detected a horizontal divergent flow of 0.6 – 2.3 km/s at the location of an active region emergence about 100 minutes before the start of emergence in the photosphere.

4.2 Data and Filtering

Doppler and magnetic field observations from Michelson Doppler Imager (Scherrer et al., 1995) onboard the *Solar and Heliospheric Observatory* (SOHO) are used in this work. The datasets are tracked with a Carrington rotation rate and remapped using Postel’s projection. The Doppler datacubes have a spatial resolution of $0.12^\circ \text{ pixel}^{-1}$, a temporal cadence of 1 minute, and a horizontal size of 256×256 pixels corresponding to an area of about $30^\circ \times 30^\circ$. Each dataset is then filtered in Fourier domain with a phase-speed filter and a frequency filter to select the oscillation signals with phase-speeds of 92 to 127 km/s and frequencies of 2 to 5 mHz (Figure 4.3). The filtered acoustic waves have one-skip horizontal distances of 111 to 198 Mm corresponding to lower turning points of 42 to 75 Mm respectively (Figure 4.4).

We have also used data from Helioseismic and Magnetic Imager (Schou et al., 2012) onboard the recently launched *Solar Dynamics Observatory* (SDO) as well as from the Global Oscillation Network Group (GONG) (Harvey et al., 1996). The HMI and GONG datasets are tracked with the same rate and spatial resolution as the MDI datasets. The temporal cadence for HMI is 45 s and for GONG is 1 minute. The filtering procedure is exactly the same for all of them.

4.3 Method

Our method is essentially based on deep-focus time-distance helioseismology technique (Duvall et al., 1993; Duvall, 2003). The measurement procedure has been modified to increase the S/N ratio in travel-time maps. The modifications are done at four separate stages of the measurement procedure: phase-speed filtering, averaging

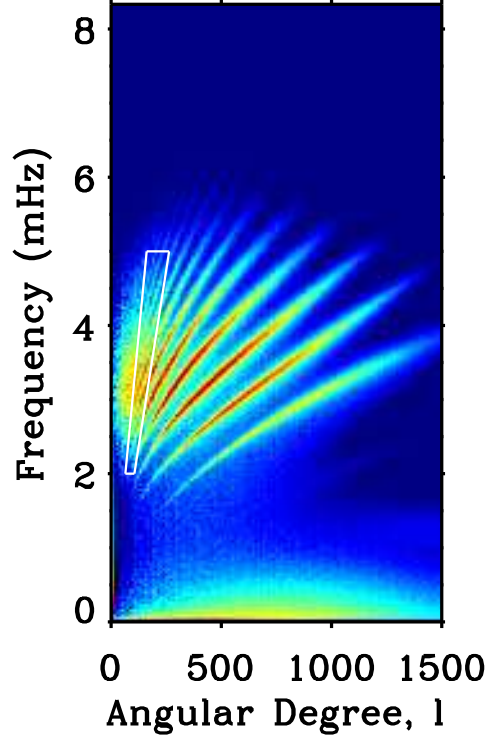


Figure 4.3: Power spectrum of solar oscillations computed from a 480-minute MDI dataset. The white quadrangle delimits the frequency range of 2 to 5 mHz and phase-speed range of 92 to 127 km/s used for the detection of emerging magnetic flux.

of the oscillation signal over an arc, use of multiple arc configurations, and selection of annuli. Helioseismic measurements at quiet and emerging-flux regions show that at each step the S/N ratio is significantly increased (Figure 4.5). In this study, cross-covariance functions are always fitted with Gabor wavelet functions (Kosovichev & Duvall, 1997) and travel-time maps show perturbations of the mean phase travel-time.

4.3.1 Phase-speed filtering

The first modification is related to the phase-speed filtering. The use of phase-speed filter can significantly increase the S/N ratio and phase-speed filters have been widely used to detect acoustic perturbations and flows in the solar interior (Duvall et al.,

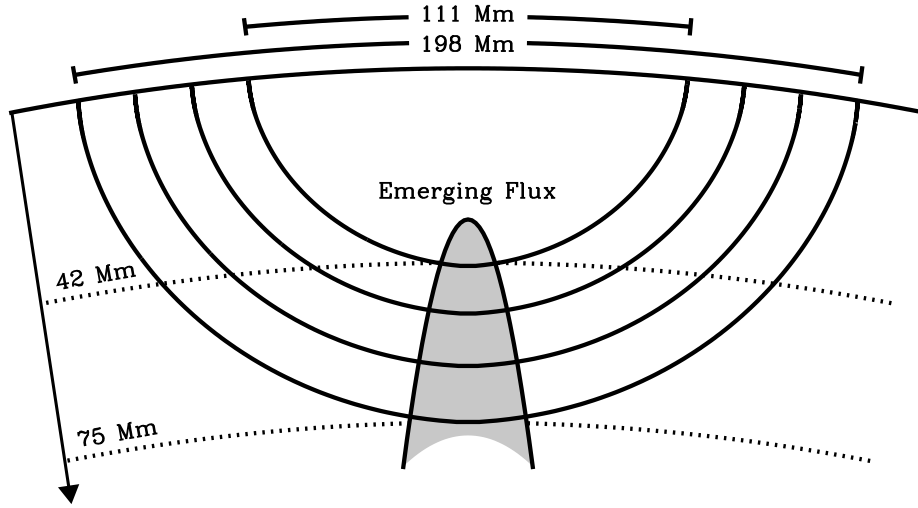


Figure 4.4: Acoustic ray paths with lower turning points between 42 and 75 Mm crossing a region of emerging flux. For simplicity only 4 out of a total of 31 ray paths, used in this study, are shown here. Figure adopted from Ilonidis, Zhao, & Kosovichev (2011).

1997). These filters select acoustic waves with similar phase speeds. The selected waves have approximately the same penetration depth into the convection zone and can be used to investigate properties of flux emergence at specific depths. In local helioseismology, phase-speed filters are typically of Gaussian shape with a narrow width that is chosen empirically. However, the choice of the shape and width of the phase-speed filter can affect both the signal level (travel-time shift caused by an emerging flux event) and the noise level (travel-time shifts measured in quiet-Sun regions). Figure 4.6 shows an example of two phase-speed filters with the same central phase speed that are tested in the same emerging-flux and quiet-Sun regions. The filter with the lower noise level, estimated by the quiet-Sun measurements, does not have a higher S/N ratio because of the significant reduction on the signal level. This simple example demonstrates the importance of the optimal phase-speed filter selection. Gaussian phase-speed filters that minimize the noise level and have been widely used in helioseismology may not necessarily maximize the S/N ratio. Here, we use a new filter which selects all the acoustic waves with phase speed between 92 and 127 km/s and drops, outside of this range, as a Gaussian function with width

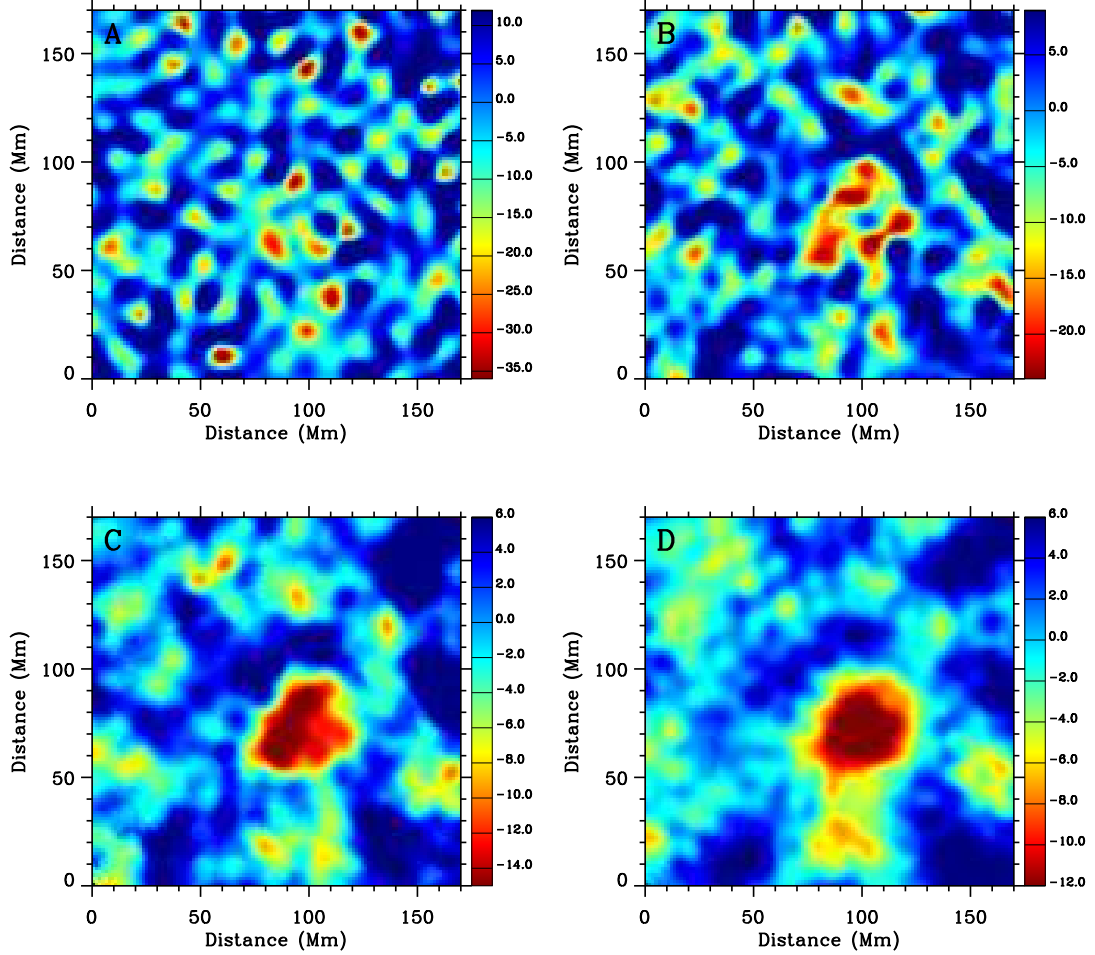


Figure 4.5: Step-by-step improvement of the S/N ratio in the mean travel-time perturbation maps. Each panel introduces one or more modifications to the previous deep-focus time-distance measurement scheme: (A) The previous method: point-to-point computation of cross-covariance function with a Gaussian phase-speed filter with width (standard deviation) of 12.3 km/s using 9 focus depths between 54 and 62 Mm. The S/N ratio is rather low. (B) Same as in panel A but with 2 modifications: the map was computed using the new filter and 31 focus depths between 42 and 75 Mm. The S/N ratio is 3.2. (C) Same as in panel B but with one additional modification: the cross-covariances are computed after averaging the oscillation signal over arcs with a size of 25.7° . The S/N ratio is 3.9. (D) Same as in panel C but with one additional modification: the cross-covariances are computed using the 20 arc configurations described in the text. The S/N ratio is 4.9.

(standard deviation) of 8.7 km/s. The S/N ratio of this phase-speed filter is higher than other Gaussian phase-speed filters with the same central phase-speed (Figure 4.7).

4.3.2 Averaging of the Oscillation Signal

The measurement scheme used for the computation of cross-covariances has been also modified. In previous studies, an annulus is selected at the solar surface and point-to-point cross-covariances are computed for every pair of diametrically opposite points on the annulus both for positive and negative time lags. These cross-covariances are then averaged and the two lags are combined to increase the S/N ratio. This measurement scheme is known as deep-focus since the acoustic ray paths that connect diametrically opposite points on an annulus are all focused on a single point below the center of the annulus. A modified version of this deep-focus geometry was used in the previous chapter to measure the coefficients of absorption, emissivity reduction, and local suppression inside sunspot regions. In that approach, the oscillation signal was first averaged over a quadrant and cross-covariances of averaged oscillation signals of diametrically opposite quadrants were computed and averaged. In general, spatial averaging (typically over an arc) of the oscillation signal before the computation of cross-covariances can increase the S/N ratio of travel-time maps (Figure 4.8). On the other hand, the spatial averaging may limit to some extent the resolving capability of small-scale structures but this is not a big concern for large horizontal wavelengths and travel-time signatures larger than several tens of Mm.

4.3.3 Multiple Arc Configurations

Spatial averaging of the oscillation signal over an arc allows the use of multiple arc configurations. Here we select arcs of 5 different sizes, 25.7°, 30°, 36°, 45° and 60° and 4 different orientations (Figure 4.9). The orientations are chosen such that starting from an arbitrarily oriented configuration with an arc size of N degrees, every other configuration with the same number of arcs can be produced from the previous one by a rotation of $N/4$ degrees. The combinations of 5 arc sizes and 4 orientations

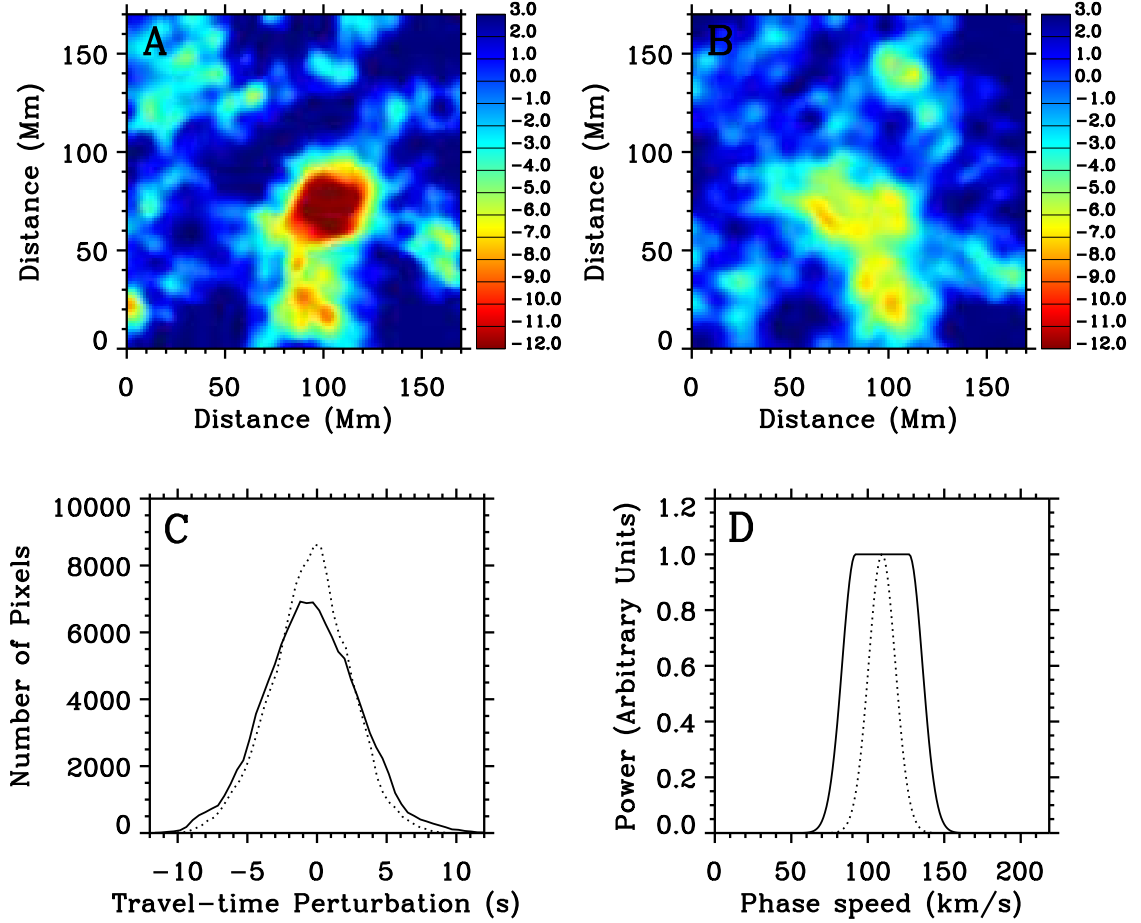


Figure 4.6: (A) Mean travel-time perturbation map (in seconds) of AR10488 at a depth of 42-75 Mm obtained from an 8-hour dataset centered at 03:30 UT, 26 October 2003. The map was computed using the phase-speed filter shown in panel D with solid line and arcs with a size of 45° and 4 different orientations. The maximum phase travel-time shift is 16.2 s. (B) Same as panel A except that the map was computed using the Gaussian phase-speed filter shown in panel D with dotted line. The maximum travel-time shift is 7.4 s. (C) Distribution of the travel-time shifts measured in 9 quiet-Sun regions using exactly the same procedure as in panel A (solid line) and exactly the same procedure as in panel B (dotted line). The standard deviations of these measurements is 3.4 s and 2.9 s which yield S/N ratios of 4.8 and 2.6 for the signature detected in panels A and B respectively. (D) The two phase-speed filters used for computation of the travel-time maps in panels A and B.

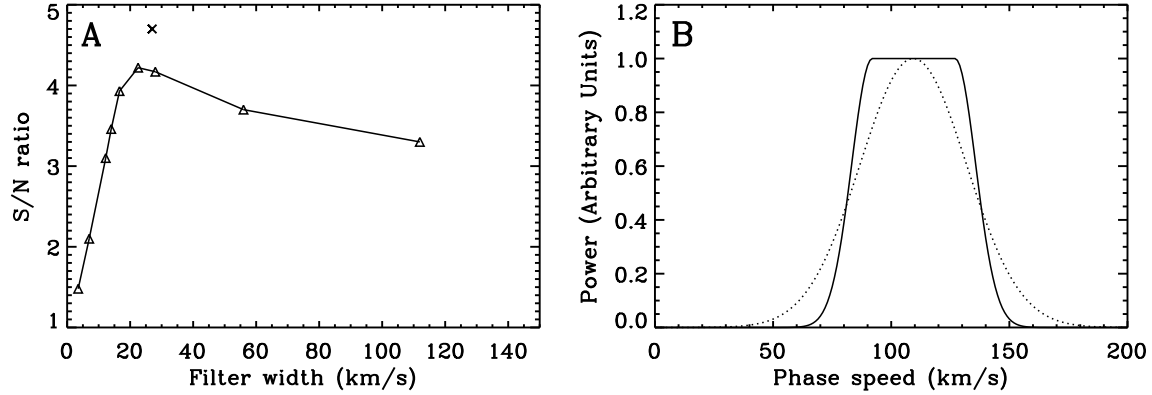


Figure 4.7: Panel A shows the S/N ratio as a function of the width (standard deviation) of a Gaussian phase-speed filter. The S/N ratios were estimated by analyzing emerging-flux and quiet-Sun regions, as shown in Figure 4.6, using the method described there. The cross sign (\times) indicates the S/N ratio of the optimized filter shown in panel B with solid line which was used for the detection of emerging sunspot regions. This filter has higher S/N ratio than any Gaussian phase-speed filter with the same central phase-speed. The dotted line in panel B shows the Gaussian filter which yields the highest S/N ratio among the Gaussian filters of panel A. Figure adopted from Ilonidis, Zhao, & Kosovichev (2012a).

produce 20 arc configurations that are used for the computation of cross-covariances. Cross-covariances obtained from configurations with the same number of arcs have same phase and therefore can be added together to increase the S/N ratio. The acoustic travel-time has a weak dependence on the arc size (it is shorter for larger arc sizes and longer for smaller arc sizes) and therefore cross-covariances obtained from arc configurations with different number of arcs are not combined. These cross-covariances are fitted separately with a Gabor wavelet (Kosovichev & Duvall, 1997) and the phase travel-time maps are averaged to increase the S/N ratio. Figure 4.10 shows travel-time maps of AR 10488 made with the 20 arc configurations. A strong travel-time anomaly caused by the emerging flux can be identified in all of them even though there are variations in the size and the strength of the detected anomaly. With an appropriate combination of cross-covariances and travel-time maps, a higher S/N ratio can be achieved as it is shown in 4.5.

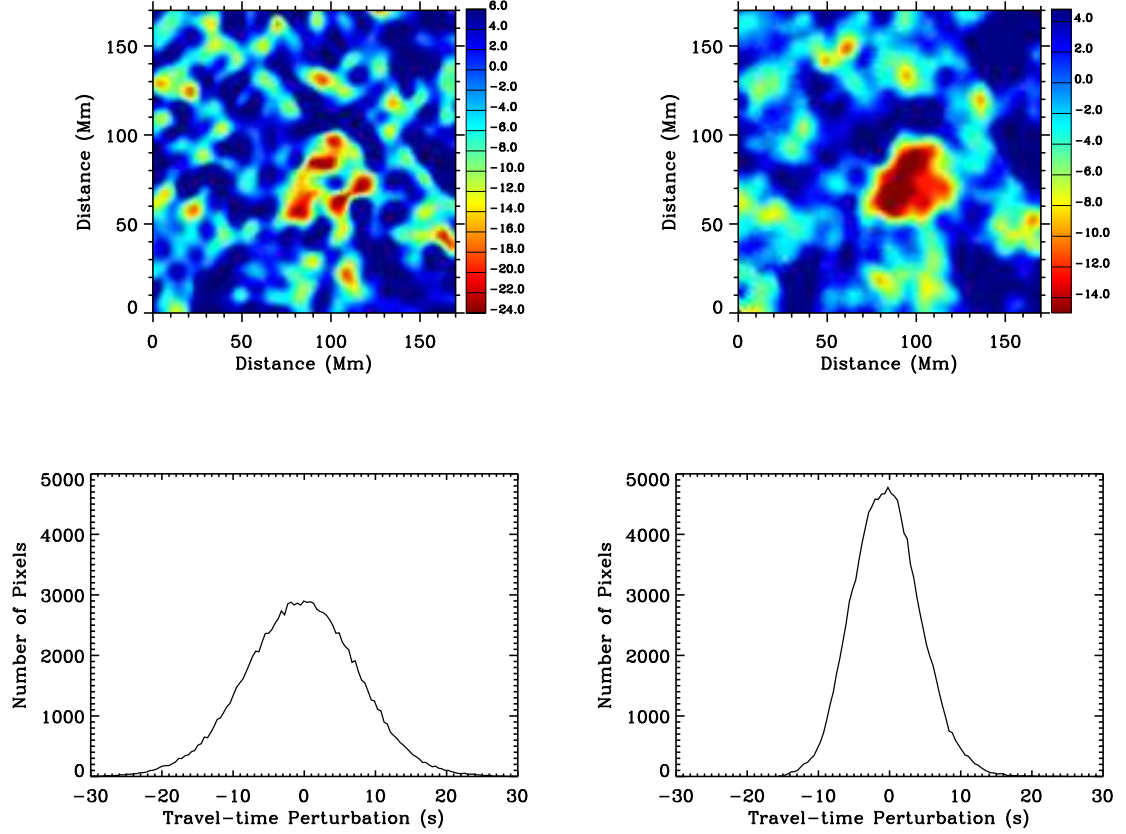


Figure 4.8: Comparison of point-to-point with arc-to-arc computation of cross-covariances. Upper left: Mean travel-time perturbation map (in seconds) of AR10488 at a depth of 42-75 Mm obtained from an 8-hour dataset centered at 03:30 UT, 26 October 2003. The map was computed using the phase-speed filter shown in Figure 4.7 with solid line and point-to-point computation of cross-covariances. The maximum phase travel-time shift is 25.5 s. Upper right: Same as left panel except that the map was computed using arc-to-arc computation of cross covariances with an arc size of 25.7° and random arc orientation. The maximum phase travel-time shift is 18.9 s. Lower left: Distribution of travel-time shifts measured in 9 quiet-Sun regions using exactly the same measurement procedure as in top left panel. The standard deviation of these measurements is 7.9 s which yields a S/N ratio of 3.2 for the signature detected in top left panel. Lower right: Distribution of travel-time shifts measured in 9 quiet-Sun regions using exactly the same measurement procedure as in top right panel. The standard deviation of these measurements is 4.8 s which yields a S/N ratio of 3.9 for the signature detected in top right panel.

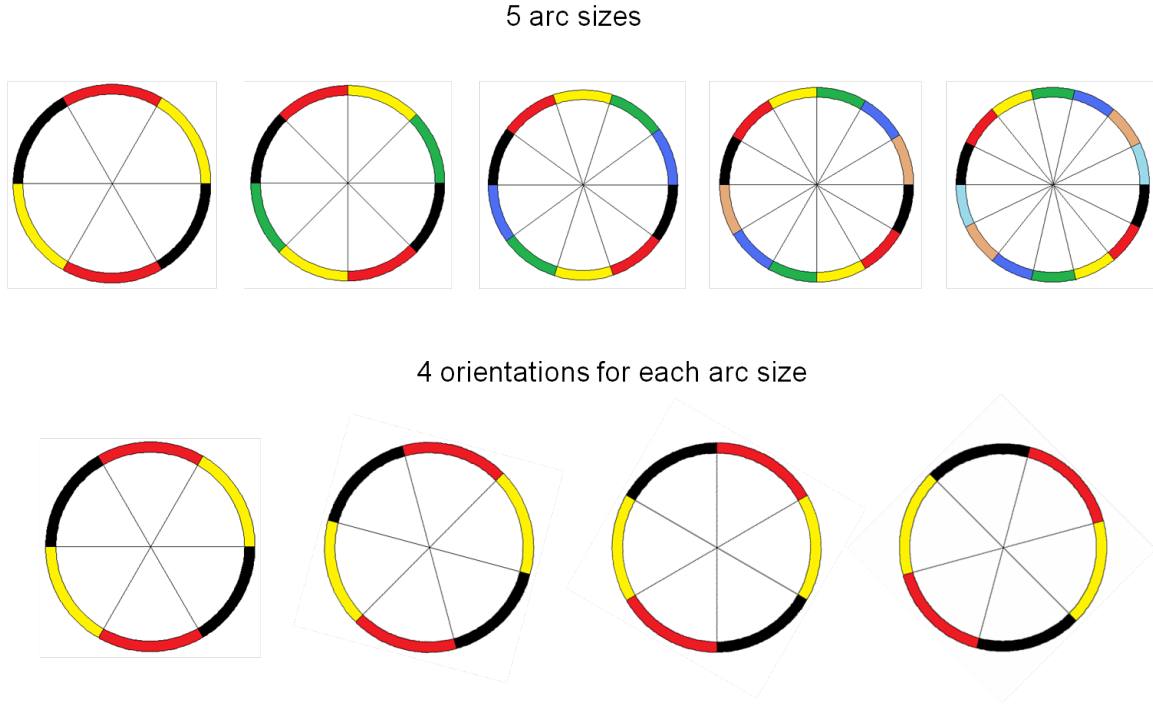


Figure 4.9: Schematic representation of the 20 arc configurations used for the computation of cross-covariances. The arcs have five different sizes and for each arc size, four orientations are selected. The selection of the orientations is described in the text. For simplicity only the four orientations corresponding to arcs with size of 60 degrees are shown here. The oscillation signal is averaged inside each arc, and cross-covariances are computed between arcs of the same color.

4.3.4 Depth Averaging

The selection of a large number of annuli, under certain conditions that are explained below, can also improve the S/N ratio. Here we use 31 annuli with diameters between 111 and 198 Mm and compute cross-covariances for the corresponding travel distances. As it was mentioned above, the acoustic ray paths of each annulus are focused on one point deep below the center of the annulus and therefore the 31 annuli correspond to 31 focus depths between 42 and 75 Mm. If the emerging flux causes a detectable effect on the measured cross-covariance at all these depths, then adding more cross-covariances from different depths will increase the S/N ratio. If on the other hand the effect of the emerging flux on the cross-covariance function is limited to a narrow range

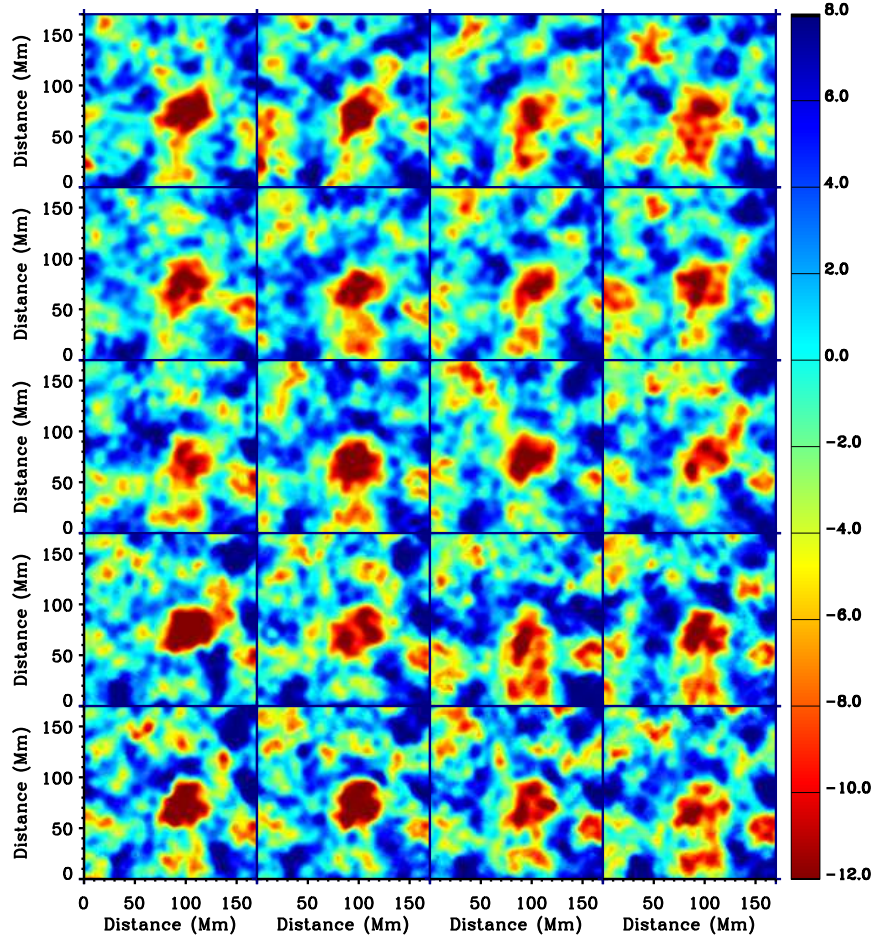


Figure 4.10: Phase travel-time perturbation maps of AR 10488 made using the 20 arc configurations described in the text. The maps were computed using the phase-speed filter shown in Figure 4.7 with solid line. Rows correspond to configurations with the same number of arcs and columns correspond to configurations with the same orientation. The number of arcs from top to bottom is 6, 8, 10, 12, and 14. The orientations are chosen such that starting from an arbitrarily oriented configuration with an arc size of N degrees, every other configuration with the same number of arcs can be produced from the previous one by a rotation of $N/4$ degrees. Each map shows a strong travel-time anomaly at the location of emergence. An appropriate combination of cross-covariances and travel-time maps, as it is described in the text, increases the S/N ratio of the final map shown in panel D of Figure 4.5.

of depths, then adding more cross-covariances outside of this depth range will reduce the S/N ratio. We found from our measurements that averaging cross-covariances from about 30 focus depths, maximizes the S/N ratio. Figure 4.11 shows travel-time maps of AR 10488 made using 11 focus depths that cover (from left to right) the depth ranges of 64 – 75, 53 – 64, and 42 – 53 Mm. The strong travel-time signatures at the center of the maps, which are caused by the emerging magnetic flux, have typical size of about 30 Mm. A combination of all the cross-covariances obtained from focus depths between 42 and 75 Mm can increase the size of the travel-time signature to about 50 Mm as it is shown in panel D of Figure 4.5. The S/N ratio is also expected to increase, since random travel-time perturbations at individual focus depths may cancel after combining measurements from many focus depths, while on the other hand the travel-time anomalies which are consistently detected at all focus depths are enhanced. It should be pointed out that the size of travel-time anomalies detected by this measurement procedure do not necessarily correspond to the actual size of acoustic perturbations at a specific depth. It is perhaps more appropriate to interpret these structures as the projection of all the acoustic perturbations between 42 and 75 Mm in a single horizontal layer. It should be also mentioned that cross-covariances, obtained from different travel distances, have different travel times and the averaging is possible only after appropriate shifts which are based on quiet-Sun measurements.

4.3.5 Discussion

Detecting travel-time signatures of emerging-flux events in the deep convection zone requires a method with high sensitivity and S/N ratio. If the Cartesian approximation is used for the selection of annuli, the computation of cross-covariances can be significantly faster. However, the acoustic travel distances in this study are quite large and the curvature of the solar surface cannot be easily neglected. Figure 4.12 shows that the use of Cartesian approximation reduces the level of the signal by 20% – 25% even for a travel-time perturbation signature which, to the accuracy of the horizontal wavelength, is at the center of the map. The effect of the Cartesian approximation is

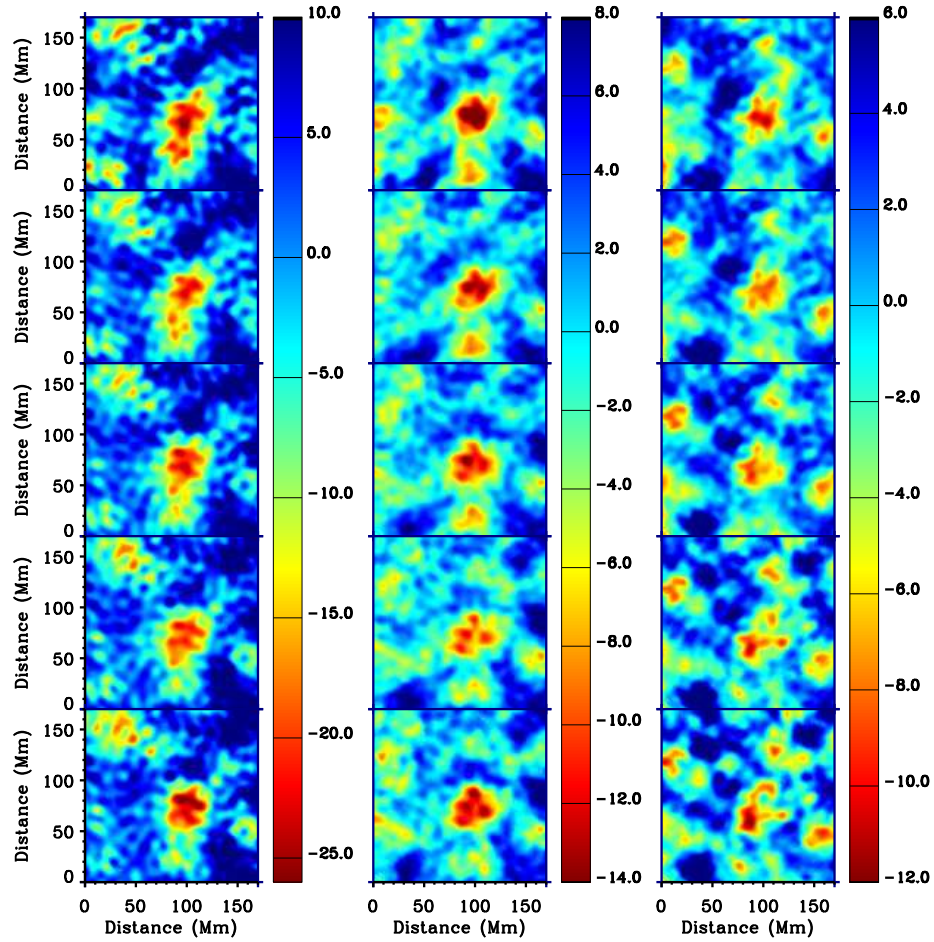


Figure 4.11: Phase travel-time perturbation maps of AR 10488 obtained from an 8-hour dataset centered at 03:30 UT, 26 October 2003. The maps were computed using the phase-speed filter shown in Figure 4.7 with solid line. Rows correspond to configurations with the same arc size and columns correspond to same depth. The number of arcs from top to bottom is 6, 8, 10, 12, and 14. The depth ranges from left to right are 64 – 75, 53 – 64, and 42 – 53 Mm. A combination of cross-covariances from these 3 depths can increase the S/N ratio as it is shown in Figure 4.5.

expected to be larger for travel-time signatures away from the center of the map. It should be pointed out that all the results presented in this chapter as well as the next one are obtained by computing the exact pixel-to-pixel distance in spherical geometry.

The size and strength of the detected travel-time anomalies depend on the sensitivity and the parameters of the measurement procedure such as the width of the phase-speed filter and the measurement scheme used for the computation of cross-covariances. It was reported (Braun, 2012) that an independent analysis with helioseismic holography could not detect significant subsurface travel-time perturbations associated with flux emergence. However, as it is shown in Figure 4.12, the discrepancy between the time-distance and the holography results can be explained by the differences in the measurement procedures such as the geometry, the phase-speed filter, and the depth averaging. The time-distance technique applied with the holography measurement procedure also fails to detect signatures of emerging flux due to low S/N ratio of this measurement procedure. More recently, Kholikov (2012) confirmed the detection of emerging magnetic flux using the time-distance technique and a measurement procedure similar to that used in this thesis.

We presented in this chapter a new measurement procedure and we explained the differences with previous methods. At each step the S/N ratio was estimated from measurements in emerging-flux and quiet-Sun regions and it was confirmed that our modifications indeed increase the S/N ratio. It was also shown that our measurement procedure is sensitive enough to detect travel-time signatures of strong emerging flux events, though additional modifications may further increase the S/N ratio in our measurements. We use this method in the next chapter to investigate the magnetic flux emergence in the deep convection zone.

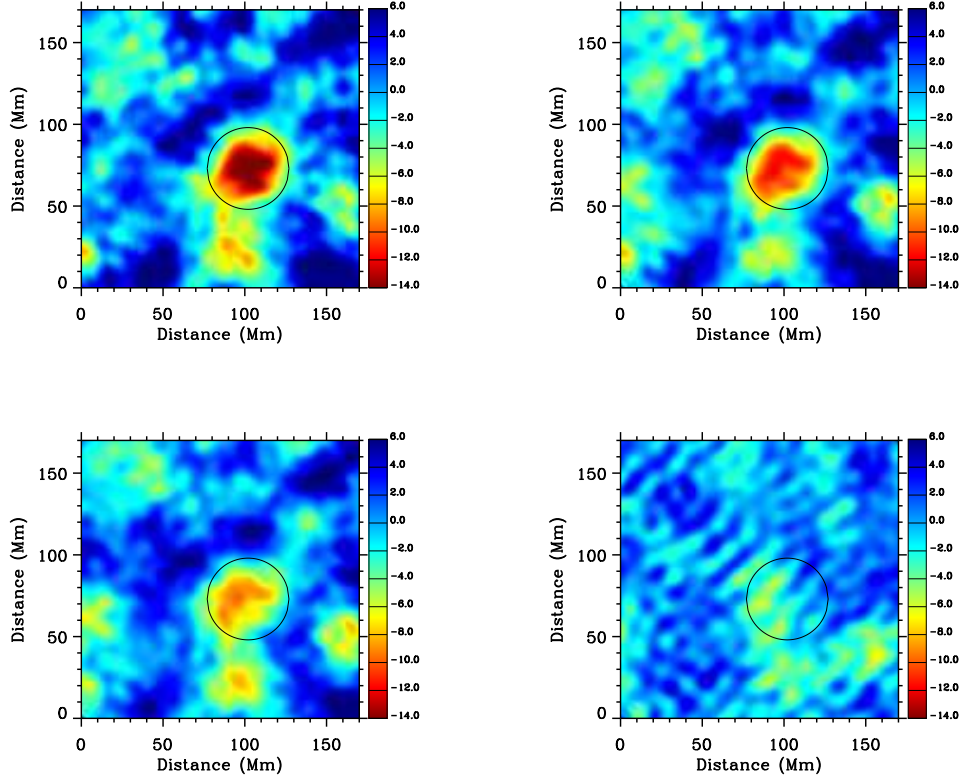


Figure 4.12: Upper left: Mean phase travel-time perturbation map of AR 10488 obtained from an 8-hour data set centered at 03:30 UT, 26 October 2003. The cross-covariances were computed using the phase-speed filter shown in Figure 4.7 with solid line and arcs with a size of 45 and four different orientations. The phase shifts inside the circle, which are caused by the emerging magnetic flux, have the maximum amplitude of 16.2 s. Upper right: Same as upper left except that the cross-covariances were computed assuming Cartesian geometry (instead of the correct spherical geometry). The maximum amplitude of the phase shifts inside the circle is reduced to 12 s. Lower left: Same as upper right except that the cross-covariances were computed using a Gaussian phase-speed filter (instead of the filter shown in 4.7). The signal inside the circle was further reduced to 9.7 s. Lower right: Mean phase travel-time perturbation map made with the methodology used in Braun (2012): Same as lower left except that the cross-covariances were computed using four Gaussian phase-speed filters at four target depths. The final phase travel-time map shown here is the average of the four individual maps. The strongest signal inside the circle is only 5.9 s, which is not sufficiently high to allow the detection of an emerging sunspot region. More details about the phase-speed filtering parameters can be found in Table 4.1. Figure adopted from Ilonidis, Zhao, & Kosovichev (2012b).

| Annulus No. | Annulus range (degrees) | Phase-speed ($\mu\text{Hz}/\ell$) | FWHM ($\mu\text{Hz}/\ell$) |
|-------------|-------------------------|-------------------------------------|------------------------------|
| 1 | 9.12 - 10.56 | 21.296 | 2.287 |
| 2 | 11.04 - 12.48 | 23.542 | 2.204 |
| 3 | 12.48 - 14.40 | 26.049 | 2.810 |
| 4 | 14.4 - 16.32 | 28.840 | 2.772 |
| 1-4 | 9.12 - 16.32 | 25.000 | 11.775 |

Table 4.1: Phase-speed filtering parameters used for the selected travel distances. The first four filters were used to make travel-time maps at four target depths between 42 and 75 Mm. These travel-time maps are then averaged to obtain the final travel-time map for the depth range of 42-75 Mm (Panel D of Figure 4.12). The last filter was used to make a travel-time map at the same depth range, 42 – 75 Mm, by averaging cross-covariances obtained from measurements at different focus depths (Panel C of Figure 4.12). The first four filters are courtesy of T. Duvall.

Chapter 5

Emerging Magnetic Flux II: Results¹

5.1 Detection of Emerging Magnetic Flux

We computed travel-time maps of five emerging-flux regions and nine quiet regions, with the exactly same measurement procedure, in order to estimate the noise level. We present in this section results from MDI observations that show the detected subsurface travel-time anomalies and the photospheric magnetic activity.

The emergence of Active Region (AR) 10488 was one of the strongest emerging flux events observed by SOHO/MDI (Figure 5.1). Doppler-shift and magnetic-field observations with 1-minute cadence are available for a long period before and after the start of emergence, with relatively few and short gaps, making this region a good example for helioseismic analysis. Magnetic-field observations before the emergence (Figure 5.2) show a very quiet region with no sign of the upcoming strong emerging-flux event. The emergence of AR 10488 started around 09:30 UT, 26 October 2003, about 30° east of the central meridian. Soon after the start of emergence, the magnetic flux rate steeply increased and had a high peak on 27 October at about 08:00 UT. A travel-time map, computed from an 8-hour data set and centered at 03:30 UT, 26 October, about 28.5 hours before the peak in flux rate, shows a strong negative

¹Part of this chapter was published in Science (Ilonidis, Zhao, & Kosovichev, 2011).

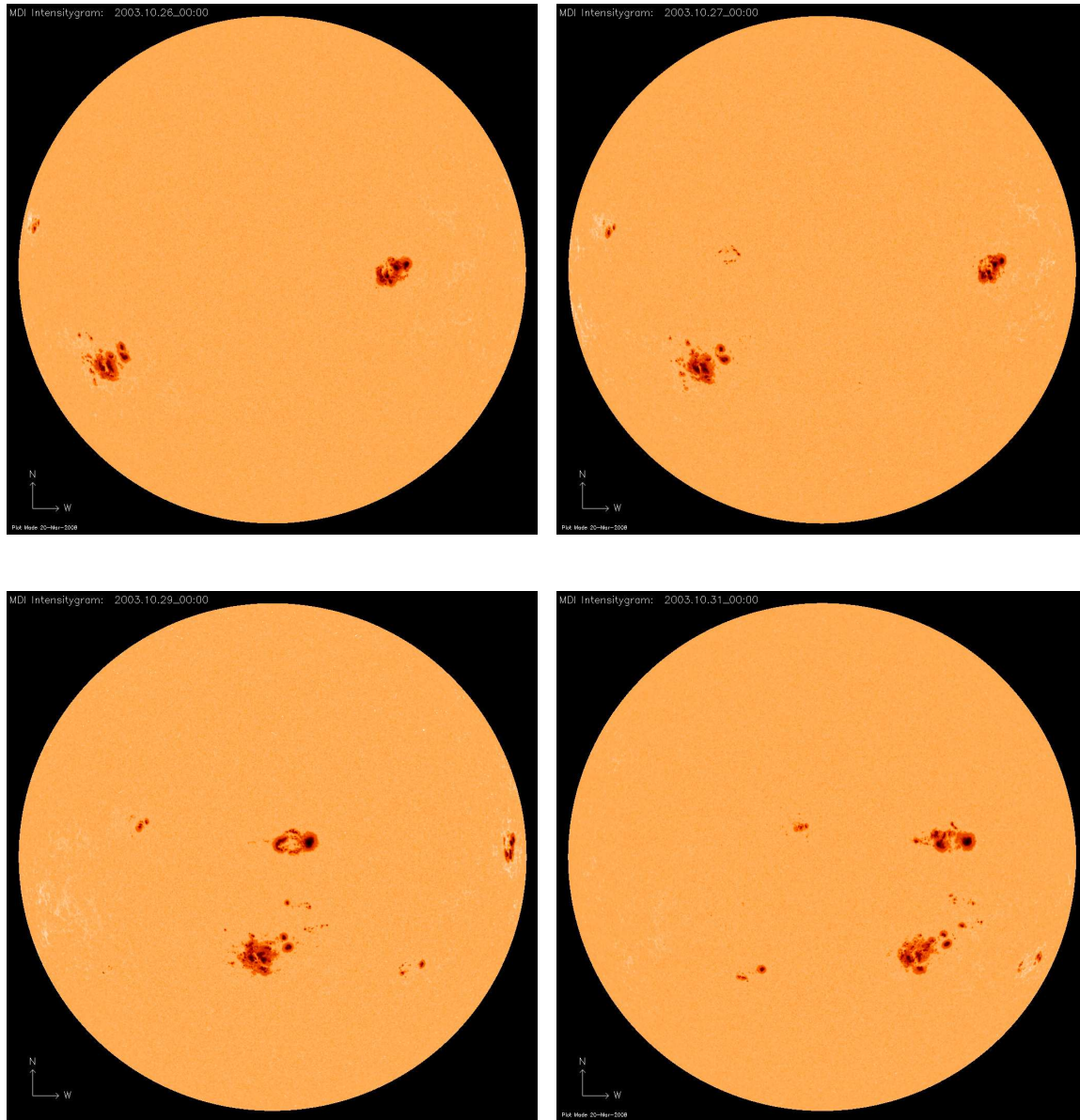


Figure 5.1: SOHO/MDI Intensity observations of AR 10488 emergence. From top left to bottom right, images were taken at 00:00 UT 26 October 2003, 00:00 UT 27 October 2003, 00:00 UT 29 October 2003, 00:00 UT 30 October 2003.

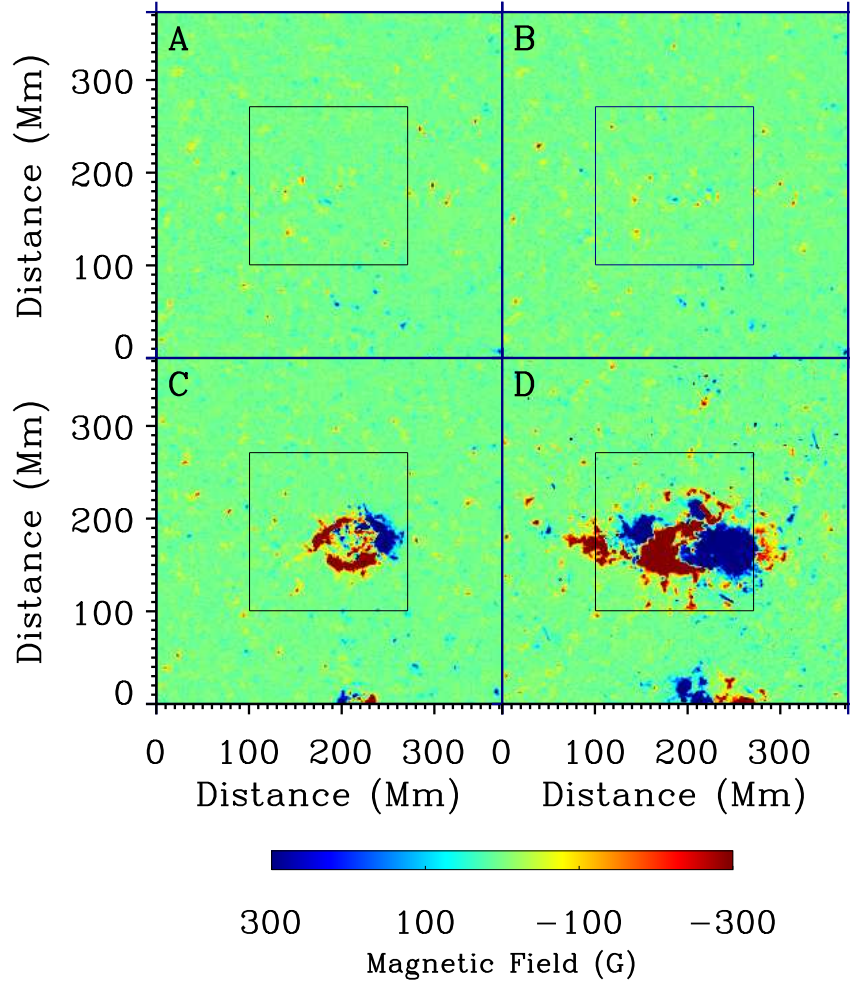


Figure 5.2: MDI magnetograms before and after the emergence of AR 10488. Panel A was taken at the time of strongest subsurface travel-time anomaly, panel B was taken at the start of emergence, panel C was taken 1 day after the start of emergence, and panel D was taken 4 days after the start of emergence. The squared area at the center corresponds to the region shown in travel-time map of Figure 5.3

travel-time perturbation at the same solar coordinates but deep inside the convection zone (Figure 5.3). This feature, with maximum travel-time anomaly of 16.3 s (relative to the quiet Sun), persisted for about 8 hours until the signal fell below the detection level. No other strong perturbations were detected at the same location before or after

the appearance of this perturbation. It should be pointed out that the development and decay of this strong subsurface travel-time anomaly happened several hours before the start of emergence at the surface. The magnetic field at that time and until the start of emergence was very quiet, and no signature of magnetic field emergence was visible in the magnetograms.

Active Regions 8164 and 8171 emerged in the northern and southern hemispheres at 04:00 UT, 23 February 1998 and 09:30 UT, 27 February 1998 respectively. They were both smaller and less active than AR 10488. The total unsigned magnetic flux and the flux rate of AR 8164 reveal that most of the flux emerged during a period of 2 days, with a strong peak in the flux rate around 08:00 UT, 24 February. The travel-time map of Figure 5.4 computed from an 8-hour dataset centered at 00:00 UT, 23 February, shows a strong signature of the emerging flux, with the maximum travel-time anomaly of 14.0 s. A similar signature, with the peak value of 12.5 s, appeared in the travel-time map of AR 8171 for a dataset centered at 04:30 UT, 27 February (Figure 5.5). These signatures first appeared several hours before the start of magnetic field emergence in the photosphere and at least 30 hours before the corresponding peaks in the flux rate.

Active Region 7978 emerged in the southern hemisphere at 17:00 UT, 06 July 1996. It continued to grow for the next 3 days, even though the magnetic flux rate was not as steep as in the previous cases. The travel-time map of Figure 5.6, centered at 11:30 UT, 06 July, displays a strong perturbation at the location of the emergence with maximum travel-time anomaly of 11.9 s.

All our measurements were carried out either in quiet-Sun regions, before the start of emergence, or in emerging flux regions where magnetic fields higher than 300 G had been masked. The travel-time anomalies of Figures 5.3 – 5.6 were all detected before the start of emergence and therefore they could not have been caused by surface magnetism effects (Lindsey & Braun, 2005; Zhao & Kosovichev, 2006). The sample of four emerging-flux events includes sunspot regions of different size and total magnetic flux, which were observed at different locations on the solar disc during different phases of the solar cycle. In all of these cases, the perturbation index shows high peaks only for a narrow time interval of the pre-emergence phase, but it stays

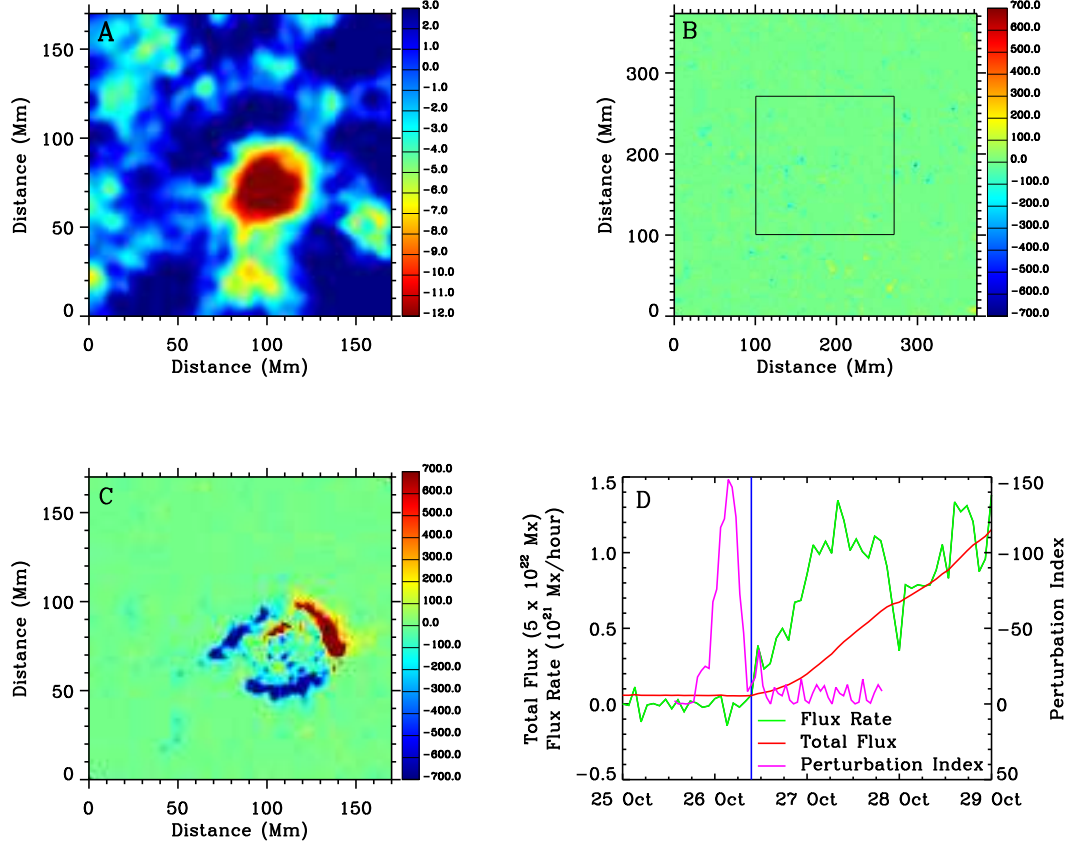


Figure 5.3: (A) Mean travel-time perturbation map (in seconds) of AR 10488 at a depth of 42 to 75 Mm, obtained from an 8-hour data set centered at 03:30 UT, 26 October 2003. (B) Photospheric magnetic field (in Gauss) at the same time as (A). The whole map corresponds to the region where the computations were carried out, whereas the squared area at the center corresponds to the region shown in (A). (C) Photospheric magnetic field (in Gauss) at the same location as (A) but 24 hours later. (D) Total unsigned magnetic flux (red line) and magnetic flux rate (green line) of AR 10488. The vertical blue line marks the start of emergence. The pink line shows the temporal evolution of the perturbation index (in units of 125 s Mm^2), which is defined as the sum of travel-time perturbations with values lower than -5.4 s , within the signature of (A). Figure adopted from Ilonidis, Zhao, & Kosovichev (2011).

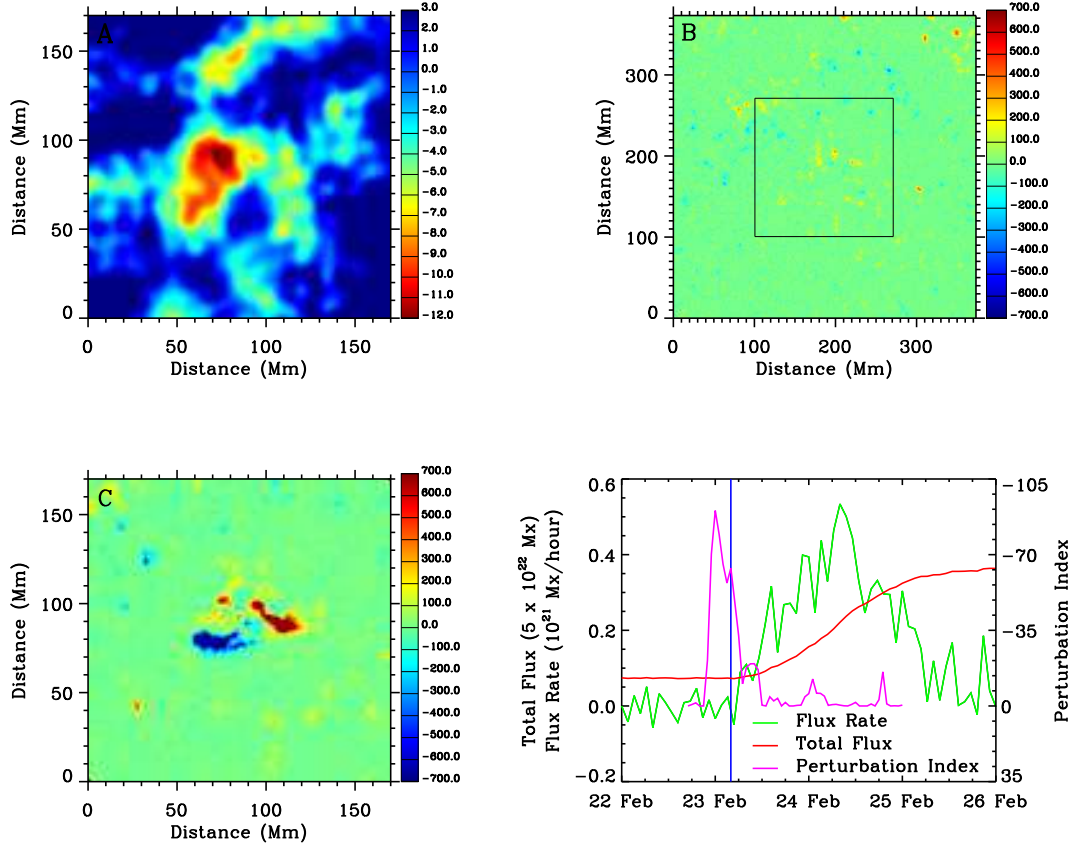


Figure 5.4: (A) Mean travel-time perturbation map (in seconds) of AR 8164 at a depth of 42 to 75 Mm, obtained from an 8-hour data set centered at 00:00 UT, 23 February 1998. (B) Photospheric magnetic field (in Gauss) at the same time as (A). The whole map corresponds to the region where the computations were carried out, whereas the squared area at the center corresponds to the region shown in (A). (C) Photospheric magnetic field (in Gauss) at the same location as (A) but 24 hours later. (D) Total unsigned magnetic flux (red line) and magnetic flux rate (green line) of AR 8164. The vertical blue line marks the start of emergence. The pink line shows the temporal evolution of the perturbation index (in units of 125 s Mm^2), which is defined as the sum of travel-time perturbations with values lower than -5.4 s , within the signature of (A). Figure adopted from Ilonidis, Zhao, & Kosovichev (2011).

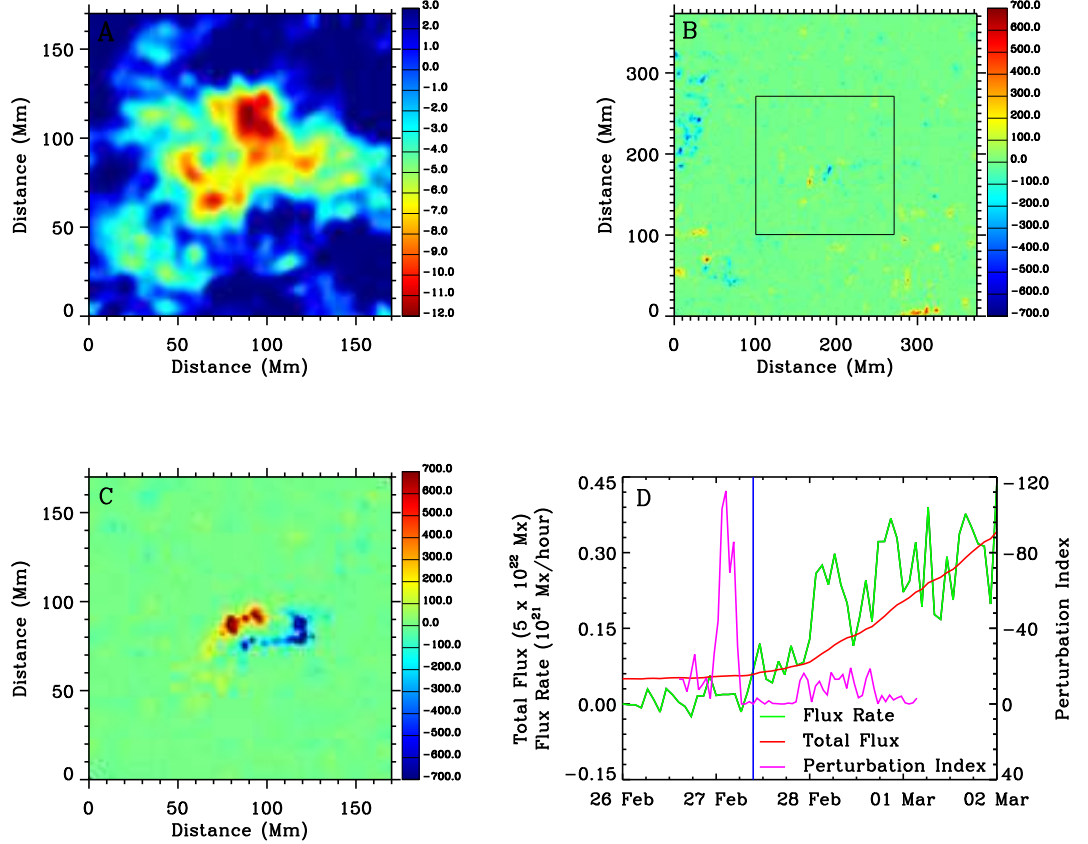


Figure 5.5: (A) Mean travel-time perturbation map (in seconds) of AR 8171 at a depth of 42 to 75 Mm, obtained from an 8-hour data set centered at 04:30 UT, 27 February 1998. (B) Photospheric magnetic field (in Gauss) at the same time as (A). The whole map corresponds to the region where the computations were carried out, whereas the squared area at the center corresponds to the region shown in (A). (C) Photospheric magnetic field (in Gauss) at the same location as (A) but 24 hours later. (D) Total unsigned magnetic flux (red line) and magnetic flux rate (green line) of AR 8171. The vertical blue line marks the start of emergence. The pink line shows the temporal evolution of the perturbation index (in units of 125 s Mm^2), which is defined as the sum of travel-time perturbations with values lower than -5.4 s , within the signature of (A). Figure adopted from Ilonidis, Zhao, & Kosovichev (2011).

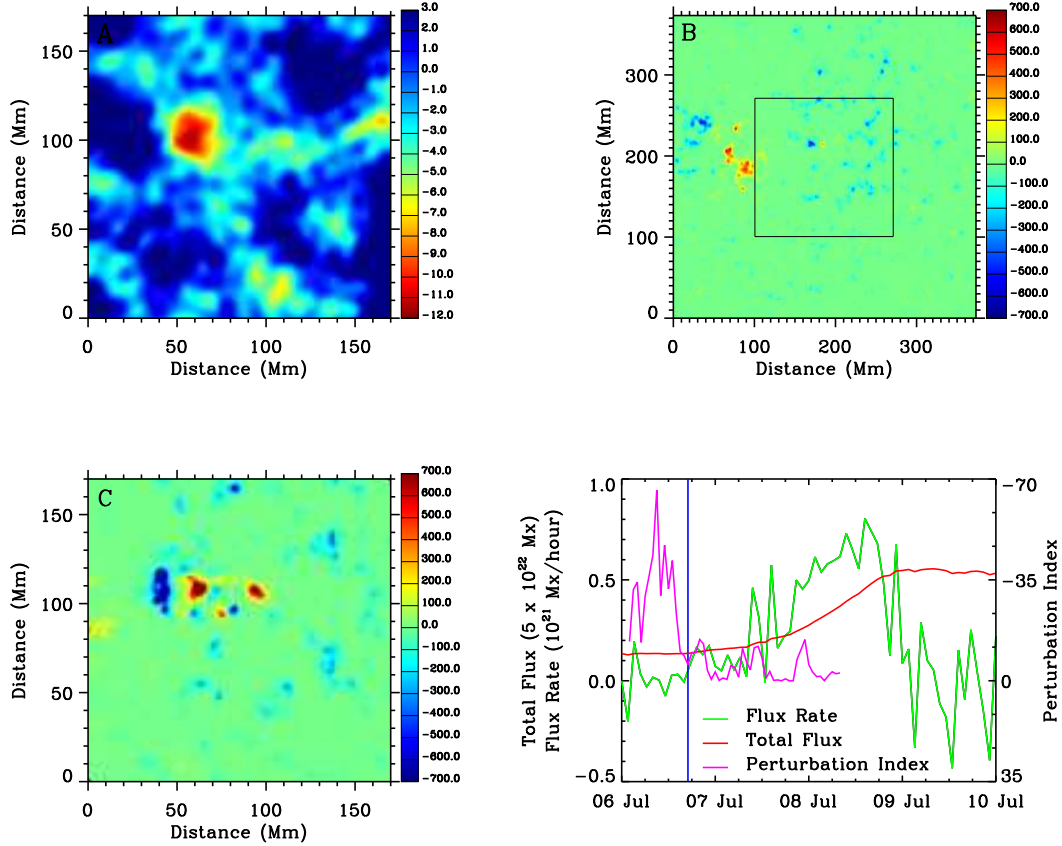


Figure 5.6: (A) Mean travel-time perturbation map (in seconds) of AR 7978 at a depth of 42 to 75 Mm, obtained from an 8-hour data set centered at 11:30 UT, 06 July 1996. (B) Photospheric magnetic field (in Gauss) at the same time as (A). The whole map corresponds to the region where the computations were carried out, whereas the squared area at the center corresponds to the region shown in (A). (C) Photospheric magnetic field (in Gauss) at the same location as (A) but 24 hours later. (D) Total unsigned magnetic flux (red line) and magnetic flux rate (green line) of AR 7978. The vertical blue line marks the start of emergence. The pink line shows the temporal evolution of the perturbation index (in units of 125 s Mm^2), which is defined as the sum of travel-time perturbations with values lower than -5.4 s , within the signature of (A). Figure adopted from Ilonidis, Zhao, & Kosovichev (2011).

very low after the start of emergence. This indicates that strong emerging flux events are detectable by our method. Indeed, our results show that 1 – 2 days after the detection of the anomalies, the magnetic structures associated with these anomalies reach the surface and cause high peaks in the photospheric magnetic flux rates. An emerging time of about 2 days from a depth of about 60 Mm is also consistent with numerical simulation models of emerging flux (see Fig. 18 of Fan, 2009). Our results also show an anticorrelation between the height of the perturbation index peak, and the time lag between this peak and the peak in the flux rate. Thus, higher peaks in the perturbation index may be caused by stronger magnetic fields that are more buoyant and rise to the surface faster.

In order to test the statistical significance of our results, we use the same method to analyze 9 datasets of quiet-Sun regions, with no emerging flux events. The analysis method (measurement scheme, phase-speed filtering, fitting etc) was exactly the same as for the emerging flux regions. The sample of 9 regions was selected from 3 different phases of the solar cycle and covers several locations of the solar disc up to 45° away from the disc center. These regions did not show substantial travel-time anomalies. The measured travel-time perturbations follow a Gaussian distribution with standard deviation of about 3.3 s (Figure 5.7), which is 3.6 – 4.9 times smaller than the peak signal of emerging flux regions. Such perturbations can be caused by realization noise, thermal variations, and weaker magnetic field structures that did not emerge soon in the photosphere.

The detection of emerging flux up to depths of about 70 Mm poses a low limit on the depth of generation of large magnetic regions. The average emergence speed from this depth up to the surface is estimated to be approximately 0.3 and 0.6 km/s for the analyzed weakest and strongest emerging flux events respectively.

Maps of the travel-time anomalies show that the signatures of emerging flux are mostly concentrated in circular areas with a typical size of 30 – 50 Mm. The horizontal wavelength of the acoustic waves at this depth is about 35 Mm, which poses limits on the size of subsurface structures that can be resolved as well as on the accuracy of the location of detected perturbations. This may also explain the absence of two distinct signatures, associated with the two magnetic polarities of sunspot regions, in

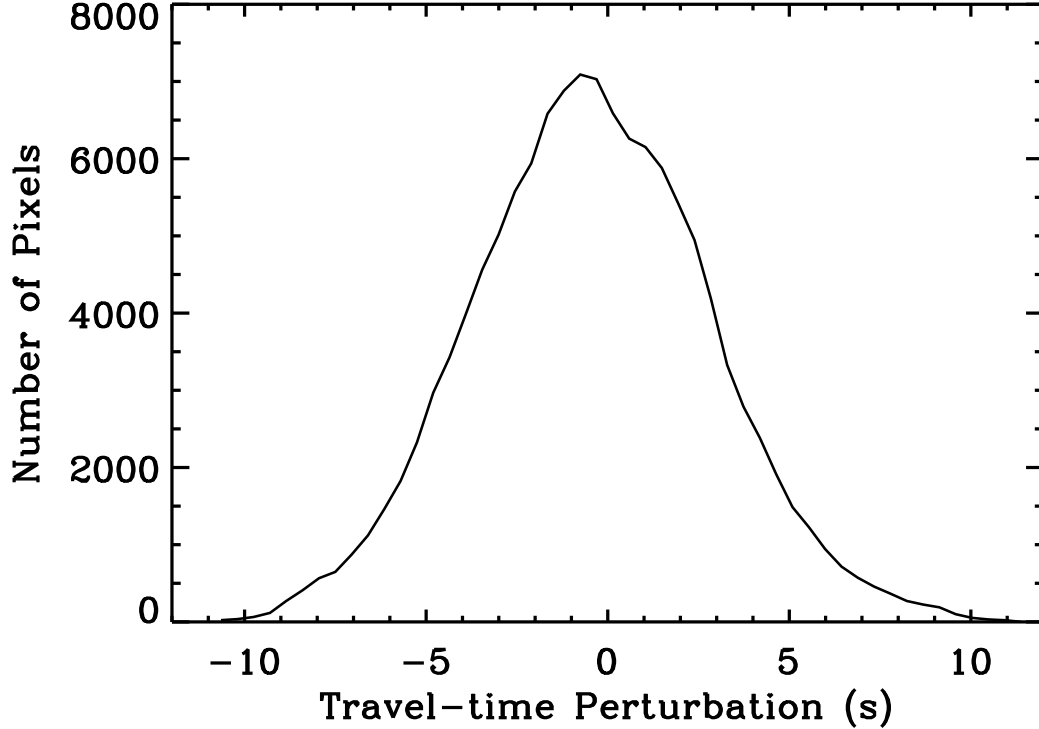


Figure 5.7: Distribution of travel-time perturbations measured in 9 quiet-Sun regions. The standard deviation of these measurements is 3.3 s which shows the statistical significance of the travel-time anomalies detected in emerging-flux regions. These anomalies have a S/N ratio of 3.6 – 4.9. Figure adopted from Ilonidis, Zhao, & Kosovichev (2011).

the travel-time maps. At the start of emergence in the photosphere, the two polarities are observed very close to each other, and only after this stage they progressively form an elongated bipolar feature. The travel-time perturbations caused by the 4 events are all negative with the maximum amplitude of 16.3 s. Recent theoretical studies, based on numerical simulations of emerging magnetic flux tubes, estimate the magnitude of travel-time anomalies at these depths to be of an order of 1 s or less (Birch, Braun, & Fan, 2010). This discrepancy will be explained in section 5.3. It should be also mentioned that the physical origin of the perturbations is not known, and the detected anomalies can be due to thermal rather than magnetic effects. In addition, a weak

magnetic flux at large depths is probably undetectable by our method. Therefore, the disappearance of the travel-time anomalies after the start of emergence does not necessarily imply that sunspots are disconnected from their roots.

5.2 Temporal Evolution and Depth Dependence

It is not clear, from the measurements presented in the previous section, whether the detected travel-time anomalies, as functions of time and depth, are relatively static or change size, shape, and strength. In this section we study the temporal evolution as well as the depth dependence of the detected travel-time perturbation signatures.

Figure 5.8 shows the temporal evolution of the travel-time anomalies in AR 10488. The first significant perturbation observed in the travel-time maps centered at 23:30 UT, 25 October 2003, 10 hours before the start of the active region emergence. During the next 4 – 5 hours (the time always corresponds to the middle time of an 8-hour data set used for cross-covariance computations) the perturbation increased in size and strength, creating a circular structure with typical size of about 50 Mm, and then gradually weakened and shrunk over the next 3 – 4 hours until the signal fell below the detection level. This picture is consistent with the emergence of a magnetic structure from deeper to shallower regions.

Similar results are also obtained for other active regions. Figures 5.9, 5.10, and 5.11 show the temporal evolution of the travel-time anomalies in ARs 8164, 8171, and 7978 respectively. These signatures are generally smaller and persist for about 5-8 hours. The region with the strongest perturbation (larger than ≈ 10 s) is mostly circular and in some cases (e.g. ARs 8164, 8171) is surrounded by a larger elongated area with weaker travel-time perturbations of the order of 6 – 10 s.

The detected signal of Figure 5.8 is the helioseismic signature of an emerging magnetic structure at depths of 42 – 75 Mm. In Figures 5.12 and 5.13, we divide the depth range of 42 – 75 Mm into 3 equal segments, 64 – 75 Mm, 53 – 64 Mm, and 42 – 53 Mm, and repeat the computations of travel-time maps with the same measurement procedure and phase-speed filter. The helioseismic signatures at each depth have smaller size and lower S/N ratio since the depth averaging of cross-covariance function

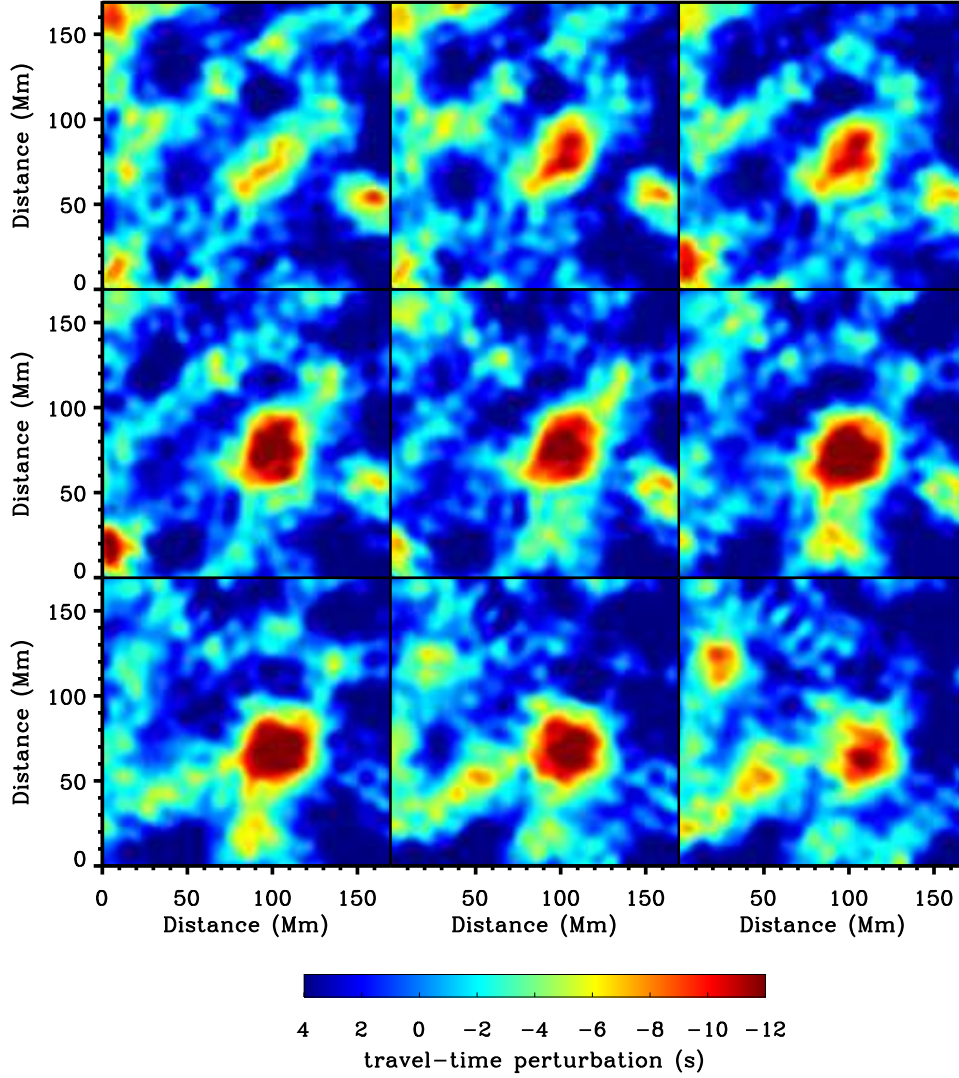


Figure 5.8: Temporal evolution of mean travel-time perturbation maps of AR 10488 at a depth of 42-75 Mm obtained from 8-hour MDI Doppler-shift datasets. From top left to bottom right, the maps are centered at 22:30 UT 25 October 2003, 23:30 UT, 00:30 UT 26 October 2003, 01:30 UT, 02:30 UT, 03:30 UT, 04:30 UT, 05:30 UT, 06:30 UT. A strong travel-time anomaly first appeared 10 hours before the start of emergence at the surface and persisted for about 8 hours.

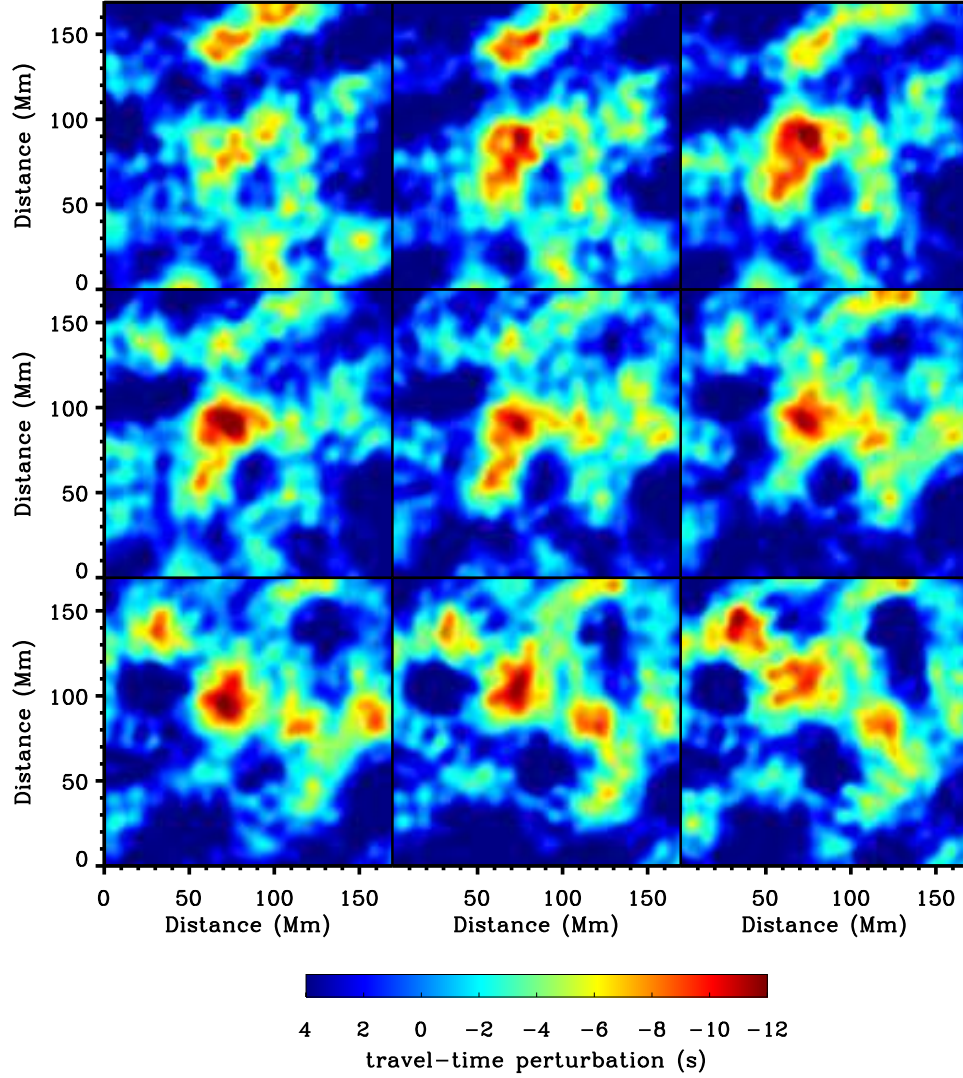


Figure 5.9: Temporal evolution of mean travel-time perturbation maps of AR 10488 at a depth of 42-75 Mm obtained from 8-hour MDI Doppler-shift datasets. From top left to bottom right, the maps are centered at 22:30 UT 25 October 2003, 23:30 UT, 00:30 UT 26 October 2003, 01:30 UT, 02:30 UT, 03:30 UT, 04:30 UT, 05:30 UT, 06:30 UT. A strong travel-time anomaly first appeared 10 hours before the start of emergence at the surface and persisted for about 8 hours.

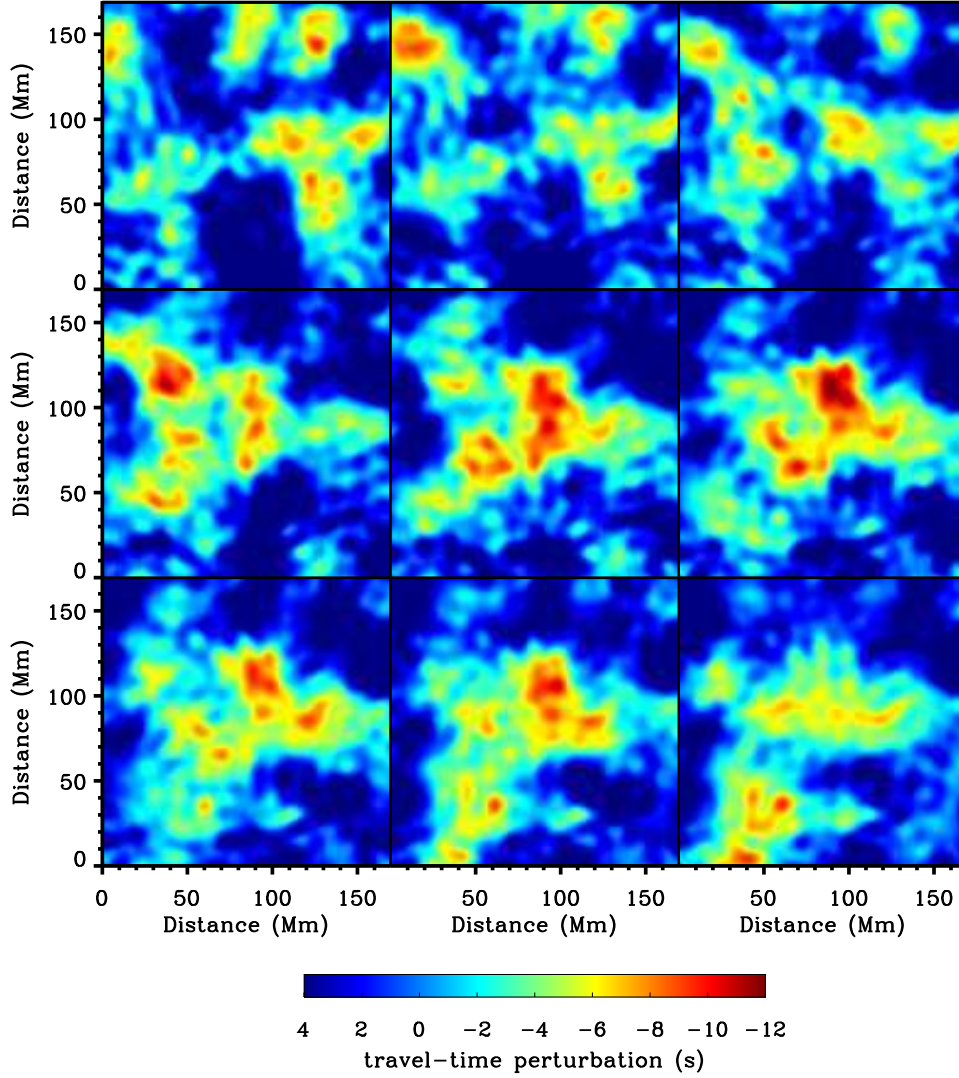


Figure 5.10: Temporal evolution of mean travel-time perturbation maps of AR 10488 at a depth of 42-75 Mm obtained from 8-hour MDI Doppler-shift datasets. From top left to bottom right, the maps are centered at 22:30 UT 25 October 2003, 23:30 UT, 00:30 UT 26 October 2003, 01:30 UT, 02:30 UT, 03:30 UT, 04:30 UT, 05:30 UT, 06:30 UT. A strong travel-time anomaly first appeared 10 hours before the start of emergence at the surface and persisted for about 8 hours.

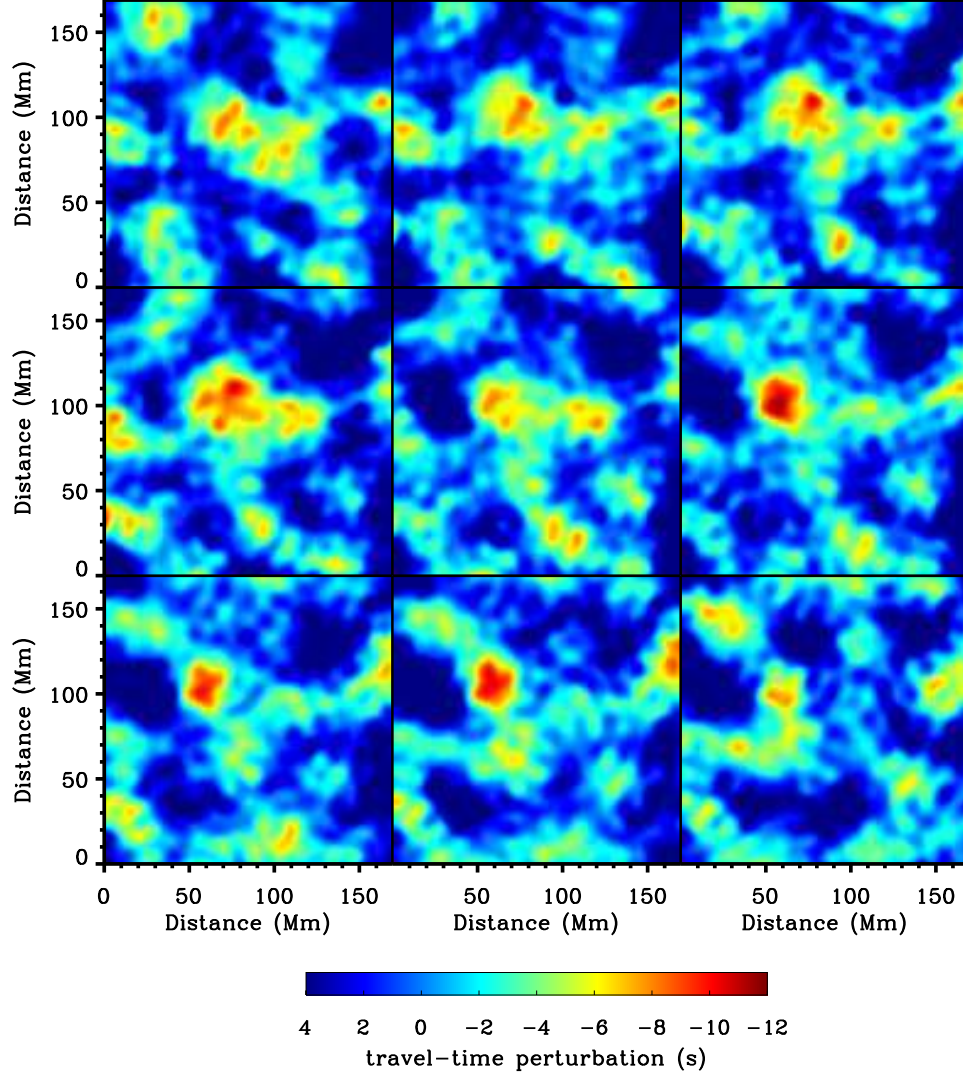


Figure 5.11: Temporal evolution of mean travel-time perturbation maps of AR 10488 at a depth of 42-75 Mm obtained from 8-hour MDI Doppler-shift datasets. From top left to bottom right, the maps are centered at 22:30 UT 25 October 2003, 23:30 UT, 00:30 UT 26 October 2003, 01:30 UT, 02:30 UT, 03:30 UT, 04:30 UT, 05:30 UT, 06:30 UT. A strong travel-time anomaly first appeared 10 hours before the start of emergence at the surface and persisted for about 8 hours.

has been reduced by a factor of 3. Nonetheless, strong phase travel-time shifts are still detectable at the location of emergence. These perturbations first appear at the deepest layer of 64 – 75 Mm, shift a few hours later to the middle layer, and gradually propagate to the top layer approximately 5 hours after the initial detection. Figure 5.14 shows the normalized perturbation at each depth as a function of time. The largest overlap of the three curves occurs around 03:30 UT which explains why the strongest travel-time anomaly in the combined measurements between 42 and 75 Mm is detected at this time. The emergence of the helioseismic signatures from deeper to shallower regions is a strong evidence that these signatures are associated with the flux emergence.

5.3 Frequency Perturbations

In this section, we examine the relationship between the phase-shifts and the frequency shifts of the cross-covariance function. The phase travel-time shifts measured in this study are determined by fitting a specific peak of the cross-covariance function and thus, the detected perturbations have information only about the position of this fitted peak. Zhao, Kosovichev, & Ilonidis (2011) showed with time-distance measurements in a sunspot region that the interaction of acoustic waves with the magnetic field can cause more complicated effects than a uniform shift of the cross-covariance function that is expected from a wave-speed perturbation. Figure 5.15 shows cross-covariance functions computed from quiet and emerging flux regions using acoustic frequencies mainly from 2.5 to 4.5 mHz with peak around 3.3 mHz. The two functions have clearly different frequency. The phase-shifts are small for time lags around 65 – 70 minutes but due to large frequency perturbation, the phase shifts are much larger for smaller time lags. The frequency perturbation can be determined quantitatively from the Gabor wavelet fitting as well. Panels C and D of Figure 5.15 show travel-time and frequency perturbation maps of this region. It appears that the location of the detected travel-time perturbations is same as that of the detected frequency perturbations, implying that the measured phase travel-time perturbations are related with frequency perturbations at locations where acoustic waves interact

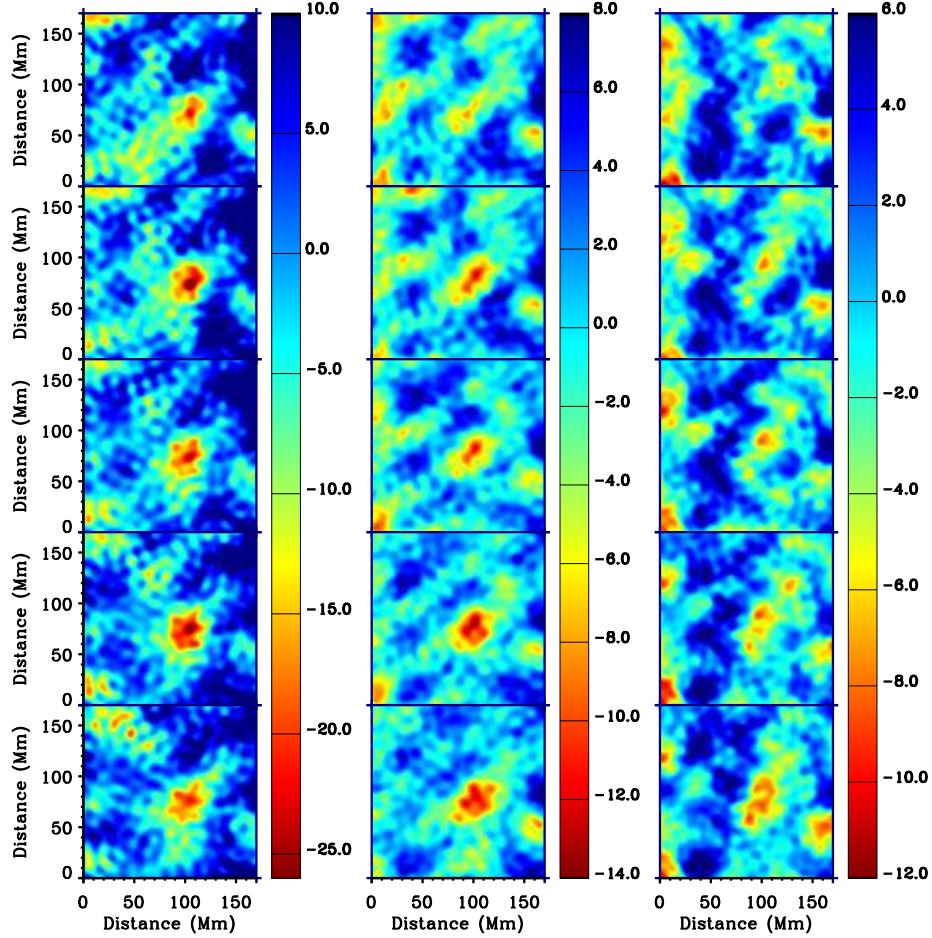


Figure 5.12: Temporal evolution of mean travel-time perturbation maps of AR 10488 at 3 different depths obtained from 8-hour MDI Doppler-shift datasets. Columns from left to right correspond to depths of 64-75, 53-64, and 42-53 Mm respectively. From top to bottom the maps are centered at 22:30 UT 25 October 2003, 23:30 UT, 00:30 UT 26 October 2003, 01:30 UT, 02:30 UT. A strong travel-time anomaly appears first at the deepest layer, it propagates within 2-3 hours to the middle layer and 5-6 hours later it is detected at the top layer (see also next figure).

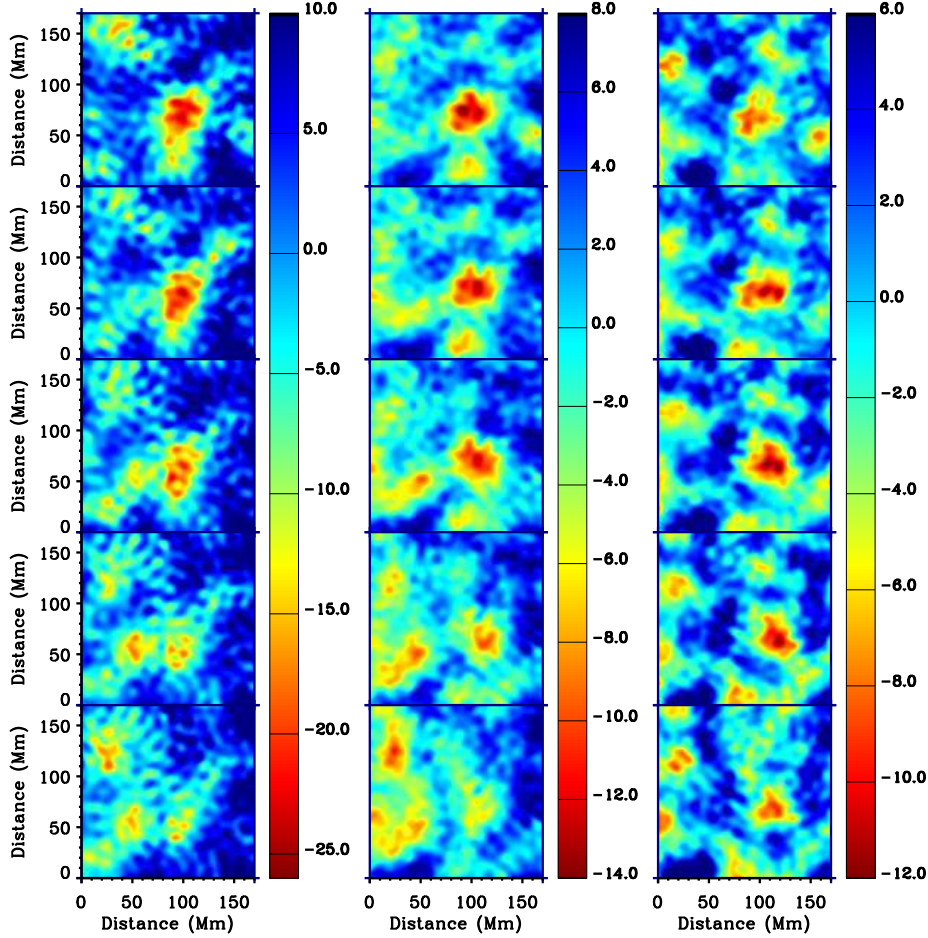


Figure 5.13: Temporal evolution of mean travel-time perturbation maps of AR 10488 at 3 different depths obtained from 8-hour MDI Doppler-shift datasets. Columns from left to right correspond to depths of 64-75, 53-64, and 42-53 Mm respectively. From top to bottom the maps are centered at 03:30 UT 26 October 2003, 04:30 UT, 05:30 UT, 06:30 UT, 07:30 UT. A strong travel-time anomaly appears first at the deepest layer, it propagates within 2-3 hours to the middle layer and 5-6 hours later it is detected at the top layer (see also previous figure).

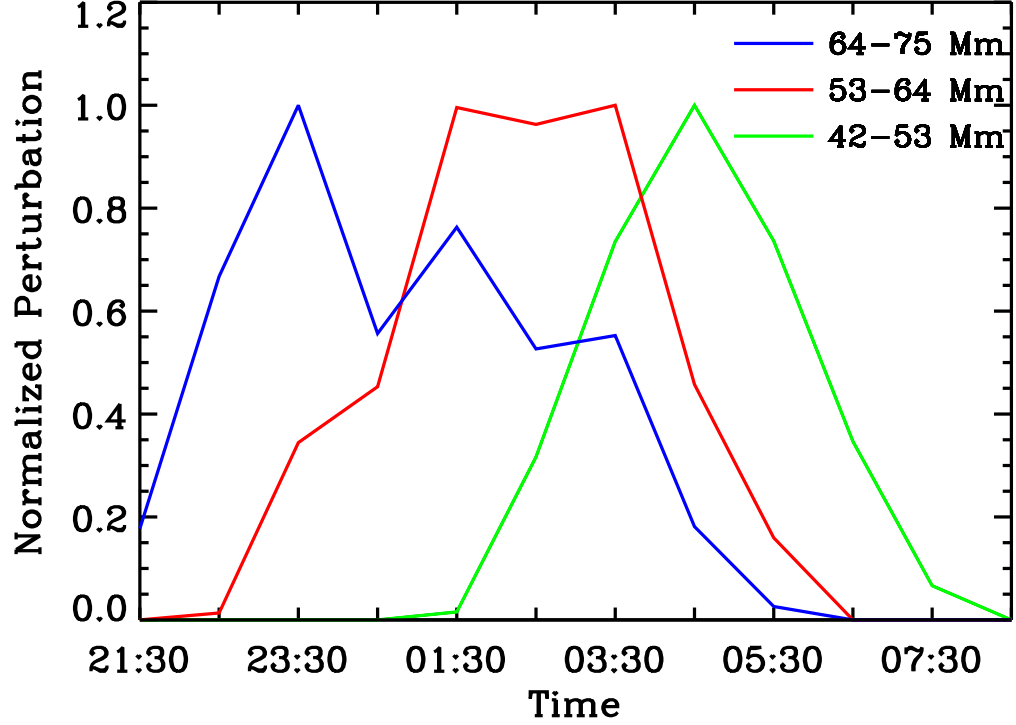


Figure 5.14: Temporal evolution of the normalized perturbation at depths of 42 – 53 Mm (green line), 53 – 64 Mm (red line), and 64 – 75 Mm (blue line). The normalized perturbation is defined as the sum of travel-time perturbations with values lower than -3.0σ , within the travel-time anomalies shown in Figures 5.12 and 5.13, normalized to the maximum value at each depth. The time starts at 21:30 UT, 25 October 2003. The travel-time anomalies emerge ~ 20 Mm in ~ 5 hours with an estimated average speed of the order of ~ 1 km/s.

with the emerging flux. It should be noted that the phase shifts are not symmetric with respect to the center of the cross-covariance function which is between 60 and 65 minutes.

We now study the acoustic frequency dependence of the detected cross-covariance frequency shifts. We repeat in Figures 5.16 and 5.17 the time-distance analysis of the emerging-flux region using mainly higher acoustic frequencies from about 3 to 5 mHz with peak around 3.6 mHz and from 3 to 5.5 mHz with peak around 4 mHz. The

behavior of the cross-covariance function changes drastically. The negative frequency shift found in Figure 5.15 now changes to a strong positive shift for frequencies around 4 mHz. The intermediate acoustic frequency range around 3.6 mHz does not show significant cross-covariance frequency shifts. The travel-time and frequency perturbation maps show the high correlation between the detected phase-shifts and the associated frequency shifts. These shifts, like in the previous case, are not symmetric with respect to the center of the cross-covariance function but now the zero-shift point seems to be on the left side.

5.4 Results from SDO/HMI and GONG

All the results presented so far are obtained by analyzing SOHO/MDI data. In this section we present helioseismic measurements of emerging flux using data from other instruments. We analyze HMI observations of AR 11158 and GONG observations of AR 10488. A discussion on the comparison of MDI and GONG results follows at the end of this section.

Active region 11158 started emerging on the solar disc around 15:30 UT, 10 February 2011. Magnetic field observations of the total flux and the flux emergence rate (Figure 5.18) show that most of the flux emerged during a strong emerging flux event which started approximately two days after the start of emergence and persisted for about two days. A high peak in the flux rate was observed on 13 February 2011 around 06:00 UT. Maps of the subsurface travel-time perturbations, at the same depth range of 42 – 75 Mm and with the same measurement procedure as in previous cases, show that strong travel-time anomalies can be detected at the location of emergence 1 – 2 days before the high peak in the flux rate but not earlier. This shows that the weak flux emergence during the first two days is probably undetectable by our method and perhaps only the very strong emerging flux events that cause high peaks in the flux rate can be detected by this method. Whether the detection occurs before or after the start of emergence depends on the relative position of the peak in the flux emergence rate with respect to the start of emergence.

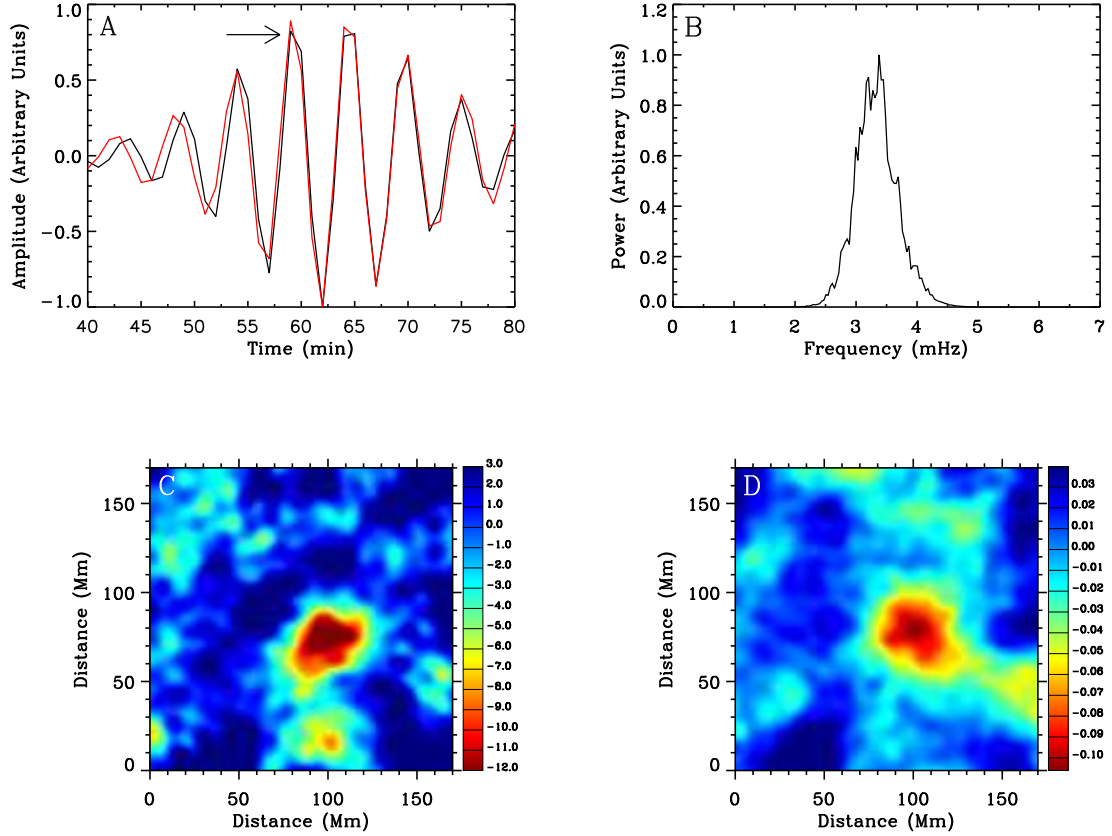


Figure 5.15: Travel-time and frequency perturbations at frequencies around 3.3 mHz. (A) Cross-covariance function from a quiet region (black) and an emerging-flux region (red). The arrow indicates the location of the fitted peak. (B) Power distribution of the oscillation signals used for the computation of cross-covariance functions in (A). These oscillation signals were selected with a phase-speed filter and a frequency filter. (C) Mean travel-time perturbation map (in seconds) of the emerging-flux region computed using the oscillation signals in (B). (D) Frequency perturbation map (in mHz) of the same region as in (C).

The temporal evolution of the detected travel-time anomalies is presented in Figure 5.19. The travel-time maps show significant perturbations for a total period of about 12 hours. This is larger than the typical perturbation duration of 5 – 8 hours that was found in previous cases. However, the travel-time maps also show that there are 2 – 3 distinct perturbation signatures and the 12-hour interval begins with the appearance of the first perturbation signature and ends with the decay of the last

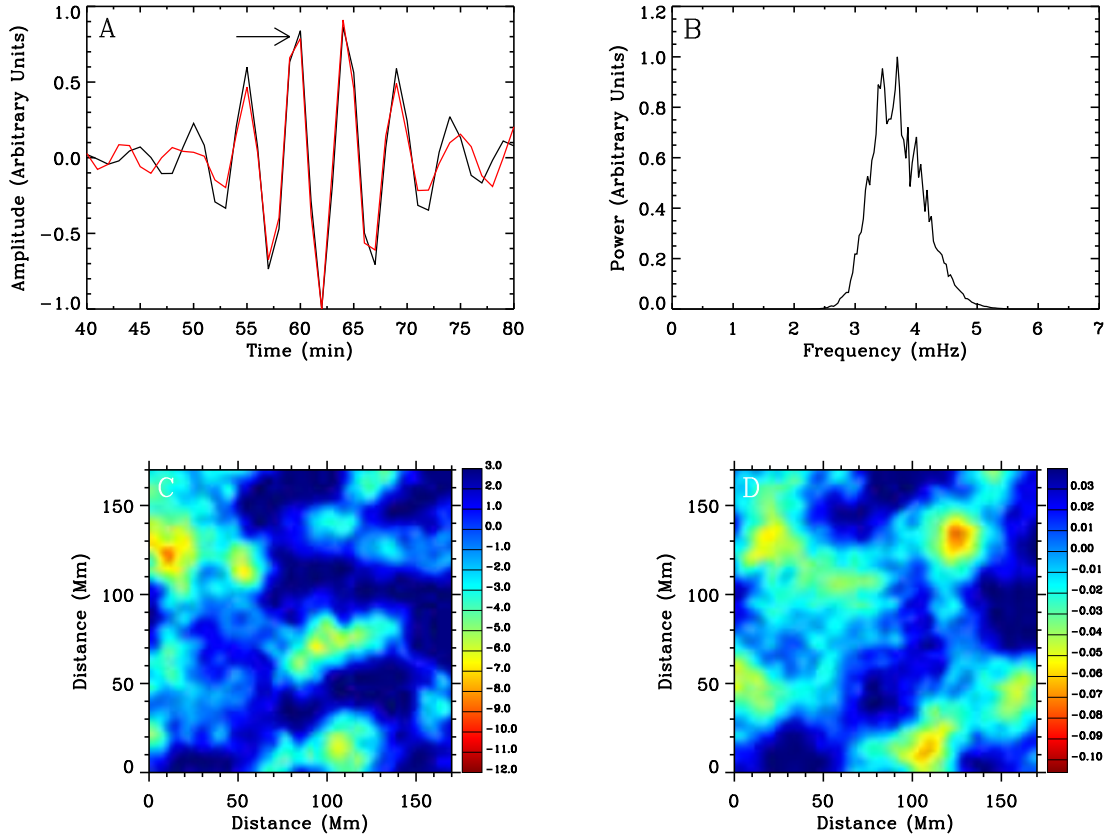


Figure 5.16: Travel-time and frequency perturbations at frequencies around 3.7 mHz. (A) Cross-covariance function from a quiet region (black) and an emerging-flux region (red). The arrow indicates the location of the fitted peak. (B) Power distribution of the oscillation signals used for the computation of cross-covariance functions in (A). These oscillation signals were selected with a phase-speed filter and a frequency filter. (C) Mean travel-time perturbation map (in seconds) of the emerging-flux region computed using the oscillation signals in (B). (D) Frequency perturbation map (in mHz) of the same region as in (C).

perturbation signature. The duration of each signature is less than ~ 8 hours which is consistent with the previous examples.

The detection of 2–3 subsurface distinct signatures may be related with the complicated configuration of the flux emergence in the photosphere. Unlike the compact emerging flux events observed in the previous cases, the magnetic flux in AR 11158

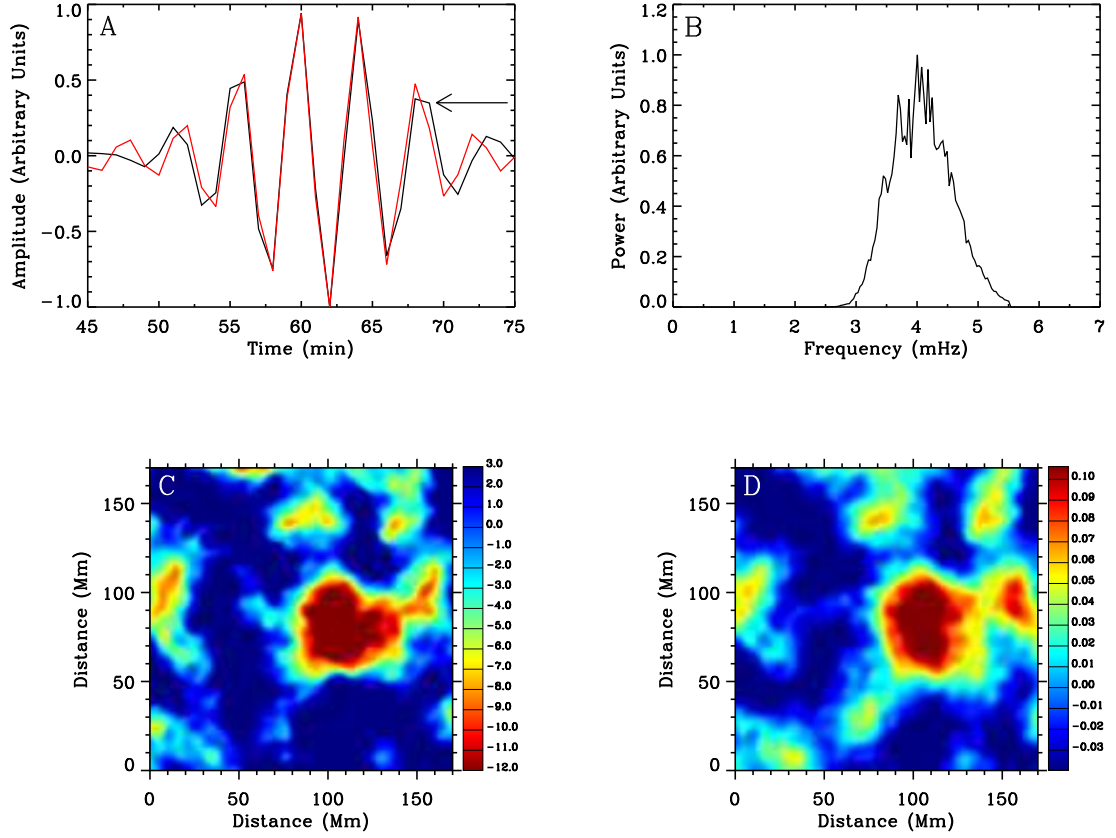


Figure 5.17: Travel-time and frequency perturbations at frequencies around 4 mHz. (A) Cross-covariance function from a quiet region (black) and an emerging-flux region (red). The arrow indicates the location of the fitted peak. (B) Power distribution of the oscillation signals used for the computation of cross-covariance functions in (A). These oscillation signals were selected with a phase-speed filter and a frequency filter. (C) Mean travel-time perturbation map (in seconds) of the emerging-flux region computed using the oscillation signals in (B). (D) Frequency perturbation map (in mHz) of the same region as in (C).

is extended over a large region and shows several centers of emergence. The detection of distinct travel-time perturbation signatures may be caused by the subsurface configuration of the field but helioseismic analysis of more emerging-flux regions is needed to further support this suggestion.

We now use GONG observations to analyze AR 10488 and compare the GONG and MDI travel-time maps. Unfortunately, GONG observations have a long gap around

the detection time of the strongest perturbation signature. Due to this restriction, we can only make travel-time maps after 06:30 UT 26 October 2003. At this time, the travel-time anomaly have smaller size and strength but it is still detectable. Figure 5.20 shows a travel-time map around the location of emergence computed from GONG observations and the corresponding MDI map at the same time. The travel-time perturbation signature can be detected in the GONG map as well and the size, the strength, and the location of the signature are similar to those of the MDI map. The independent detection of this perturbation signal by a ground-based instrument validates to some extent our method. The two maps show good agreement not only for the strongest travel-time perturbation signature which is caused by the emerging flux but also for other weaker perturbations, far from the location of the emergence. It is not known at this point whether these weak travel-time perturbations are caused by real acoustic perturbations in the solar interior or they appear due to noise in the data. The good agreement between GONG and MDI indicates that most perturbations in the map have solar origin and instrumental or other effects are probably not important in this case.

5.5 Discussion

First of all, it should be pointed out that the detection of a travel-time anomaly for about 8 hours does not necessarily mean that the emergence of new flux takes place for only 8 hours. It has been shown that travel-time signatures up to ≈ 10 s can be found in quiet-Sun regions as well and thus the detection of an emerging-flux event is possible only if the measured perturbations are larger than ≈ 10 s. These perturbations may depend on the flux density and perhaps other physical quantities and therefore a detection with the current measurement procedure may not be possible for weak magnetic flux or under other conditions.

Our measurements show that the detection of travel-time signatures caused by emerging-flux events is easier at depths between 42 and 75 Mm. However, the nature of these signatures is not known yet and therefore it is not easy to explain why such signatures have not been detected yet at deeper or shallower regions. One possible

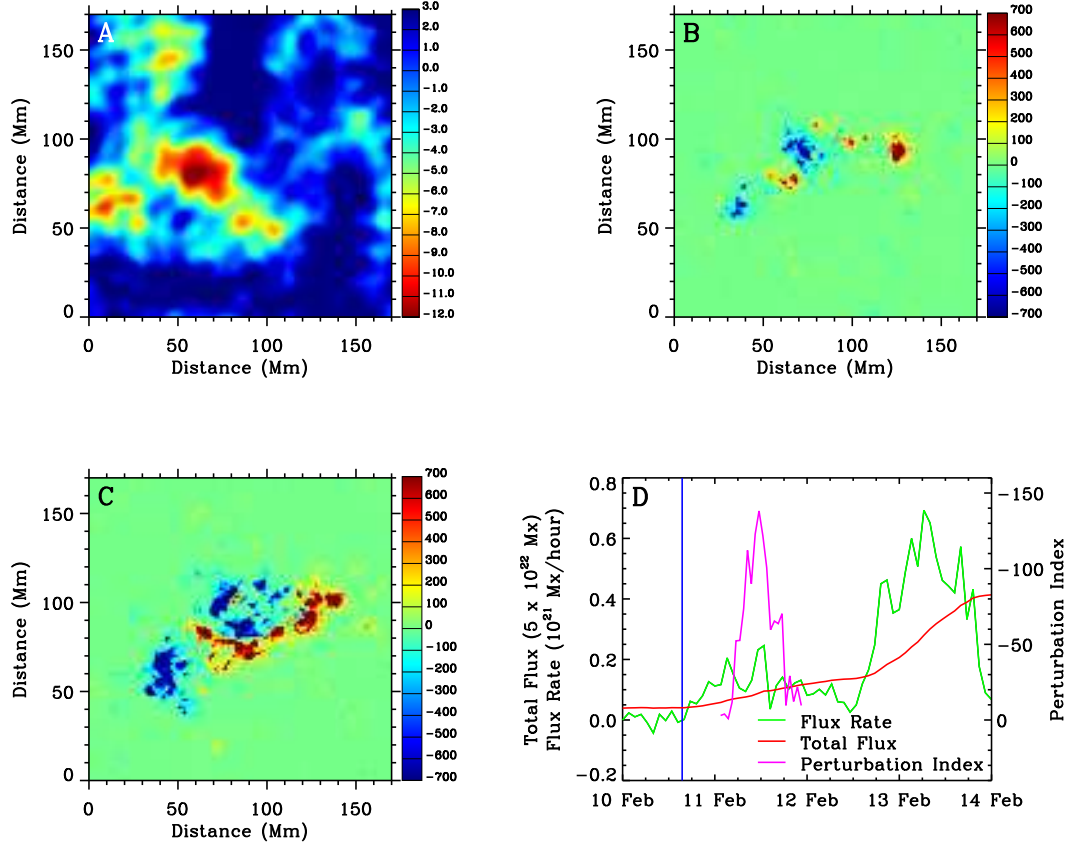


Figure 5.18: (A) Mean travel-time perturbation map (in seconds) of AR 11158 at a depth of 42 to 75 Mm, obtained from an 8-hour data set centered at 08:30 UT, 11 February 2011. (B) Photospheric magnetic field (in Gauss) at the same time as (A). (C) Photospheric magnetic field (in Gauss) at the same location as (A) but 24 hours later. (D) Total unsigned magnetic flux (red line) and magnetic flux rate (green line) of AR 11158. The vertical blue line marks the start of emergence. The pink line shows the temporal evolution of the perturbation index (in units of 125 s Mm^2), which is defined as the sum of travel-time perturbations with values lower than -5.4 s , within the signature of (A).

explanation is that shallow regions are sampled by acoustic waves with low phase-speed and mainly small horizontal wavelengths while deep regions are sampled by waves with high phase speeds and mainly large horizontal wavelengths. If the detected signatures are the result of interaction between the acoustic waves and the magnetic field which occurs when the size of the horizontal wavelength is roughly equal to the

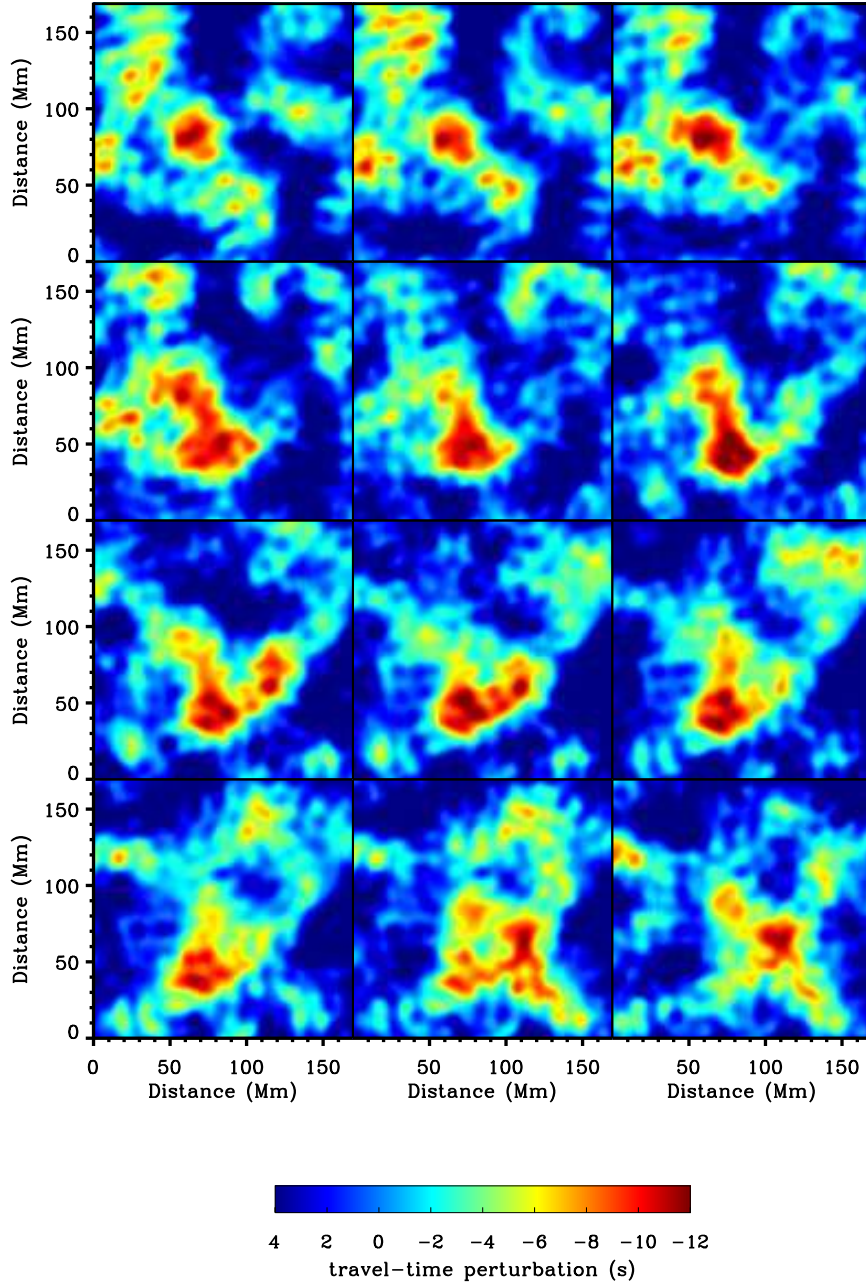


Figure 5.19: Temporal evolution of mean travel-time perturbation maps of AR 11158 at a depth of 42-75 Mm obtained from 8-hour MDI Doppler-shift datasets.

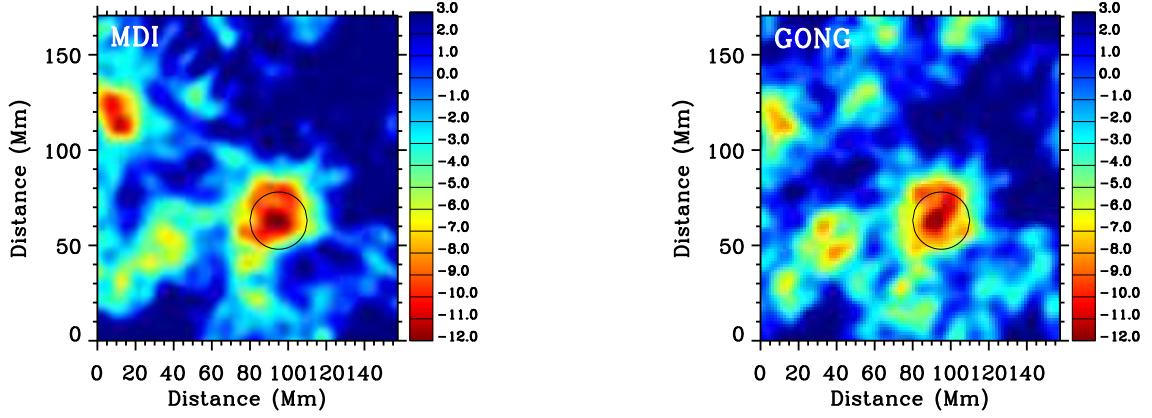


Figure 5.20: Comparison of SOHO/MDI (left) and GONG (right) travel-time maps of AR 10488. The circle shows the region of the travel-time anomaly.

size of the emerging flux tube (or the effective size of a bundle of emerging flux tubes) then the detection would be possible only at a limited depth range. At a depth of 60 Mm the horizontal wavelength is ≈ 32 Mm and the typical size of the emerging signatures in Figure 5.12 is ≈ 30 Mm (which is larger than the smallest structures that can be resolved in these maps with size of ≈ 15 Mm). Thus, at this depth the horizontal wavelength is roughly equal to the size of the emerging flux tubes and the pressure scale height is ≈ 17 Mm so a detection may be possible only at depths of roughly 60 ± 17 Mm.

It is interesting to compare estimates of the emerging speed from Figures 5.12 and 5.13 with the average emerging speed from a depth of about 60 Mm until the surface estimated in section 5.1. The purpose here is not to make a very accurate comparison but to check if at least the two estimates have the same order of magnitude. The travel-time signatures in Figures 5.12 – 5.13 seem to propagate roughly 20 Mm (from the deepest to the shallowest layer) in about five hours and that gives an emerging speed of about 1 km/s. This is in agreement with estimates of emerging speed from previous studies (Kosovichev, Duvall, & Scherrer, 2000; Zharkov & Thompson 2008). In section 5.1 we estimated from the detection of the maximum signal at the depth of about 60 Mm and the peak in the flux rate at the surface that the flux emerged with an average speed of 0.6 km/s. The two estimates agree within an order of magnitude,

and this is reasonable given all the assumptions that are involved in this calculation. There are several reasons that could perhaps explain why a better agreement is not found. First, the emerging flux may actually decelerate at some depth between 60 Mm and the surface as it was found by some numerical simulation studies (Toriumi & Yokoyama, 2010, 2011). Second, the magnitude of the travel-time signatures vary strongly as a function of depth, which can underestimate the emerging time from about 70 to 50 Mm, overestimating the emerging speed at this depth. The strongest travel-time shifts in Figures 5.12 and 5.13 change by almost a factor of 2 from 70 Mm to 50 Mm. However, the measurements at each depth are not completely independent since the sensitivity of acoustic waves to external perturbations extends far beyond the ray path. Given that the strongest signal in the middle layer, for example, is detected when there is still a comparable or stronger signal in the deepest layer, we expect that the deeper signal affects the measurement in the shallower region, shifting the strongest signals in the shallower region at earlier times. This effect may also overestimate the emerging speed. Third, the travel-time perturbation signature at the depth of 60 Mm is detected several hours before the start of emergence at the surface but it needs about 1 day to emerge at the surface. Soon after the start of emergence, strong downflows developed in the emerging-flux region may reduce the estimated emerging speed. At this point it is not clear which of the above effects is more prominent.

The detected cross-covariance frequency shifts, their acoustic frequency dependence, and the asymmetric form of the cross-covariance function show that there might be a complicated interaction between acoustic waves and the interior magnetic field. These effects may not be possible to be explained by simple sound-speed perturbations in the solar interior which is expected to cause mainly uniform shifts of the cross-covariance function without strong frequency dependence. We conclude from the above that the magnitude of the detected 12-16 s phase travel-time shift cannot be simply used to estimate a sound speed perturbation in the solar interior without taking into account all the other changes in the cross-covariance function. Comparison of phase travel-time maps between different methods also need to be

done carefully since different fitting methods are not always equivalent and the measured phase shifts may not agree. It is clear that phase travel-time perturbations have only limited information about the subsurface magnetic fields and helioseismic studies on the interaction of acoustic waves with magnetic fields need the development of methods of waveform heliotomography as suggested by Zhao, Kosovichev, & Ilonidis (2011).

The detection of emerging magnetic flux in the deep convection zone has also important practical implications. Predicting solar magnetic activity is a valuable tool for space weather forecast. Our technique of imaging the deep solar interior, combined with uninterrupted helioseismic observations of the Solar Dynamics Observatory and the far-side imaging technique (Lindsey & Braun, 2000; Zhao, 2007; Ilonidis, Zhao, & Hartlep, 2009), can monitor the Sun's activity in a synoptic way, both in the near and the far sides, and allow detection of large sunspot regions before their appearance on the solar disc. Strong emerging flux events can be anticipated 1-2 days in advance.

Chapter 6

Summary and Perspective

In this thesis, time-distance helioseismology measurements are carried out in order to detect sunspot regions before they become visible on the solar disc. The sunspot regions are either on the far-side of the Sun, and thus not visible from the Earth, or deep inside the convection zone before they emerge in the photosphere. The aim of our studies is to investigate the magnetic flux emergence through the convection zone to the photosphere, monitor the solar subsurface and far-side magnetic activity, and improve space-weather forecasting. We also perform time-distance measurements in sunspot regions that have already emerged on the solar disc in order to measure the coefficients of surface and deep absorption, emissivity reduction, and local suppression. These measurements determine quantitatively the effect of sunspot regions at the solar surface on the excitation and absorption of acoustic waves and may help the improvement of sunspot detection methods. We summarize below the main results of this dissertation and discuss perspectives for future studies.

6.1 Summary

First, we worked on the solar far-side imaging using the time-distance technique. This work was motivated by space weather forecasting needs to monitor the magnetic activity on the far hemisphere of the Sun. Existing methods, based on the helioseismic holography and the time-distance techniques, have been applied successfully to obtain

far-side maps but these maps are not always free of spurious features. We performed time-distance measurements using acoustic waves that travel to the solar far side and return to the front side with three skips, and succeeded in detecting far-side sunspot regions. The three-skip imaging method was first validated with use of numerical simulation data and then it was applied to SOHO/MDI Doppler observations to detect large sunspot regions on the solar far side. This method provides an independent imaging tool which in combination with the existing imaging tools can improve the quality of the far-side maps. The advantages and disadvantages of this method were discussed and the three-skip maps were combined with four- and five-skip maps to show the improvement in the quality of the final map.

Second, we determined the coefficients of surface absorption, deep absorption, emissivity reduction, and local suppression in sunspot regions. It is known that acoustic power is reduced in sunspot regions and this reduction can be attributed to several physical mechanisms. By analyzing a large sample of quiet and sunspot regions, we determined the contribution of each mechanism to the total power reduction from measurements of cross-covariance amplitudes. Our results indicate that absorption is the most important power-reduction mechanism for short horizontal wavelengths whereas for large horizontal wavelengths local suppression is mainly responsible for the observed power reduction. Surprisingly, it was also found that sunspots can absorb significant amounts of acoustic power not only close to the surface but also deep inside the convection zone. This effect may be useful for the development of helioseismic methods to investigate the subsurface properties of sunspot regions and the improvement of current sunspot detection methods. We also determined the coefficient of emissivity reduction and showed that the emissivity of acoustic waves is highly suppressed in sunspot regions and especially in the sunspot umbra. The lower value of the emissivity reduction in sunspot penumbra may indicate that there are more acoustic sources below the penumbra than the umbra. However, emissivity reduction accounts for only 15% – 20% of the observed power reduction which is dominated by the effects of absorption and local suppression.

After detecting sunspot regions on the solar far side and studying sunspots in the near-side photosphere, we focused our efforts on the detection of emerging sunspot

regions in the deep convection zone. The goal of this study is to detect subsurface helioseismic signatures of sunspot regions before these magnetic regions become visible in the photosphere. In chapter 4 we introduced a measurement procedure, based on the deep-focus time-distance helioseismology technique, which is able to detect sunspot regions at depths around 60 Mm. Searching helioseismic signals at such large depths requires accurate measurements with high sensitivity. We explained step-by-step the modifications that we introduced to previous time-distance measurement schemes and we demonstrated the increase in the S/N ratio with measurements in quiet and emerging-flux regions.

Once we developed this measurement procedure, we analyzed several emerging-flux regions and succeeded in detecting travel-time anomalies in the deep solar interior, several hours before the start of emergence at the surface and 1-2 days before the detected magnetic structures emerge in the photosphere. We studied the relationship between the travel-time perturbation amplitude and the magnetic flux emergence rate at the surface and found that large active regions emerge faster than smaller ones probably due to their larger magnetic buoyancy. The average emerging speed from depths around 60 Mm until the surface was estimated at $0.3 - 0.6$ km/s. Our measurements showed that the perturbation signatures persist for several hours and move from deeper to shallower regions with speeds up to 1 km/s. It was also found from the study of the cross-covariance function that the detected phase travel-time anomalies are associated with cross-covariance frequency perturbations that depend strongly on the acoustic frequency. Last, we managed to detect emerging sunspot regions using data from HMI and GONG instruments which are currently the only instruments that provide continuous helioseismic observations. The results of this study improve our understanding of magnetic flux emergence in the solar convection zone and may benefit space weather forecasting.

6.2 Perspective

A lot of progress has been made recently in helioseismic studies of sunspot regions. The far-side imaging and the determination of absorption coefficient are topics that

have been explored for more than a decade. On the other hand the detection of perturbations associated with strong emerging flux events in the deep convection zone is a new research finding that offers many opportunities for helioseismic studies. Here we discuss perspectives for future work and remaining open questions.

A statistical study with a large sample of emerging-flux regions is a very interesting topic and naturally extends our previous work. The events analyzed in this dissertation include some of the strongest emerging-flux regions that have been observed by MDI since 1996 and HMI since 2010. If this analysis method is applied to a large sample of regions, with various sizes and magnetic field strengths, it may be possible to determine whether a successful detection requires specific conditions such as a high magnetic flux emergence rate.

A statistical study is also needed to find possible connections between the subsurface activity in emerging flux regions with photospheric properties of sunspot regions or even with the flaring activity in these regions. Determining quantitative relationships between the subsurface perturbations and the total magnetic flux that emerges in the photosphere within the next few days is particularly useful for space weather forecasts. Several other ideas, which are currently under investigation, can be tested in future studies. It is believed for example that in some cases active regions that emerge separately within a few days may have common origin in the solar interior (Zhou et al., 2007). A systematic study of emerging-flux regions may reveal such “nests” of magnetic activity.

Regarding the measurement procedure, future work may offer the opportunity to refine the method used in this thesis and improve the sensitivity and S/N ratio. It should be noted that this method was developed and optimized by analyzing very strong emerging-flux events and modifications may be necessary for the detection of smaller emerging sunspot regions. It was shown that the arc configurations, the phase-speed filter, and the depth averaging play important role but several other parameters may affect the S/N ratio and more tests should be made with sunspots of different sizes.

The physical origin of the detected travel-time anomalies is not known yet. Possible physical mechanisms that may be related with these anomalies are discussed

in Ilonidis et al. (2012b). It may be hard to test from observations which of these mechanisms cause the travel-time anomalies but it is perhaps easier to make progress with use of numerical simulations. Simulation data can be also used to validate and further improve the helioseismic methods. An improvement of the S/N ratio may be required for the investigation of emerging magnetic flux in deeper layers.

All these are certainly very interesting topics and there are perhaps many more that need to be explored. Almost half a century since the first observations of solar oscillations, helioseismology still provides numerous opportunities for exciting discoveries.

Bibliography

Basu, S., Antia, H. M., & Tripathy, S. C. 1999, *Astrophys. J.*, 512, 458

Basu, S., Christensen-Dalsgaard, J., Chaplin, W. J., Elsworth, W., Isaak, G. R., New, R., Schou, J., Thompson, M. J., & Tomczyk, S. 1997, *Mon. Not. R. Astron. Soc.*, 292, 243

Birch, A. C., Braun, D. C., & Fan, Y. 2010, *Astrophys. J. Lett.*, 723, L190

Bogart, R. S., Sá, L. A. D., Duvall, T. L., Haber, D. A., Toomre, J., & Hill, F. 1995, in *Proceedings of the 4th SOHO Workshop*, 147

Bogdan, T., Brown, T., Lites, B., & Thomas, J. 1993, *Astrophys. J.*, 406, 723

Brandenburg, A. 2005, *Astrophys. J.*, 625, 539

Braun, D. C. 2012, *Science*, 336, 296

Braun, D. C., Duvall, T. L. Jr., & LaBonte, B. J. 1987, *Astrophys. J. Lett.*, 319, L27

Braun, D. C., Duvall, T. L. Jr., & LaBonte, B. J. 1988, *Astrophys. J.*, 335, 1015

Braun, D. C., Lindsey, C. 1999, *Astrophys. J.*, 513, L79

Braun, D. C. & Lindsey, C. 2000, *Solar Phys.*, 192, 307

Braun, D. C. & Lindsey, C. 2001, *Astrophys. J.*, 560, L189

- Burtseva, O., Kholikov, S., Serebryanskiy, A., & Chou, D.-Y. 2007, *Solar Phys.*, 241, 17
- Cally, P. S. & Bogdan, T. J. 1993, *Astrophys. J.*, 402, 721
- Cally, P. S., Bogdan, T. J., & Zweibel, E. G. 1994, *Astrophys. J.*, 437, 505
- Chang, H.-K., Chou, D.-Y., Labonte, B., & The TON Team 1997, *Nature*, 389, 825
- Chang, H.-K., Chou, D.-Y., & Sun, M.-T. 1999, *Astrophys. J.*, 526, L53
- Charbonneau, P. 2010, *Living Rev. Solar Phys.*, 7, 3
- Chen, K.-R., Chou, D.-Y., & the TON team 1996, *Astrophys. J.*, 465, 985
- Chen, P. F. & Shibata, K. 2000, *Astrophys. J.*, 545, 524
- Cheung, M. C. M., Schüssler, M., Tarbell, T. D., & Title, A. M. 2008, *Astrophys. J.*, 687, 1373
- Chou, D.-Y. & Ladenkov, O. 2007, *Solar Phys.*, 241, 7
- Chou, D.-Y., Liang, Z.-C., Yang, M.-H., & Sun, M.-T. 2009a, *Solar Phys.*, 255, 39
- Chou, D.-Y., Sun, M.-T., Huang, T.-Y., Lai, S.-P., Chi, P.-J., Ou, K.-T., Wang, C.-C., Lu, J.-Y., Chu, A.-L., Niu, C.-S., et al. 1995, *Solar Phys.*, 160, 237
- Chou, D.-Y., Yang, M.-H., Liang, Z.-C., & Sun, M.-T. 2009b, *Astrophys. J. Lett.*, 690, L23
- Chou, D.-Y., Liang, Z.-C., Yang, M.-H., Zhao, H., & Sun, M.-T. 2009c, *Astrophys. J. Lett.*, 696, L106
- Chou, D.-Y., Yang, M.-H., Zhao, H., Liang, Z.-C., & Sun, M.-T. 2009d, *Astrophys. J.*, 706, 909
- Christensen-Dalsgaard, J. 2002, *Rev. of Modern Phys.*, 74, 1073

Christensen-Dalsgaard, J., Däppen W., Ajukov, S. V., Anderson, E. R., Antia, H. M., Basu, S., Baturin, V. A., Berthomieu, G., Chaboyer, B., Chitre, S. M., et al. 1996, *Science*, 272, 1286

Claverie, A., Isaak, G. R., McLeod, C. P., van der Raay, H. B., & Roca Cortes, T. 1979, *Nature*, 282, 591

Couvidat, S., Rajaguru, S. P., Wachter, R., Sankarasubramanian, K., Schou, J., & Scherrer, P. H. 2011, *Solar Phys.*, 278, 217

Crouch, A. D. & Cally, P. S. 2005, *Solar Phys.* 227, 1

Deubner, F.-L. 1975, *Astron. Astrophys.*, 44, 371

Duvall Jr., T. L. 1994, *ASP Conf. Ser.*, 76, 465

Duvall, T. L., Jr. 2003, in *Proc. SOHO 12/GONG+ 2002, Local and Global Helioseismology: The Present and Future*, ed. H. Sawaya-Lacoste (ESA SP- 517; Noordwijk, Netherlands: ESA Publications Division), 259

Duvall, T. L. Jr., D'Silva, S., Jefferies, S. M., Harvey, J. W., & Schou, J. 1996, *Nature*, 379, 235

Duvall, T. L., Jr. & Harvey, J. W. 1983, *Nature*, 302, 24

Duvall, T. L. Jr. & Kosovichev, A. G. 2001, In: Brekke, P., Fleck, B., Gurman, J.B. (eds.) *IAU Symp. 203, Recent Insights into the Physics of the Sun and Heliosphere: Highlights from SOHO and Other Space Missions*, ASP, San Francisco, 159

Duvall, T. L. Jr., Kosovichev, A. G., & Scherrer, P. H. 2000, *Bull. Am. Astron. Soc.*, 32, 837

Duvall, T. L. Jr., Kosovichev, A. G., Scherrer, P. H., Bogart, R. S., Bush, R. I., De Forest, C., Hoeksema, J. T., Schou, J., Saba, J. L. R., Tarbell, T. D., et al. 1997, *Solar Phys.*, 170, 63

- Duvall Jr., T. L., Jefferies, S. M., Harvey, J. W., & Pomerantz, M. A. 1993, *Nature*, 362, 430
- D'Silva, S. 1994, *Astrophys. J.*, 435, 881
- Evans, J. W. & Michard, R. 1962, *Astrophys. J.*, 136, 493
- Fan, Y. 2008, *Astrophys. J.*, 676, 680
- Fan, Y. 2009, *Living Rev. Solar Phys.*, 6, 4
- Fang, F., Manchester IV, W., Abbett, W. P., & Holst, B. V. D. 2010, *Astrophys. J.*, 714, 1649
- Fang, F., Manchester IV, W., Abbett, W. P., & Holst, B. V. D. 2012, *Astrophys. J.*, 745, 37
- Fisher, G. H., Fan, Y., Longcope, D. W., Linton, M. G., & Pevtsov, A. A. 2000, *Solar Phys.*, 192, 119
- Giles, P. M. 1999, Ph.D. Thesis, Stanford University
- Giles, P. M., Duvall, T. L., Jr., Scherrer, P. H., & Bogart, R. S. 1997, *Nature*, 390, 52
- Gizon, L. & Birch, A. C. 2004, *Astrophys. J.*, 614, 472
- Gizon, L., Duvall, T. L., Jr., & Larsen, R. M. 2000, *J. Astrophys. Astr.*, 21, 339
- Goldreich P. & Keeley, D. A. 1977, *Astrophys. J.*, 212, 243
- González Hernández, I., Patrón, J., Chou, D.-Y., & The TON Team 1998, *Astrophys. J.*, 501, 408
- Goossens, M. & Poedts, S. 1992, *Astrophys. J.*, 384, 348
- Gordovskyy, M. & Jain, R. 2008, *Astrophys. J.*, 681, 664

- Gough, D. O. 1993, in *Astrophysical Fluid Dynamics*, ed. J.-P. Zahn & J. Zinn-Justin, Elsevier Science Publ., 339
- Gough, D. O. & Toomre, J. 1983, *Solar Phys.*, 82, 401
- Haber, D. A., Hindman, B. W., Toomre, J., Bogart, R. S., Larsen R. M., & Hill, F. 2002, *Astrophys. J.*, 570, 855
- Haber, D. A., Hindman, B. W., Toomre, J., Bogart, R. S., Thompson, M. J., & Hill, F. 2000, *Solar Phys.*, 192, 335
- Hale, G. E., Ellerman, F., Nicholson, S. B., & Joy, A. H. 1919, *Astrophys. J.*, 49, 153
- Hartlep, T., Kosovichev, A. G., Zhao, J., & Mansour, N. N. 2011, *Solar Phys.*, 268, 321
- Hartlep, T., Zhao, J., Mansour, N. N., & Kosovichev, A. G. 2008, *Astrophys. J.*, 689, 1373
- Harvey, J. W., Hill, F., Hubbard, R. P., Kennedy, J. R., Leibacher, J. W., Pintar, J. A., Gilman, P. A., Noyes, R. W., Title, A. M., Toomre, J., Ulrich, R. K., Bhatnagar, A., Kennewell, J. A., Marquette, W., Patron, J., Saa, O., & Yasukawa, E. 1996, *Science*, 272, 1284
- Hathaway, D. H. 2010, *Living Rev. Sol. Phys.*, 7, 1
- Hill, F. 1988, *Astrophys. J.*, 333, 996
- Hindman, B. W., Jain, R., & Zweibel, E. G. 1997, *Astrophys. J.*, 476, 392
- Hollweg, J. 1988, *Astrophys. J.*, 335, 1005
- Hurlburt, N. & Toomre, J. 1988, *Astrophys. J.*, 327, 920
- Ilonidis, S. & Zhao, J. 2011, *Solar Phys.*, 268, 377
- Ilonidis, S., Zhao, J., & Hartlep, T. 2009, *Solar Phys.*, 258, 181

- Ilonidis, S., Zhao, J., & Kosovichev, A. 2011, *Science*, 333, 993
- Ilonidis, S., Zhao, J., & Kosovichev, A. 2012a, <http://arxiv.org/abs/1203.2546>
- Ilonidis, S., Zhao, J., & Kosovichev, A. 2012b, *Science*, 336, 296
- Jensen, J. M., Duvall Jr., T. L., Jacobsen, B. H., & Christensen-Dalsgaard, J. 2001, *Astrophys. J.*, 553, L193
- Kholikov, S. 2012, private communication
- Komm, R., Howe, R., & Hill, F. 2009, *Solar Phys.*, 258, 13
- Kosovichev, A. G. 2009, *Space Sci. Rev.*, 144, 175
- Kosovichev, A. G., & Duvall, T. L., Jr. 1997, in *SCORRe96: Solar Convection and Oscillations and their Relationship*, ed. F. P. Pijpers, J. ChristensenDalsgaard, & C. S. Rosenthal (Astrophysics and Space Science Library, Vol. 225; Dordrecht: Kluwer), 241
- Kosovichev, A. G. & Duvall Jr., T. L. 2008, *ASP Conf. Ser.*, 383, 59
- Kosovichev, A. G., Duvall, T. L. Jr., & Scherrer, P. H. 2000, *Solar Phys.*, 192, 159
- Kosovichev, A. G., Schou, J., Scherrer, P. H., Bogart, R. S., Bush, R. I., Hoeksema, J. T., et al. 1997, 170, 43
- Leibacher, J. W. & Stein, R. F. 1971, *Astrophys. Lett.*, 7, 191
- Leighton, R., Noyes, R., & Simon, G. 1962, *Astrophys. J.*, 135, 474
- Liewer, P. C., González Hernández, I., Hall, J. R., Thompson, W. T., & Misrak, A. 2012, *Solar Phys.*, DOI: 10.1007/s11207-012-9932-9
- Lindsey, C. & Braun, D. C 1990, *Sol. Phys.*, 126, 101
- Lindsey, C. & Braun, D. C. 1997, *Astrophys. J.*, 485, 895
- Lindsey, C. & Braun, D. C. 1998, *Astrophys. J.*, 499, L99

- Lindsey, C. & Braun, D. C. 2000a, *Science*, 287, 1799
- Lindsey, C. & Braun, D. C. 2000b, *Solar Phys.*, 192, 261.
- Lindsey, C. & Braun, D. C. 2005, *Astrophys. J.*, 620, 1107
- Lites, B. W., White, O. R., & Packman, D. 1982, *Astrophys. J.*, 253, 386
- Lou, Y.-Q. 1990, *Astrophys. J.*, 350, 452
- Maunder, E. W. 1904, *Mon. Not. R. Astron. Soc.*, 64, 747
- Parchevsky, K. V. & Kosovichev, A. G. 2007, *Astrophys. J. Lett.*, 666, L53
- Rajaguru, S. P., Sankarasubramanian, K., Wachter, R., & Scherrer, P. H. 2007, *Astrophys. J. Lett.*, 654, L178
- Rempel, M. & Schlichenmaier R. 2011, *Living Rev. Solar Phys.*, 8, 3
- Rhodes, Jr., E. J., Ulrich, R. K., & Simon, G. W. 1977, *Astrophys. J.*, 218, 901
- Roddier, F. 1975, *C. R. Acad. Sci. Ser. B.*, 281, 93
- Roth, M., Gizon, L., & Beck, J. G. 2007, *Astron. Nachr.*, 328, 215
- Sakurai, T., Goossens, M., & Hollweg, J. V. 1991, *Solar Phys.*, 133, 247
- Scherrer, P.H., Bogart, R. S., Bush, R. I., Hoeksema, J. T., Kosovichev, A. G., Schou, J., Rosenberg, W., Springer, L., Tarbell, T. D., Title, A., et al. 1995, *Solar Phys.*, 162, 129
- Scherrer, P.H., Schou, J., Bush, R. I., Kosovichev, A. G., Bogart, R. S., Hoeksema, J. T., Liu, Y., Duvall, T. L., Zhao, J., Title, A. M., Schrijver, C. J., Tarbell, T. D., & Tomczyk, S. 2012, *Solar Phys.*, 275, 207
- Schou, J., Antia, H. M., Basu, S., Bogart, R. S., Bush, R. I., Chitre, S. M., Christensen-Dalsgaard, J., di Mauro, M. P., Dziembowski, W. A., Eff-Darwich, A., et al. 1998, *Astrophys. J.*, 505, 390

- Schou, J. & Bogart, R. S. 1998, *Astrophys. J. Lett.*, 504, L131
- Schou, J., Scherrer, P. H., Bush, R. I., Wachter, R., Couvidat, S., Rabello-Soares, M. C., Bogart, R. S., Hoeksema, J. T., Liu, Y., Duvall, T. L., et al. 2012, *Solar Phys.*, 275, 229
- Schwabe, H. 1844, *Astron. Nachr.*, 21, 233
- Snodgrass, H. B. 1984, *Solar Phys.*, 94, 13
- Solanki, S. K. 2003, *Astron. Astrophys. Rev.*, 11, 153
- Spruit, H. C. & Bogdan, T. J. 1992, *Astrophys. J. Lett.*, 391, L109
- Toriumi, S. & Yokoyama, T. 2010, *Astrophys. J.*, 714, 505
- Toriumi, S. & Yokoyama, T. 2011, *Astrophys. J.*, 735, 126
- Toriumi, S., Hayashi, K., & Yokoyama, T. 2012, *Astrophys. J.*, 751, 154
- Ulrich, R. K. 1970, *Astrophys. J.*, 162, 993
- Usoskin, I. G. 2008, *Living Rev. Solar Phys.*, 5, 3
- Vernazza, J. E., Avrett, E. H., & Loeser, R. 1981, *Astrophys. J. Suppl.*, 45, 635
- Wachter, R., Schou, J., & Sankarasubramanian, K. 2006, *Astrophys. J.*, 648, 1256
- Weber, M. A., Fan, Y., & Miesch, M. S. 2011, *Astrophys. J.*, 741, 11
- Wittman, A. D. & Xu, Z. T. 1987, *Astron. Astrophys. Suppl. Ser.*, 70, 83
- Woodard, M. F. 1997, *Astrophys. J.*, 485, 890
- Zhao, H., Chou, D.-Y., & Yang, M.-H. 2011, *Astrophys. J.*, 740, 56
- Zhao, J. 2007, *Astrophys. J.*, 664, L139.
- Zhao, J., Couvidat, S., Bogart, R. S., Parchevsky, K. V., Birch, A. C., Duvall, T. L., Beck, J. G., Kosovichev, A. G., & Scherrer, P. H. 2012, 275, 375

- Zhao, J. & Kosovichev, A. G. 2003, *Astrophys. J.*, 591, 446
- Zhao, J. & Kosovichev, A. G. 2004, *Astrophys. J.*, 603, 776
- Zhao, J. & Kosovichev, A. G. 2006, *Astrophys. J.*, 643, 1317
- Zhao, J., Kosovichev, A. G., & Duvall, T. L., Jr. 2001, *Astrophys. J.*, 557, 384
- Zhao, J., Kosovichev, A. G., & Ilonidis, S. 2011, *Solar Phys.*, 268, 429
- Zharkov, S. & Thompson, M. J. 2008, *Solar Phys.*, 251, 369
- Zhou, G., Wang, J., Wang, Y., & Zhang, Y. 2007, *Solar Phys.*, 244, 13